RUPRECHT-KARLS-UNIVERSITÄT HEIDELBERG

Falk Bartels

Improving the Sensitivity of Dark Matter Searches by Combining Unfolded Experimental Signatures

Masterarbeit

HD-KIP-18-04

KIRCHHOFF-INSTITUT FÜR PHYSIK

Department of Physics and Astronomy

University of Heidelberg

Master thesis

in Physics

submitted by

Falk Bartels

born in Hildesheim

2017

Improving the Sensitivity of Dark Matter Searches by Combining Unfolded Experimental Signatures

This Master thesis has been carried out by Falk Bartels

at the

Kirchhoff-Institute for Physics

under the supervision of

Priv.-Doz. Monica Dunford

Steigerung der Sensitivität von Suchen nach Dunkler Materie durch Kombination entfalteter experimenteller Signaturen

Methoden der Entfaltung ermöglichen es, in Beschleunigerexperimenten gemessene kinematische Verteilungen um Detektoreffekte zu korrigieren. Dies ermöglicht den direkten Vergleich mit beliebigen Modellvorhersagen. Zusätzlich wird so die gleichzeitige Berücksichtigung von Beobachtugnen aus mehreren Quellen zur Überprüfung eines bestimmten Modells vereinfacht. In gegenwärtig veröffentlichten Suchen nach Dunkler Materie wird das üblicherweise nicht durchgeführt. Diese vorliegende Arbeit demonstriert die mögliche Verbesserung der Sensitivität gegenüber Physik jenseits des Standardmodells durch die Kombination einer Mono-Jet und einer Mono-Z Signatur. Die präsentierte Studie basiert auf Proton-Proton Kollisionen bei $\sqrt{s} = 13\,\text{TeV}$, die einer integrierten Luminosität von 3,2 fb^{-1} entsprechen und 2015 vom ATLAS Detektor am Large Hadron Collider aufgezeichnet wurden.
Durch die Kombination beider Signaturen können die oberen Grenzwerte für Wirkungsquerschnitte um einen Faktor von bis zu 2,4 gegenüber der separaten Analyse beider Signaturen verbessert werden. Die gewonnene Sensitivität ist dabei maximal, wenn die berücksichtigten Signaturen individuell eine vergleichbare Sensitivität bieten.

Improving the Sensitivity of Dark Matter Searches by Combining Unfolded Experimental Signatures

Methods of unfolding allow to correct for detector effects in kinematic distributions observed in collider experiments such that they can be directly compared to arbitrary model predictions. This also simplifies the process of testing a given model under simultaneous consideration of observations from multiple sources, which is not commonly done in present dark matter searches. This thesis demonstrates the possible gain in sensitivity to physics beyond the Standard Model by combining observations in a mono-jet and a mono-Z signature. The performed study is based on the analysis of proton-proton collisions at $\sqrt{s} = 13\,\text{TeV}$ corresponding to an integrated luminosity of $3.2\,\text{fb}^{-1}$, recorded by the ATLAS detector at the Large Hadron Collider in 2015.
By combining both signatures instead of analyzing them separately, an improvement of upper cross section limits by a factor of up to 2.4 is found. The sensitivity gain becomes maximal in the case of similar sensitivity of the two signatures.

Contents

1 Introduction

The nature of dark matter is one of the leading puzzles in today's physics community. Despite strong astronomical evidence for its existence, the Standard Model of particle physics cannot yet provide a viable particle candidate to explain the observations. This motivates the search for yet unknown particles in a variety of experiments. The study of proton-proton collisions at the Large Hadron Collider by the ATLAS and CMS collaborations is one approach.

The common strategy in such a search is to compare the recorded data to simulated events, which are generated according to predictions of the Standard Model as well as selected theories beyond the Standard Model in order to constrain the latter. To perform this comparison, the simulated collision events are interfaced to a simulation of the detector such that they account for detector effects like resolution or inefficiencies which are present in recorded data. However, this procedure limits the possibility of using already published measurements to test models different from those considered in the publication. It would require the application of the computationally very demanding and not necessarily publicly available detector simulation to events predicted by the new model in question.

Unfolding is a powerful method to overcome this limitation by removing detector effects from the observations instead. Unfolded kinematic distributions can be directly compared to predictions of arbitrary signal models without the need of a detector simulation, enabling more researchers to test new models against data.

The preservation of relevance for future models by publishing unfolded results bears additional potential: It facilitates combined analyses of multiple publications. Typically, a specific detector signature is studied and the observations are used to constrain a selection of proposed models. If a certain model, however, predicts contributions to several detector signatures, this is typically not taken into account for the constraints. Instead, limits on model parameters are placed by each study individually such that ultimately only the strongest ones are of interest. A combined analysis of multiple signatures, on the other hand, can potentially improve the sensitivity compared to each individual one as a larger set of observations is taken into account.

To date, constraining a certain model with a combined analysis of multiple publications proves difficult since the provision of unfolded results is rare. Instead, one is limited to those signatures, whose respective publications consider the model in question in the first place. Additionally, these need to precisely state the predicted event numbers after the detector simulation as well as all sources of systematic uncertainties individually to account for correlations.

This thesis demonstrates the possibility to combine multiple signatures if unfolded results are available and evaluates the potential gain in sensitivity. Two typical signatures for dark matter searches – the mono-jet and the mono-Z topology – are analyzed and the results unfolded. They are then used to constrain three different signal models:

WIMP production via an axial-vector mediator, the decay of the Higgs boson into an invisible final state, and the existence of an additional heavy Higgs-like scalar. These constraints are derived for both signatures individually as well as in a combined analysis to evaluate the gain in sensitivity. The presented studies use proton-proton collisions at a center-of-mass energy of $\sqrt{s} = 13\,\text{TeV}$ recorded by the ATLAS detector in 2015 corresponding to an integrated luminosity of $3.2\,\text{fb}^{-1}$.

The structure of this thesis is as follows. Chapter 2 provides an overview of the Standard Model as theoretical background. Possible extensions with special emphasis on dark matter and its potential discovery in a collider experiment are considered as well. Chapter 3 introduces the process of unfolding and the algorithms used in this thesis. The experimental setup, in particular the Large Hadron Collider and the ATLAS detector, is described in Chapter 4. Chapter 5 provides details on the reconstruction of the physics objects used for this thesis. The mono-jet analysis and the unfolding of the results is presented in Chapter 6. Chapter 7 provides the description of the mono-Z analysis and the respective unfolding. In Chapter 8, the process of constraining models by observations in single or multiple signatures is discussed and the results for the three considered models are presented. Finally, the results of this thesis are summarized.

2 Theoretical Background

Today's best understanding of the fundamental nature of matter is given by the Standard Model of particle physics. Developed in the 1960s and early 70s it correctly describes almost all experimental observations to date. It is outlined in Section 2.1 following the description in References [1, 2]. But regardless of its great successes, we know the Standard Model to be incomplete. A selection of phenomena not described by it and possible extensions is given in Section 2.2. The mono-X signature sensitive to those extensions is discussed in Section 2.3.

2.1 The Standard Model of Particle Physics

The Standard Model of particle physics is a relativistic quantum field theory describing how the elementary particles interact via the exchange of gauge bosons. It contains three *forces* which are generated by imposing a local gauge symmetry of the $\mathrm{SU}(3)_C \times \mathrm{SU}(2)_L \times \mathrm{U}(1)_Y$ groups. This combines the *electroweak theory* developed by Glashow, Salam and Weinberg [3–5] with *quantum chromodynamics* (QCD) describing the strong interaction [6, 7].

The Standard Model contains the twelve fundamental spin $1/2$ fermions listed in Table 2.1 and their respective antiparticles. They are grouped into quarks and leptons depending on whether they interact via the strong force or not, and into three generations sorted by their mass.

Each of the three lepton generations consists of a charged lepton and its corresponding electrically neutral partner, a neutrino. They are called electron (e), muon (μ) and tau (τ), accordingly the neutrinos are the electron-neutrino (ν_e), muon-neutrino (ν_μ) and tau-neutrino (ν_τ). All leptons are subject to the weak interaction while only the charged leptons interact electromagnetically. According to the Standard Model's lepton universality, the three generations behave completely identical except for their different

	generation			electric	weak	color
	1	2	3	charge [e]	charge	charge
leptons	ν_e	ν_μ	ν_τ	0	yes	no
	e	μ	τ	-1	yes	no
quarks	u	c	t	$+2/3$	yes	yes
	d	s	b	$-1/3$	yes	yes

Table 2.1: Fermions of the Standard Model

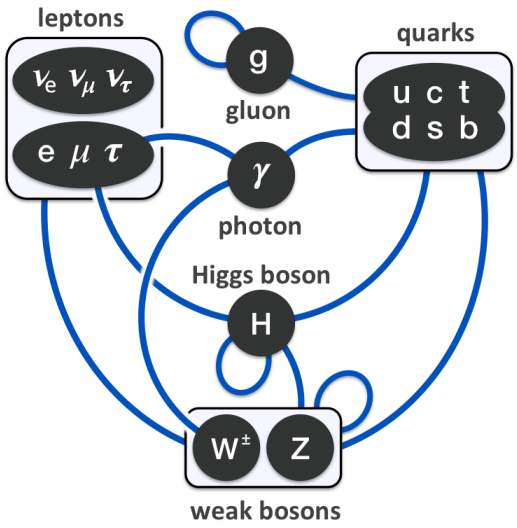

Figure 2.1: Possible interactions between the fundamental fermions and bosons of the Standard Model. Blue lines indicate a non-zero coupling and those attached to a box act on every fermion or boson inside it. Although eight different gluons exist, only one is shown here, because their interactions cannot be observed individually. [8]

masses[1].

The six quarks are the up (u), down (d), charm (c), strange (s), top (t) and bottom (b). Each of the three generations contains an up-type quark with positive electrical charge and a down-type quark with negative charge, as also indicated in Table 2.1. Unlike leptons, quarks are subject to all three fundamental forces as they also carry color charge.

The forces are mitigated by twelve spin 1 gauge bosons. A schematic of which fermions and other bosons they couple to is provided in Figure 2.1. A more detailed description of the interactions is given in the following sections.

2.1.1 Electroweak Interaction

For now, consider the electroweak sector without particle masses – they are added in the next section via the Higgs mechanism.

Following from the degrees of freedom of the local gauge symmetries, the electroweak theory contains four gauge fields: the B_μ from the generator of the $\mathrm{U}(1)_Y$ group and the three W^a_μ, $a \in \{1, 2, 3\}$, fields from the generators of the $\mathrm{SU}(2)_L$ group. They give rise to their corresponding field strength tensors

$$B_{\mu\nu} = \partial_\mu B_\nu - \partial_\nu B_\mu \tag{2.1}$$

$$W^a_{\mu\nu} = \partial_\mu W^a_\nu - \partial_\nu W^a_\mu + g\epsilon^{abc} W^b_\mu W^c_\nu \,, \tag{2.2}$$

where g denotes the coupling constant of the weak interaction and ϵ^{abc} the totally anti-symmetric Levi-Civita tensor. The additional term for $W^a_{\mu\nu}$ allows for a self-interaction of

[1] With the addition of neutrino masses to the Standard Model and the corresponding extension from 19 to 26 free parameters, this exception needs to include the mixing angles between the neutrino mass and flavor eigenstates.

the W fields. It arises because $\mathrm{SU}(2)_L$ is non-abelian, meaning the commutator $\left[W_\mu, W_\nu\right]$ does not vanish.

Imposing that the weak fields W_μ^a only couple to left-handed fermion spinors ψ_L leads to the following covariant derivatives:

$$\mathrm{D}_\mu \psi_L = \left(\partial_\mu + i\frac{g}{2}\sigma^a W_\mu^a - i\frac{g'}{2}B_\mu\right)\psi_L \tag{2.3}$$

$$\mathrm{D}_\mu \psi_R = \left(\partial_\mu + i\frac{g'}{2}B_\mu\right)\psi_R \tag{2.4}$$

where g' is the coupling of the electromagnetic interaction and σ^a are the three Pauli matrices.

Using these expressions, the electroweak Lagrangian density is written as:

$$\begin{aligned}\mathcal{L}_{\mathrm{EW}} = &-\frac{1}{4}B^{\mu\nu}B_{\mu\nu} - \frac{1}{4}W_a^{\mu\nu}W_{\mu\nu}^a \\ &+ \sum_{\text{fermions}} \left(i\bar{\psi}_L \,\mathrm{D}_\mu\, \gamma^\mu \psi_L + i\bar{\psi}_R \,\mathrm{D}_\mu\, \gamma^\mu \psi_R\right),\end{aligned} \tag{2.5}$$

where γ^μ are the Dirac matrices. Expressing this in terms of the raising and lowering operators $\sigma_\pm = (\sigma_1 \pm i\sigma_2)/2$ of $\mathrm{SU}(2)_L$ identifies the physically observable charged bosons

$$W_\mu^\pm = \frac{1}{\sqrt{2}}\left(W_\mu^{(1)} \mp i W_\mu^{(2)}\right). \tag{2.6}$$

The remaining uncharged $W^{(3)}$ and B fields superpose to the physical Z boson and the photon. The ratio of the two contributions is expressed in terms of the Weinberg angle θ_W:

$$\begin{pmatrix} A_\mu \\ Z_\mu \end{pmatrix} = \begin{pmatrix} \cos\theta_W & \sin\theta_W \\ -\sin\theta_W & \cos\theta_W \end{pmatrix} \cdot \begin{pmatrix} B_\mu \\ W_\mu^{(3)} \end{pmatrix}. \tag{2.7}$$

The necessity for the superposition as well as the value of θ_W arises naturally from the Higgs mechanism described in the following section.

2.1.2 Higgs Mechanism

Introducing a boson mass term like $\frac{1}{2}m_Z^2 Z_\mu Z^\mu$ into the electroweak Lagrangian proposed in Equation 2.5 would break the required gauge invariance under $\mathrm{SU}(2)_L$. In the Standard Model, this contradiction is resolved by the particles acquiring mass via interaction with the Higgs field. The minimal Higgs model consists of two complex scalar fields arranged in a doublet ϕ under $\mathrm{SU}(2)_L$. Its Lagrangian density contains a potential $V(\phi)$ of fourth order:

$$\mathcal{L}_{\mathrm{Higgs}} = \left(\mathrm{D}^\mu \phi\right)^\dagger \left(\mathrm{D}_\mu \phi\right) - V(\phi) \tag{2.8}$$

$$V(\phi) = \mu^2 \phi^\dagger \phi + \lambda\left(\phi^\dagger \phi\right)^2. \tag{2.9}$$

The covariant derivative in this case behaves completely analogous to the left handed fermions:

$$\mathrm{D}_\mu \phi = \left(\partial_\mu + i\frac{g}{2}\sigma^a W_\mu^a + i\frac{g'}{2}B_\mu\right)\phi\,. \tag{2.10}$$

For $\mu^2 < 0$ and $\lambda > 0$, $V(\phi)$ assumes the famous Mexican hat shape with infinite global minima at a non-vanishing vacuum expectation value $v^2 = -\mu^2/\lambda$. One of those is physically chosen by a spontaneous symmetry breaking of the vacuum. Expanding the Lagrangian in perturbation theory around the physical vacuum state and requiring the photon to become massless then creates W and Z mass terms and fixes the Weinberg angle

$$m_W = \frac{v}{2}\,g\,, \quad m_Z = \frac{v}{2}\,\sqrt{g^2 + g'^2}\,, \quad \tan\theta_W = \frac{g'}{g}\,. \tag{2.11}$$

The asymmetry of Φ around the vacuum state gives rise to a massive scalar – the Higgs boson – with a coupling to the W and the Z bosons proportional to their masses.

Similar to the bosons, an introduction of fermion mass terms $m_f\bar{\psi}\psi$ violates the $\mathrm{SU}(2)_L$ gauge symmetry. The Higgs mechanism works around this by introducing a Yukawa coupling of the fermions to the Higgs field:

$$\mathcal{L}_{\text{Yukawa}} = -g_f\left(\bar{\psi}_L\phi\psi_R + \left(\bar{\psi}_L\phi\psi_R\right)^\dagger\right). \tag{2.12}$$

And again, expanding around the physical vacuum state gives rise to mass terms

$$m_f = \frac{\sqrt{2}}{v}\,g_f\,. \tag{2.13}$$

Requiring consistency with the observed fermion masses, this relation fixes their couplings g_f to the Higgs boson itself.

2.1.3 Strong Interaction

The theory of quantum chromodynamics assigns a *color* charge to quarks which makes them subject to the strong interaction. This color charge can assume one of three orthogonal states (or the respective "anti"-states for antiquarks) which we label red, green and blue. QCD is based on the $\mathrm{SU}(3)_C$ symmetry that gives rise to the eight gluon fields G_μ^a, $a \in \{1, \ldots, 8\}$. They require the covariant derivative

$$\mathrm{D}_\mu \psi = \left(\partial_\mu + i\frac{g_S}{2}\lambda^a G_\mu^a\right)\psi\,, \tag{2.14}$$

where λ^a are the Gell-Mann matrices, the generators of SU(3). As SU(3) is non-abelian, the corresponding field strength tensor includes a self-interaction term like in the weak interaction:

$$G_{\mu\nu}^a = \partial_\mu G_\nu^a - \partial_\nu G_\mu^a + g_S f^{abc} G_\mu^b G_\nu^c\,, \tag{2.15}$$

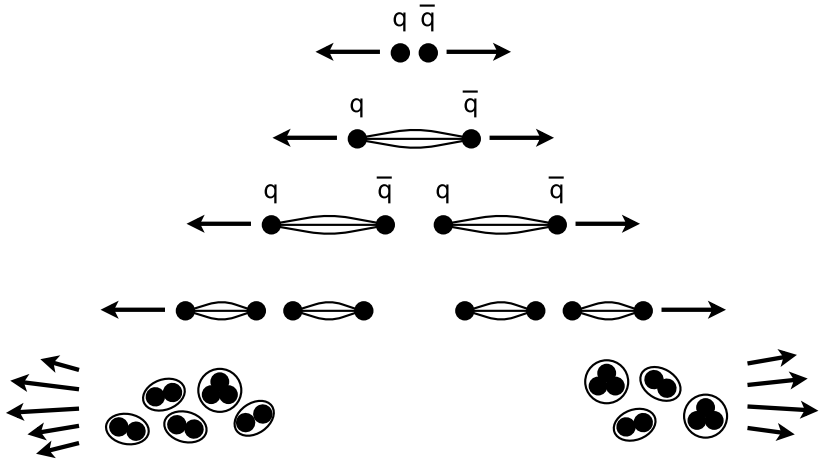

Figure 2.2: Effect of color confinement on two quarks moving away from each other. As soon as sufficient energy is stored in the gluon field, a $q\bar{q}$ pair can be created that breaks up the gluon tube. This process continues until all quarks are bound in color-neutral hadrons. Adapted from Reference [1].

where g_S is the strong coupling and f^{abc} are the structure constants fulfilling $\left[\lambda^a, \lambda^b\right] = if^{abc}\lambda^c$. In those terms, the QCD Lagrangian can be written as

$$\mathcal{L}_{\text{QCD}} = -\frac{1}{4}G^a_{\mu\nu}G^{\mu\nu}_a + \sum_{\text{quarks}} i\bar{\psi}\gamma^\mu \,\mathrm{D}_\mu\, \psi\,. \tag{2.16}$$

The gluon self-interaction term in Equation 2.15 gives rise to a defining feature of QCD: color confinement. It dictates, that no object with non-zero color charge, like a quark, can propagate as free particle. It can be explained qualitatively by gluon "tubes" caused by the gluon-gluon self interaction. The process is shown schematically in Figure 2.2. When two quarks move away from each other, an attractive interaction between them is mitigated via virtual gluons. But the gluons themselves carry color charge, so they are attracted to each other as well. For quarks at a relatively large distance, this creates a compressed tube of gluons between them resulting in a constant force independent of their distance. Quarks moving away from each other thus store energy $V(r) \propto r$ in the gluon field between them. With sufficient energy in the gluon tube, new $q\bar{q}$ pairs can be created. If the remaining quarks and antiquarks connected by tubes still have large relative momenta, this sequence repeats until all are of sufficiently low energy in their respective center-of-mass frames to form color-neutral hadrons. This process of *hadronization* causes quarks and gluons produced in collider experiments to appear as collimated sprays of particles in the detector – so-called *jets*.

A second challenging aspect of QCD is the running of the strong coupling $\alpha_S \propto g_S^2$. Unlike in quantum electrodynamics, it *decreases* with energy due to gluon self-interactions. Correspondingly, it becomes large in low-energy interactions. At energies around 1 GeV and below, α_S is of $\mathcal{O}(1)$. This limits the applicability of perturbation theory in this regime, making the aforementioned hadronization as well as initial and final state radiation difficult to model. Closely related to the running of α_S are the renormalization which cancels ultraviolet divergences [6, 7], and the factorization which cancels infrared

divergencies [9]. They are not scope of this thesis, but uncertainties due to their scale choices appear in Chapters 6 and 7.

2.2 Physics Beyond the Standard Model

Despite the Standard Model's great success, we know it to be incomplete. Strikingly, it lacks a description of gravity, which itself is described by general relativity without deviations between observations and predictions to date. Attempts to quantify the underlying Einstein-Hilbert action could not resolve ultraviolet divergencies [10, 11]. More exotic approaches like string theory [12] and quantum loop gravity [13] are currently under development but still lack predictive power. Experimental constraints on the number of spatial dimensions or even the discovery of the graviton could potentially lead to further progress in these fields [14].

Another puzzle is the baryon asymmetry, meaning the observed dominace of matter over antimatter in the Universe. It requires a violation of the CP (charge conjugation, parity) symmetry because otherwise matter and antimatter would have been created in equal amounts after the Big Bang [15]. Such a violation is indeed present in the Standard Model in form of the quark flavor mixing under the weak interaction and potentially in neutrino oscillations. However, the measured CP violation in the quark sector is insufficient to account for the observed asymmetry. The violation in the lepton sector, on the other hand, is yet to be determined in upcoming, more sensitive experiments [16]. Depending on the outcome, additional sources of CP violation beyond the Standard Model might be necessary.

The last shortcoming of the Standard Model considered in this scope is its lack of a suitable candidate for dark matter. This is the main motivation for the searches presented in this thesis and the results are interpreted in the context of dark matter models. A description of these is given in the following section.

2.2.1 Dark Matter

Various sources of astronomical evidence let us assume, that a significant amount of matter present in the Universe is not bound in luminous stars or interstellar gas clouds, but is *dark* instead. Especially compelling are velocity distributions of stars in disk galaxies [17, 18]. Outside the central bulge of such a galaxy and assuming rotational symmetry, a star's tangential velocity should be dictated by the typical centripetal acceleration in a gravitational field

$$\frac{mv^2}{r} \approx \frac{Gm}{r^2} M(r)\,, \tag{2.17}$$

where $M(r)$ is the total mass inside the orbit of radius r. As the majority of the visible mass is concentrated around the center of the galaxy, the visible $M(r)$ is approximately constant for large radii. Correspondingly, the tangential velocity should decrease as $v(r) \propto r^{-1/2}$. However, observed velocity distributions show no strong radial dependence of the velocities outside the central bulge, implying a mass distribution of approximately

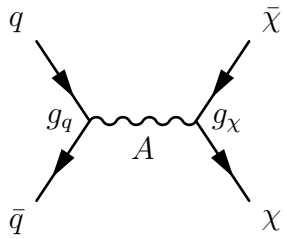

Figure 2.3: WIMP production via an axial-vector mediator. The couplings of the mediator to quarks and to WIMPs can in principle be chosen arbitrarily. In this thesis, they are fixed to $g_q = 0.25$ and $g_\chi = 1$ as benchmark.

$M(r) \propto r$. This hints at large halos of matter around the studied galaxies that interact gravitationally but not electromagnetically.

Additional evidence is available by observations using gravitational lensing. Light passing a massive object follows the null geodesics of the spacetime curved towards this object. This results in a deflection angle seen by a distant observer and a lensing effect caused by said massive object. This effect can be used to infer the mass distributions in the path between the light source and the observer. Especially weak gravitational lensing in combination with the cosmic microwave background as light source [19] can be used to map the mass density across large sections of the celestial sphere [20]. Mismatches of this gravitationally interacting mass distribution and visible matter then indicate dark matter.

A famous example of the lensing effect not matching the visible matter is the *Bullet Cluster* consisting of two colliding clusters [21]. Observations in the X-ray spectrum show that the hot gas in the clusters collided, resulting in a distinct "bullet-shot" shape. The dark matter identified by gravitational lensing and the stars, on the other hand, passed collisionless. This results in a clear separation of the visible baryonic matter dominated by the hot gas and the mass distribution inferred from the lensing effect.

These and other present observations themselves do not reveal the fundamental nature of the dark matter. The prevalent ΛCDM (Lambda cold dark matter) model of cosmology [22], however, constrains candidates for dark matter by their effect on large-scale structure formation in the Universe. Light particles, like neutrinos, would remain relativistic (hot) throughout the cooling of the Universe and hinder the clumping of matter. They would thus affect structure formation in a different way than massive particles that become non-relativistic (cold) in the first few years after the Big Bang. Additionally, the candidate needs to yield the observed relic abundance, meaning the correct amount of dark matter remaining from its production in the thermal equilibrium of the early Universe. These constraints make *weakly interacting massive particles* (WIMPs) χ in the GeV–TeV range a promising dark matter candidate.

In order for WIMPs to interact with quarks, typically a mediator with a coupling g_q to quarks, g_χ to the WIMPs and no interaction with any other Standard Model particle is introduced. This way, the production of WIMPs in a proton-proton collision could happen e.g. in an s-channel diagram as depicted in Figure 2.3. In this thesis, a model with a neutral, spin 1 axial-vector mediator A is tested, since vector mediators are already well constrained by direct detection experiments [23]. Generic scalar or pseudo-scalar

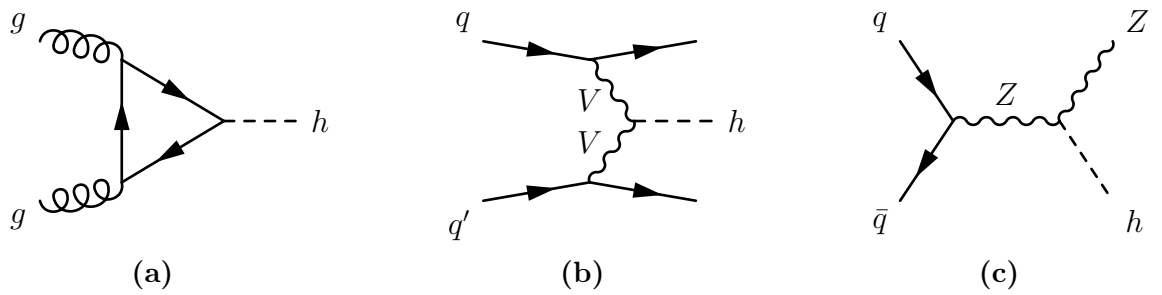

Figure 2.4: Example diagrams for the three considered production modes of Higgs bosons in p-p collisions ordered by their total production cross section [25]: **(a)** gluon-gluon fusion with $\sigma(\text{ggF-}h) = 48.6\,\text{fb}$. The internal fermion loop can in principle be any quark, but due to the Higgs boson coupling proportionally to the mass of the fermion, it is most likely a top or bottom loop. **(b)** vector boson fusion with $\sigma(\text{VBF-}h) = 3.74\,\text{fb}$. V denotes a W or Z boson in this case. **(c)** Higgs radiation from a Z boson with $\sigma(q\bar{q} \to Zh) = 888\,\text{pb}$.

mediators are not considered.

This model depends on the four parameters g_q, g_χ, m_A and m_χ. The two masses can influence the kinematic distributions of the process, which requires an analysis to consider multiple points in the m_A-m_χ-plane. The two couplings g_q and g_χ, on the other hand, only scale the total cross section, as long as they correspond to a sufficiently narrow decay width. For the tree-level production as shown in Figure 2.3, this corresponds to a quadratic scaling in both couplings:

$$\sigma(q\bar{q} \to A \to \chi\bar{\chi}) \propto g_q^2 g_\chi^2 \tag{2.18}$$

A promising alternative for the "portal" between the Standard Model particles and dark matter is the Higgs boson [24]. As we know it to couple to fermions proportionally to their mass (Equation 2.13), it should couple to any fermionic dark matter. The Higgs boson could be produced via the known processes of gluon-gluon fusion, vector boson fusion or Higgs radiation, as depicted in Figure 2.4, and then decay into dark matter.

The Standard Model, on the other hand, only predicts an invisible final state of the Higgs boson if it decays into two Z bosons, which subsequently decay into four neutrinos. This results in a small branching ratio of $\text{BR}^{\text{SM}}(h \to \text{inv}) = 1.06 \times 10^{-3}$ [25] and at the time of writing this thesis, invisible Higgs decays have not yet been observed [26]. More precise measurements are thus interesting in order to test the Standard Model prediction. The results in this thesis are also interpreted in terms of invisible Higgs decays to set upper limits on $\text{BR}(h \to \text{inv})$.

As stated in Section 2.1.2, the Higgs doublet in the Standard Model only represents the minimal model necessary to generate the fermion and boson masses. Several extensions to this choice, like the two-Higgs-doublet [27] or the electroweak-singlet model [28], introduce a new heavy, Higgs-like scalar. Such a scalar could be produced in p-p collisions analogously to the Standard Model Higgs boson and be observable as a resonance in the s-channel production of Z boson pairs. The third interpretation of the results in this thesis is performed in the framework of a search for such a heavy Higgs-like scalar H. Its existence is not necessarily tied to dark matter, but there are renormalizable dark matter models proposed which include such a second Higgs doublet [29].

2.3 Mono-X Signatures

Searching for a completely invisible final state is not possible in a collider experiment as it cannot be distinguished from no event at all. At least one additional visible particle in the final state is necessary that will recoil against seemingly nothing in the detector. Depending on the choice of the recoiling object X, this signature is referred to as mono-X. It is widely used in dark matter searches, with typical choices for X being a jet, photon, Higgs-, W- or Z-boson [30–34].

The primary discriminating variable of such a signature is *missing transverse momentum*. In a proton-proton collision the initial longitudinal momentum of the interacting partons along the beam line is unknown, as each parton can carry an arbitrary fraction x of the proton's momentum. Only the transverse momentum p_{T} of the partons is known to be zero, which implies that the vectorial sum of the final state particles' transverse momenta must be zero as well. If some particles leave the detector unseen, this is no longer true and the remaining difference is the missing transverse momentum. In the following, it is called *missing transverse energy* and denoted by $\vec{E}_{\mathrm{T}}^{\mathrm{miss}}$ with its absolute value $E_{\mathrm{T}}^{\mathrm{miss}}$. The choice of energy instead of momentum here reflects that, in experiments, usually calorimetric measurements in combination with tracking information are used to evaluate the balance, as described in Chapter 5.6.

Disregarding detector acceptance, inefficiencies and resolution, missing transverse energy in the Standard Model can only be caused by neutrinos. In order to be sensitive to new invisible particles, like WIMPs, mono-X searches select events with large $E_{\mathrm{T}}^{\mathrm{miss}}$ and a correspondingly large transverse momentum p_{T} of the recoil partner. In this thesis, a mono-jet and a mono-Z analysis are performed. WIMP production via an axial-vector mediator as depicted in Figure 2.3 can be detected if one of the incoming quarks radiates a gluon or a Z boson respectively. For the invisible Higgs decay, the mono-jet search is mainly sensitive to the vector-boson fusion (Figure 2.4(b)) and the gluon-gluon fusion (Figure 2.4(a)) if one of the incoming gluons or the internal quark loop radiates an additional gluon. The mono-Z search is directly sensitive to the Higgs radiation in Figure 2.4(c). Both signatures are sensitive to a heavy ZZ resonance where one Z boson decays into neutrinos to create the $E_{\mathrm{T}}^{\mathrm{miss}}$. If the other Z boson decays hadronically it can create the mono-jet signature. If it decays into a e^+e^- or $\mu^+\mu^-$ pair, the mono-Z analysis is sensitive instead.

3 Unfolding

3.1 Motivation

The ATLAS experiment was designed to test the Standard Model in a large variety of processes. As long as no significant deviation in a selected one is found, exclusion limits on theories beyond the Standard Model can be derived. The prevalent procedure of this is depicted in Figure 3.1. Our understanding of nature in form of the Standard Model is used to generate Monte Carlo events. Events at this stage are typically referred to as *truth level* or *particle level*[1]. Our data, on the other hand, is defined on the so-called *reconstruction level* or *detector level*, as we can only study what was seen by the detector and reconstructed afterwards. It is altered by detector effects like resolution, non-linear response, missed particles or ambiguities in their reconstruction in comparison to the particle level.

Hence, events need to be transferred to the same level in order to compare Standard Model predictions to data. In a common search on reconstruction level, this is done by passing the accordingly generated Monte Carlo events through a simulation of the detector and its reconstruction algorithms. Additionally, Monte Carlo events according to the new physics model in question are generated for given model parameters and inserted into the detector simulation. The resulting event yield is then added to the Standard Model contribution and compared to the data. This procedure limits the possibility of theorists to check their own models against observations as a simulation of the used detector is necessary. The latter is usually not publicly available and also computationally very demanding. Theorists thus need to rely on the experimentalists to constrain their models or resort to approximations of the detector response [35] with the accompanied additional uncertainties. The experimentalists, on the other hand, cannot check every proposed model in every analysis of a certain final state and phase space. This way, constraining future models would essentially require to repeat already published searches.

Currently, this problem is mitigated by the use of *simplified models* [36]. They offer an effective Lagrangian at the TeV-scale including only a few new particles and interactions. They can also be easily expressed in terms of observables like particle masses and decay widths, production cross sections and branching ratios. Simplified models often represent limits of more general theories beyond the Standard Model with most of the new particles integrated out. This aims at selecting a manageable amount of models sensitive to certain detector signatures.

Experimentalists now use those benchmark models and derive limits on their cross

[1] The term particle level implies, that the hadronization of quarks and gluons as well as soft final state radiation is included in the simulated events. If only the direct products of the hard scatter are considered, one refers to this as *parton level*. In this thesis, only truth information on particle level is used.

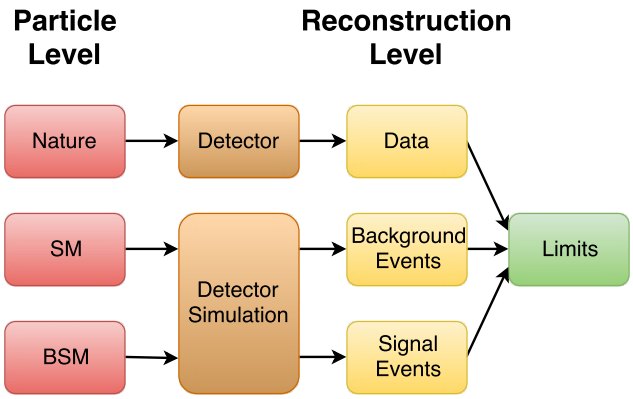

Figure 3.1: Workflow of a search for physics beyond the Standard Model (BSM) on reconstruction level. Both the SM and BSM predictions need to be passed through a detector simulation in order to constrain the considered BSM model by data.

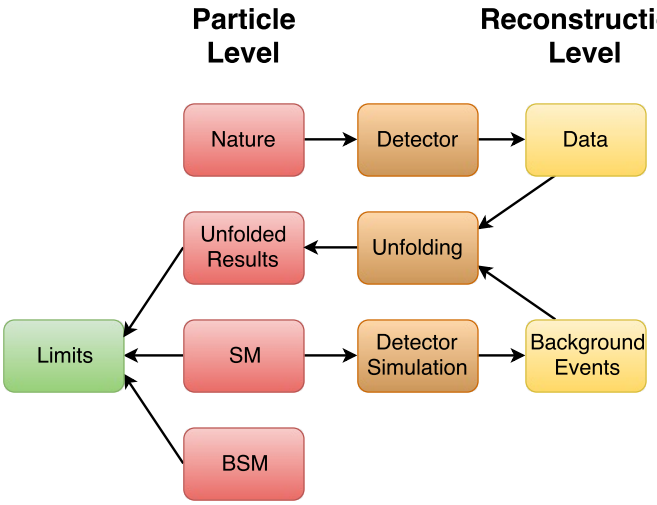

Figure 3.2: Workflow of a search for physics beyond the Standard Model (BSM) on particle level. The data is unfolded under the assumption of SM-like behavior. The result on particle level can then be used to constrain any BSM model without the need of a detector simulation.

sections. Theorists can simplify their specific models by replacing complex interactions by effective ones and thereby reducing the parameter space to a projection of the specific model on the nearest simplified model. The experimental limits can then be used to constrain their original model. However, the loss of information associated with the detour via simplified models usually results in weaker limits than a direct test of the more general model in question [36].

An elegant alternative to the approach of simplified models is given by *unfolding*, as sketched in Figure 3.2. It aims at removing the detector effects from the observed data and determine their underlying particle level distributions. This allows theorists to derive limits on their complex models and to consider different signatures simultaneously as well as different experimental sources, like ATLAS, CMS and cosmological constraints.

3.2 Bayes' Theorem

This section describes the Bayesian approach to infer particle level information from reconstruction level observables. To do so, the detector response for particle level events must be known. It can be evaluated by Monte Carlo events before and after the detector simulation, as they carry information about both levels. This approach relies on an accurate description of the detector by its simulation, but so does a common search on reconstruction level.

Consider a distribution of a kinematic variable with a binning $\{T_j\}$ on particle level (or truth level, hence the acronym) and $\{R_i\}$ on reconstruction level. For now assume, that every event falls exactly into one particle level bin and one reconstruction level bin, meaning there are no inefficiencies in the detector. A truth event belonging into bin T_j will then fall into a certain bin R_i after the detector simulation. As the detector response is a statistical process, a second event from bin T_j may end up in another bin R_k. Given a sufficient set of Monte Carlo events, one can fill the *migration matrix* A with its elements A_{ij} counting how many events fall into both T_j and R_i. Normalizing the migration matrix to unity along the reconstruction axis yields an estimate for the *folding probability* of an event from bin T_j to be propagated into R_i:

$$\mathrm{P}\big(R_i \,|\, T_j\big) = \frac{A_{ij}}{n\big(T_j\big)}\,, \tag{3.1}$$

where $n\big(T_j\big)$ denotes the total number of events in bin T_j. The number of events in bin R_i can now be derived by *folding* (convolving) the event counts on particle level with these probabilities:

$$n(R_i) = \sum_j \mathrm{P}\big(R_i \,|\, T_j\big)\, n\big(T_j\big)\,. \tag{3.2}$$

This way, $\mathrm{P}\big(R_i \,|\, T_j\big)$ can be interpreted as the folding matrix P_{ij} transferring a vector of events on particle level to a vector of events on reconstruction level. To reverse this, i.e. to *unfold* (deconvolve), one could naively create the unfolding matrix $\tilde{P}$ by inverting the folding matrix.

However, the inversion disregards the intrinsic probabilistic nature of this process. Deriving the unfolded vector with this matrix results in a strong enhancement of statistical fluctuations, strongly anticorrelated neighboring bins and potentially unphysical distributions. The flaw in this method becomes obvious in a case where P is singular, such that $\tilde{P}$ cannot be derived, or where negative terms in $\tilde{P}$ result in negative event counts in some bins. To correctly reverse the folding, Bayes' theorem states how a conditional probability can be inverted:

$$\tilde{P}_{ij} = \mathrm{P}\big(T_j \,|\, R_i\big) = \frac{\mathrm{P}\big(R_i \,|\, T_j\big)\,\mathrm{P}\big(T_j\big)}{\mathrm{P}\big(R_i\big)} = \frac{\mathrm{P}\big(R_i \,|\, T_j\big)\,\mathrm{P}\big(T_j\big)}{\sum_k \mathrm{P}\big(R_i \,|\, T_k\big)\,\mathrm{P}\big(T_k\big)}\,, \tag{3.3}$$

where $\mathrm{P}\big(T_j\big)$ and $\mathrm{P}\big(R_i\big)$ denote our *prior* knowledge about the probability of an event to fall into T_j or R_i respectively. $\mathrm{P}\big(R_i\big)$ can be expressed in terms of $\mathrm{P}\big(T_j\big)$ by summing

over all truth bins and multiplying their prior with the corresponding folding probability, analogous to Equation 3.2:

$$\mathrm{P}(R_i) = \sum_j \mathrm{P}\big(R_i \,|\, T_j\big)\, \mathrm{P}\big(T_j\big)\,. \tag{3.4}$$

Since our best knowledge of the distribution on particle level is given by the Monte Carlo events generated according to the Standard Model, these can be used to express our prior $\mathrm{P}\big(T_j\big)$:

$$\mathrm{P}\big(T_j\big) = \frac{n\big(T_j\big)}{\sum_k n(T_k)} \tag{3.5}$$

With these results, the unfolding probability in Equation 3.3 can be expressed as

$$\mathrm{P}\big(T_j \,|\, R_i\big) = \frac{A_{ij}}{n(R_i)}\,, \tag{3.6}$$

showing complete analogy to Equation 3.1 as to be expected. This allows propagating events from reconstruction level to particle level via

$$n\big(T_j\big) = \sum_i \mathrm{P}\big(T_j \,|\, R_i\big)\, n\big(R_i\big)\,. \tag{3.7}$$

For Monte Carlo distributions, this relation is trivial as one ends up with the exact same $n\big(T_j\big)$ that has been inserted in the beginning. But one can now also insert the observed data as $n(R_i)$ while using $\mathrm{P}\big(T_j \,|\, R_i\big)$ evaluated from the Monte Carlo events to get the unfolded observed distribution:

$$n_{\mathrm{unf}}\big(T_j\big) = \sum_i \frac{A_{ij}}{n_{\mathrm{mc}}(R_i)}\, n_{\mathrm{obs}}(R_i)\,. \tag{3.8}$$

So far, we disregarded detector inefficiencies and thus only considered events occupying one bin on both reconstruction and particle level. However, a failed reconstruction of particles, their misidentification (e.g. a photon as an electron), or the smearing due to the detector resolution can result in an event being accepted by the selection criteria on one level and rejected on the other. An event accepted on particle level, that is falsely rejected on reconstruction level, is commonly referred to as a *miss*. Conversely, an event accepted only on reconstruction level is labeled as *fake*.

One way to think of this is to expand both the reconstruction and particle level by one additional bin containing those events, as depicted in Figure 3.3. Let N_T denote the number of original bins on particle level and N_R on reconstruction level, respectively. By identifying $A_{i,N_T+1} \equiv n_{\mathrm{fake}}(R_i)$ and $A_{N_R+1,j} \equiv n_{\mathrm{miss}}\big(T_j\big)$ and including these new bins in the sums, the validity of Equations 3.1 to 3.6 is preserved. Equation 3.7, however, cannot be applied to data anymore, as the number of missed events $n_{\mathrm{obs}}(R_{N_R+1})$ is unknown. This can be solved by summing over the original bins only and applying an efficiency ϵ_j

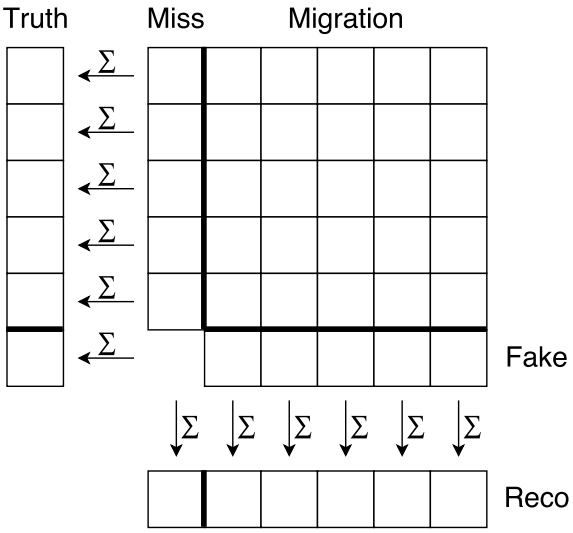

Figure 3.3: Visualization of the handling of fakes and misses by adding an additional bin on reconstruction and particle level. The missed events are those which do not correspond to a valid bin on reconstruction level, the fakes do not correspond to a valid bin on truth level.

per particle level bin:

$$\epsilon_j = \sum_{i=1}^{N_R} \mathrm{P}\big(R_i \,|\, T_j\big) = \frac{\sum_{i=1}^{N_R} A_{ij}}{n_{\mathrm{mc}}\big(T_j\big)} \tag{3.9}$$

$$\begin{aligned} n_{\mathrm{unf}}\big(T_j\big) &= \frac{1}{\epsilon_j} \sum_{i=1}^{N_R} \mathrm{P}\big(T_j \,|\, R_i\big)\, n_{\mathrm{obs}}(R_i) \\ &= \frac{1}{\epsilon_j} \sum_{i=1}^{N_R} \frac{A_{ij}}{n_{\mathrm{mc}}(R_i)}\, n_{\mathrm{obs}}(R_i)\,. \end{aligned} \tag{3.10}$$

This result is equivalent to correcting $n_{\mathrm{obs}}(R_i)$ for fakes, then unfold according to Equation 3.8 and finally correct $n_{\mathrm{unf}}\big(T_j\big)$ for misses, which is used in the IDS algorithm described in Section 3.4.

3.3 Iterative Bayesian Unfolding

Following a Bayesian approach, one had to assume a prior $\mathrm{P}\big(T_j\big)$ for the particle level distribution in Equation 3.3. Using the Monte Carlo distribution is the correct starting point, but if there are effects of nature unconsidered in our model, this introduces a *bias*. In this case, the resulting unfolded distribution will not completely represent the true distribution. One way to deal with this is an iterative approach to update the choice of the prior [37]. After the unfolding step according to Equation 3.8, the unfolded distribution carries information from the observed data and should thus be able to replace the initial choice of the prior. The updated prior then falls between the initial choice and its true distribution, which can be checked in simulated data. This suggests an

iterative update of the prior, the corresponding unfolding probability and the unfolded distribution. The algorithm for *iterative Bayesian unfolding* then looks as follows:

$$\mathrm{P}^{(1)}\big(T_j\big) = \frac{n_{\mathrm{mc}}\big(T_j\big)}{\sum_{k=1}^{N_T+1} n_{\mathrm{mc}}(T_k)} \tag{3.11}$$

$$\mathrm{P}^{(r)}\big(T_j|R_i\big) = \frac{\mathrm{P}\big(R_i \,|\, T_j\big)\, \mathrm{P}^{(r)}\big(T_j\big)}{\sum_{k=1}^{N_T+1} \mathrm{P}\big(R_i \,|\, T_k\big)\, \mathrm{P}^{(r)}(T_k)} \tag{3.12}$$

$$n_{\mathrm{unf}}^{(r)}\big(T_j\big) = \frac{1}{\epsilon_j} \sum_{i=1}^{N_R} \mathrm{P}^{(r)}\big(T_j|R_i\big)\, n_{\mathrm{obs}}(R_i) \tag{3.13}$$

$$\mathrm{P}^{(r+1)}\big(T_j\big) = \frac{n_{\mathrm{unf}}^{(r)}\big(T_j\big)}{\sum_{k=1}^{N_T+1} n_{\mathrm{unf}}^{(r)}(T_k)}\,, \tag{3.14}$$

where r indicates the current iteration, starting at 1. $\mathrm{P}\big(R_i \,|\, T_j\big)$ is defined as before and kept constant across iterations in order not to influence the detector response. Repeatedly updating $\mathrm{P}\big(T_j\big)$ decreases the influence of the initial choice of the prior and thus also the bias. However, the statistical uncertainties increase at the same time. Fluctuations present in the migration matrix and the data itself leave an imprint on the updated prior which is enhanced with every iteration. This feedback loop lets the unfolding matrix converge towards the initially discarded naive inverse of the folding matrix as all information from the initial prior is lost. An appropriate tradeoff between tolerated bias and statistical uncertainties needs to be found, which is done by the choice of the so-called *regularization*. In this iterative unfolding procedure, limiting the number of iterations is the straightforward way to regularize. In some applications, an additional smoothing of the prior between iterations is used.

3.4 Iterative, Dynamically Stabilized Unfolding

3.4.1 Algorithm

A sophisticated way of regularization is given by the iterative, dynamically stabilized (IDS) unfolding presented in Reference [38]. Again, detector inefficiencies are disregarded for now, a correction is applied afterwards.

The starting point is the difference $\Delta(R_i) = n_{\mathrm{obs}}(R_i) - n_{\mathrm{mc}}(R_i)$ between the observed distribution and its Monte Carlo expectation on reconstruction level (after a normalization procedure). In an artificial case of vanishing difference in every bin, the unfolded result can be set exactly to the Monte Carlo truth distribution, as the latter is able to perfectly explain the observed data. In a real-world application, however, some deviations between observation and prediction are to be expected due to statistical fluctuations or due to effects in the data which are not considered in the model. These differences need to be unfolded to improve our particle level distribution accordingly. Doing this directly with

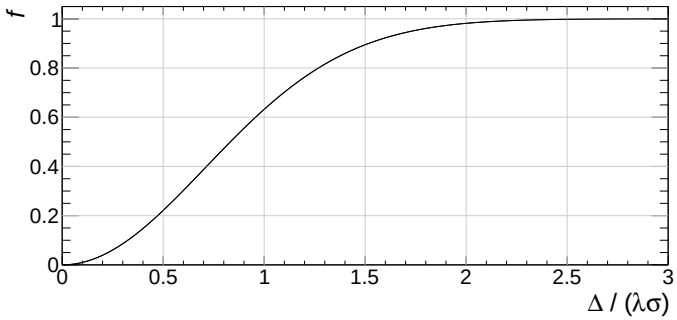

Figure 3.4: $f = 1 - e^{-\left(\frac{\Delta}{\lambda\sigma}\right)^2}$ as regularization function.

the unfolding matrix from Equation 3.3 would be equivalent to Bayesian unfolding:

$$\begin{aligned} n_{\text{unf}}(T_j) &= n_{\text{mc}}(T_j) + \sum_i \tilde{P}_{ij} \left(n_{\text{obs}}(R_i) - n_{\text{mc}}(R_i) \right) \\ &= n_{\text{mc}}(T_j) + \sum_i \tilde{P}_{ij}\, n_{\text{obs}}(R_i) - n_{\text{mc}}(T_j) = n_{\text{unf}}^{\text{Bayes}}(T_j)\,. \end{aligned} \tag{3.15}$$

The novelty of IDS unfolding is a weighting of the differences according to their statistical significance. This aims at unfolding possibly significant new structures in the data while fluctuations with low significance remain comparably untouched, preventing them from an enhancement in further iterations. The continuous distinction into insignificant and significant is implemented by a regularization function f. It assigns a weight between 0 and 1 to any bin-wise deviation $\frac{\Delta}{\sigma\lambda}$ between two distributions, using the difference Δ scaled by its statistical uncertainty σ and a global regularization parameter λ. Different values for this regularization parameter are used in various steps of the algorithm, in the following denoted by λ_U, λ_N, etc. A variety of choices for the regularization function is possible, as long as they are smooth and monotonically increasing from 0 to 1. In this thesis,

$$f = 1 - e^{-\left(\frac{\Delta}{\lambda\sigma}\right)^2} \tag{3.16}$$

as shown in Figure 3.4 is used.

A large λ results in overall lower weights and in deviations being interpreted as less significant. Conversely, a small λ has the opposite effect. Including this weighting (and the Monte Carlo normalization factor C_{norm} which is explained afterwards), the unfolding formula changes to

$$n_{\text{unf}}(T_j) = C_{\text{norm}} \cdot n_{\text{mc}}(T_j) + \sum_i \left(f_i^{\lambda_U} \cdot \Delta(R_i) \cdot \tilde{P}_{ij} + \left(1 - f_i^{\lambda_U}\right) \cdot \Delta(R_i) \cdot \delta_{ij} \right), \tag{3.17}$$

where $\Delta(R_i)$ denotes the difference between observation and expectation in reconstruction bin i, and f_i^{λ} the evaluation of the regularization function in this bin with given

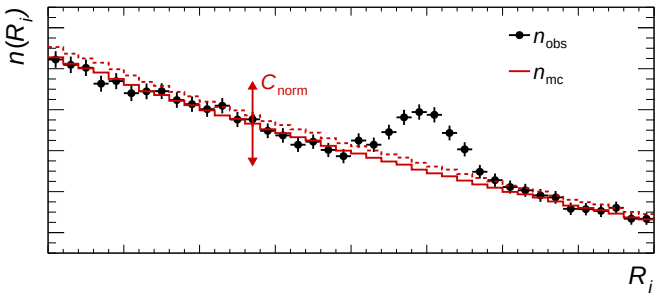

Figure 3.5: Influence of the normalization factor C_{norm} in a toy experiment with unexpected structure present in the data. The red dashed line indicates the normalization that would be found by the naive normalization, which creates a systematic deviation in every bin. Instead, the solid red line corresponds to the correct normalization that removes the systematic deviation in the well-modeled region.

regularization parameter λ:

$$f_i^{\lambda} = f\left(\frac{\left|\Delta(R_i)\right|}{\lambda\sigma(R_i)}\right) \tag{3.18}$$

$$\Delta(R_i) = n_{\text{obs}}(R_i) - C_{\text{norm}}\, n_{\text{mc}}(R_i) \tag{3.19}$$

$$\sigma(R_i) = \sqrt{\sigma^2_{\text{obs}}(R_i) + C^2_{\text{norm}}\, \sigma^2_{\text{mc}}(R_i)}\,. \tag{3.20}$$

In this formulation, an identical binning on particle and reconstruction level is required. If that is not the case, δ_{ij} must be replaced by a rebinning transformation. The uncertainty $\sigma(R_i)$ on the difference is evaluated by assuming Gaussian profiles for $n_{\text{obs}}(R_i)$ and $n_{\text{mc}}(R_i)$ and propagating their uncertainties accordingly.

This way, no longer the full difference between data and the Monte Carlo expectation in a given bin is migrated according to $\tilde{P}$ but only a fraction $f_i^{\lambda_U}$. The remaining part $\left(1 - f_i^{\lambda_U}\right)$ remains untouched in the original bin. Decreasing λ_U increases the amount of migration in this step, with the limit $\lambda_U \to 0$ retrieving Bayesian unfolding.

The normalization factor C_{norm} allows a global scaling of the Monte Carlo expectation to get the best possible agreement between observation and expectation. The naive implementation $C_{\text{norm}} = \sum_i n_{\text{obs}}(R_i) / \sum_i n_{\text{mc}}(R_i)$ achieves this only if the shape of the observed distribution is correctly represented by the Monte Carlo. If, for example, an additional peak is present in the data, this would increase C_{norm} and artificially create a mismatch in all bins as can be seen in Figure 3.5. To avoid this, the normalization procedure estimates the amount of data events $N^{\text{est}}_{\text{obs}}$ which can be described by the expected shape. Contributions of significant deviations indicating an unknown structure are disregarded, again by utilizing the regularization function. An iterative approach is chosen to minimize the discrepancy between the two distributions, starting at the naive implementation mentioned above:

$$\left(N_{\text{obs}}^{\text{est}}\right)^{(1)} = \sum\nolimits_i n_{\text{obs}}(R_i) \tag{3.21}$$

$$C_{\text{norm}}^{(r)} = \frac{\left(N_{\text{obs}}^{\text{est}}\right)^{(r)}}{\sum_i n_{\text{mc}}(R_i)} \tag{3.22}$$

$$\left(N_{\text{obs}}^{\text{est}}\right)^{(r+1)} = \left(N_{\text{obs}}^{\text{est}}\right)^{(r)} + \sum\nolimits_i \left(1 - f_i^{\lambda_N}\right) \Delta^{(r)}(R_i)\,. \tag{3.23}$$

It typically converges very quickly and can be tuned independently by the parameter λ_N.

Between the unfolding iterations, an update of the unfolding matrix $\tilde{P}$ corresponding to the update of the prior in the Bayesian algorithm is applied. And again, the extent of this modification is regularized by f

$$\tilde{P}'_{ij} = \frac{A'_{ij}}{\sum_k A'_{ik}} \tag{3.24}$$

$$A'_{ij} = A_{ij} + f_j^{\lambda_M} \frac{\Delta\left(T_j\right)}{C_{\text{norm}}} P_{ij} \tag{3.25}$$

$$\Delta\left(T_j\right) = n_{\text{unf}}\left(T_j\right) - C_{\text{norm}}\, n_{\text{mc}}\left(T_j\right)\,, \tag{3.26}$$

where $\Delta\left(T_j\right)$ denotes the deviation of the unfolded result from the particle level Monte Carlo distribution and f_j^{λ} the evaluation of f with this difference[2]. Equation 3.25 can be understood as propagating the update of the prior $f_j^{\lambda_M}\,\Delta\left(T_j\right)/C_{\text{norm}}$ into the migration matrix to update the unfolding probability. As in this formulation the migration matrix itself is altered, which depends on the prior *and* the detector response, caution is necessary. Only the prior is supposed to be updated between iterations, the response is assumed to be perfectly known and shall remain unchanged. In this case, that is achieved by altering the migration matrix for the evaluation of $\tilde{P}_{ij}$ only. The folding probability P_{ij} is not updated and will always be given by the initial migration matrix:

$$P_{ij} = \frac{A_{ij}^{\text{mc}}}{\sum_k A_{kj}^{\text{mc}}}\,. \tag{3.27}$$

Regularizing the extent of the update by the parameter λ_M retrieves the Bayesian algorithm in the limit $\lambda_M \to 0$.

In Reference [38], an additional procedure for fluctuations due to background subtraction is described. As no background subtraction is performed in this thesis, the mechanism is disabled by setting the corresponding regularization parameter λ_S to ∞.

Missed events are accounted for by scaling the unfolded result by $1/\epsilon_j$ like in the Bayesian algorithm. Fakes are handled analogously by a bin-wise correction of the observed distribution with the factor $\sum_{j=1}^{N_T} A_{ij}/n_{\text{mc}}(R_i)$. Analytically, this is equivalent to the introduction of an additional particle level bin and subsequent adjustment of the unfolding probability [38].

[2] For the evaluation of f_j^{λ}, the uncertainty $\sigma_{\text{unf}}\left(T_j\right)$ of the unfolded result is necessary. This could in principle be evaluated by toys with the bootstrapping method introduced in Section 3.5. To avoid the additional computational complexity, the code implementation approximates $\sigma_{\text{unf}}\left(T_j\right)$ by $\sigma_{\text{obs}}(R_i)$ in the case of identical binning on truth and reconstruction level. An overall scaling factor of the uncertainty can be absorbed into the choice of the regularization parameter λ_M, only bin-wise effects are lost this way. The overall impact of this approximation is estimated to be small [39].

3.4.2 Choice of Parameters

With the algorithm as described above, four parameters remain to be fixed: λ_U, λ_N, λ_M and the number of iterations. In a dedicated analysis to search for new physics, these should be studied separately in pseudo experiments to judge the introduced bias and the sensitivity to injected signals. In this thesis, these steps are omitted because ultimately only relative differences between individual and combined signatures are analyzed and absolute results are secondary. Instead, the chosen parameters are based on the detailed example provided in Reference [38].

If no background subtraction is performed, as it is the case for the applications in this thesis, no strong dependence on λ_N for values $\lambda_N \gtrsim 1$ is found. In the following, $\lambda_N = 5$ is used. The example also suggests small values of λ_M and λ_U to achieve a best possible agreement between the true distribution and the unfolded result. This corresponds to a conservative approach of low regularization.

In the following, $\lambda_M = 0$ is chosen[3], meaning no regularization is applied to the update on the unfolding matrix such that the Bayesian update of the prior is retrieved. The regularization is solely achieved by λ_U.

The first iteration can be performed with $\lambda_U = 0$ since the prior is evaluated only by the Monte Carlo estimate at this point and no fluctuations from the data can be enhanced yet. This opposes the choice of a large λ_U for the first iteration in Reference [38] which is necessary to correctly handle background subtraction. For all following iterations, a value of $\lambda_U = 0.5$ is selected. This corresponds to a weight of $f \approx 98\,\%$ for deviations of $\Delta = 1\sigma$ and a drop to a weight of $f \approx 50\,\%$ for deviations of $\Delta \approx 0.42\sigma$.

The total number of iterations is tested individually for both applications (Sections 6.6 and 7.6) and found to be 4 and 3, respectively, in order to reach a stable result. As they rely on a very coarse binning in comparison to the example in Reference [38] and correspondingly have smaller migrations, the result is less dependent on the exact choice of parameters. This is shown for the number of iterations in Sections 6.6 and 7.6 and has been verified for the other parameters in a similar manner.

3.5 Uncertainty Propagation

The procedure of unfolding an observed distribution to particle level requires to handle the uncertainties differently than in a common search on reconstruction level. As every observed event is split into varying contributions to several particle level bins and overall efficiency corrections are applied during the unfolding, the probability density of the unfolded result $p\big(n_{\text{unf}}(T_j)\big)$ cannot be assumed Poissonian anymore, unlike $p\big(n_{\text{obs}}(R_i)\big)$ which corresponds to a counting experiment. Additionally, the splitting of events causes correlations between bins in the unfolded distribution. In Reference [37], the covariance between two unfolded bins after Bayesian unfolding is derived, including possible correlations present in the migration matrix.

Due to the increased complexity of the IDS unfolding algorithm, an analytic description of the uncertainty propagation seems more involved. In this thesis, a sampling approach referred to as *bootstrapping* [40], is employed to create replicas of histograms. For each

[3] In fact, $f_j^{\lambda_M}$ is set to 1 instead in order to not divide by 0.

event (both observed and in Monte Carlo simulation) that would fill a certain bin R_i or T_j, N Poissonian distributed integers $\mathcal{P}_r(1)$ around a mean of 1 are generated[4]. These are used to fill the event $\mathcal{P}_r(1)$ times into the corresponding bin $R_i^{(r)}$ or $T_j^{(r)}$ for replicas $r = 1, ..., N$ of the histogram. The random number generation is seeded by the unique event ID, such that e.g. correlations due to a single event appearing in multiple signal regions are preserved. This is done for the distributions on particle and reconstruction level and the migration matrix. All unfolding steps in the algorithms mentioned above are then executed for each replica separately, resulting in N unfolded distributions. Those can be used as a sample to estimate the variance in each bin and the covariance between them:

$$\begin{aligned} \mathrm{cov}_{i,j} &= \left\langle \Big(n_{\mathrm{unf}}(T_i) - \big\langle n_{\mathrm{unf}}(T_i)\big\rangle\Big)\Big(n_{\mathrm{unf}}(T_j) - \big\langle n_{\mathrm{unf}}(T_j)\big\rangle\Big) \right\rangle \\ &= \frac{1}{N}\sum_{r=1}^{N}\Big(n_{\mathrm{unf}}^{(r)}(T_i) - \big\langle n_{\mathrm{unf}}(T_i)\big\rangle\Big)\Big(n_{\mathrm{unf}}^{(r)}(T_j) - \big\langle n_{\mathrm{unf}}(T_j)\big\rangle\Big) \end{aligned} \tag{3.28}$$

Systematic uncertainties are handled by separately unfolding varied distributions as described in Chapter 6.

3.6 Topology Unfolding

Most applications of unfolding in ATLAS searches so far employ a background subtraction. Usually, the dominant Standard Model background is labeled as the signal process while all other backgrounds on reconstruction level are subtracted from the observed distribution:

$$n_{\mathrm{obs}}^{\mathrm{subt}}(R_i) = n_{\mathrm{obs}}(R_i) - \sum_{\mathrm{bkg}} n_{\mathrm{mc}}^{\mathrm{bkg}}(R_i)\,. \tag{3.29}$$

The unfolding is then performed on this background-subtracted observed distribution, using only the response of the selected signal process: A_{ij}^{sig}, $n_{\mathrm{mc}}^{\mathrm{sig}}(R_i)$ and $n_{\mathrm{mc}}^{\mathrm{sig}}(T_i)$.

In this thesis, on the other hand, the novel method of *topology unfolding* is used, where all processes present in the selected topology are added up to form A_{ij}^{topo}, $n_{\mathrm{mc}}^{\mathrm{topo}}(R_i)$ and $n_{\mathrm{mc}}^{\mathrm{topo}}(T_i)$. These are then used to unfold the complete observed distribution.

It has been shown in a mono-jet search [41], that the results are consistent with the common way of unfolding. The uncertainties can even be reduced as the statistical uncertainty of the migration matrix is reduced by considering more events. At the same time, it allows to separate the theoretical uncertainties on the cross sections of the individual background processes from the unfolded result. In the standard way, they influence the normalization of the background to be subtracted and thus also the resulting $n_{\mathrm{obs}}^{\mathrm{subt}}(R_i)$. In the topology unfolding, they only influence the relative amount of each process in the total migration matrix. As long as their responses do not strongly differ from each other, this results only in a minor effect on the unfolded result. Instead, the theoretical uncertainties can be applied to the particle level Monte Carlo predictions that

[4] All applications in this thesis generate $N = 1000$ replicas.

the unfolded result is compared to. This allows for a clean separation of the experimental and theoretical uncertainties and creates the possibility to update the latter in case of new results.

4 The ATLAS Experiment

The studies in this thesis are based on proton-proton collisions at a center-of-mass energy of $\sqrt{s} = 13\,\text{TeV}$[1] from 2015, produced by the Large Hadron Collider (LHC) and recorded by the ATLAS detector at CERN[2], Geneva. This chapter provides a general overview of the experimental setup. The overall accelerator complex and the LHC in particular are described in Section 4.1, the ATLAS detector and its subsystems in Section 4.2.

4.1 The Large Hadron Collider

Colliding protons at $\sqrt{s} = 13\,\text{TeV}$, the LHC is the most powerful particle accelerator to date. It is located in a 27 km long circular tunnel between 45 m and 170 m below the surface of both Switzerland and France. This tunnel was excavated in the 1980s to host the *Large Electron-Positron Collider* (LEP), which became the world's most powerful lepton accelerator ever built, reaching a center-of-mass energy of $\sqrt{s} = 209\,\text{GeV}$ [43]. Using heavy protons instead of light electrons and positrons allows the LHC to vastly exceed the energies reached by LEP, as the synchrotron radiation, which was the limiting factor before, is strongly suppressed[3].

The LHC is capable of colliding protons as well as heavy ions like lead. As only proton-proton collisions are analyzed in this thesis, only their production is described in the following. The filling of the LHC proton beams is achieved by a series of pre-accelerators as illustrated in Figure 4.1. Hydrogen gas serves as the proton source after an electric field strips the electrons from the hydrogen atoms. These protons are accelerated to 50 MeV by the linear accelerator LINAC2. They are then injected into the chain of circular accelerators increasing in diameter, specifically the *Booster* accelerating the protons to 1.4 GeV, the *Proton Synchrotron* (PS) reaching 26 GeV and the *Super Proton Synchrotron* (SPS) reaching 450 GeV before being injected into the LHC ring. The acceleration is performed by superconducting radio frequency cavities that produce standing waves for the protons to travel through. Because of this, the beam cannot be continuous but has to be lumped in *bunches*. They are spaced by 25 ns with each one containing $\mathcal{O}(10^{11})$ protons.

To bend the two highly energetic proton beams into their circular orbit, 1232 superconducting dipole magnets are placed along the tunnel, each one cooled to below 2 K and providing a magnetic field of up to 8.3 T by conducting about 12 kA of current [45]. The maximal magnetic field before risking a quench of the magnets dictates the LHC's design center-of-mass energy of 14 TeV. In addition to the dipole magnets, 858 quadrupole

[1] Mandelstam variable $s = (p_1 + p_2)^2$. For two colliding anti-parallel particles with $E_1 = E_2 \equiv E$ and $m_1, m_2 \ll E$ the center-of-mass energy is given by $\sqrt{s} = 2E$.

[2] Conseil Européen pour la Recherche Nucléaire

[3] A charged particle with energy E and rest mass m moving in a bent trajectory with radius R radiates off power due to synchrotron radiation: $P_{synch} \propto \frac{E^4}{R^2 m^4}$ [44]

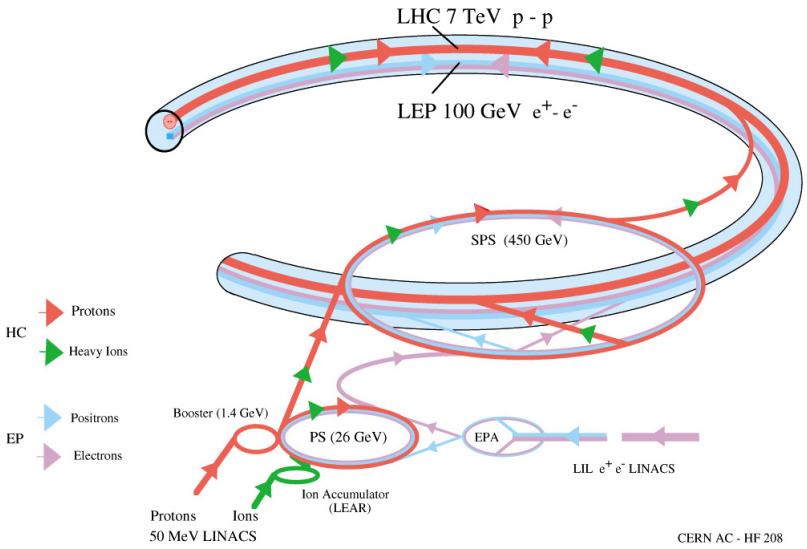

Figure 4.1: Pre-accelerator complex for the LHC. Indicated are the paths of protons and heavy ions that mostly rely on the same accelerators and the energy that a single proton beam reaches in each of the stages. It can also be seen that most of the structure are reused from LEP. [42]

magnets are used to focus the beam. This is done to increases the event rate $\frac{\mathrm{d}N}{\mathrm{d}t}$ which, for a process with given cross section σ, scales with the *luminosity* L at the interaction points:

$$\frac{\mathrm{d}N}{\mathrm{d}t} = L \cdot \sigma \,. \tag{4.1}$$

In a collider experiment with N_i particles contained in each of the two beams, revolving frequency f and a cross section A of the beams at the interaction points, the luminosity is given by:

$$L = \frac{N_1 \cdot N_2 \cdot f}{A} \tag{4.2}$$

which is why a strong focusing of the beams, i.e. minimal A, is essential to provide high event rates. With a design luminosity of $10^{34}\,\mathrm{cm}^{-2}\mathrm{s}^{-1}$, which has even been exceeded by a factor of ≈1.5 by now [46], the LHC sets a new record for hadron colliders. This high event rate comes with the downside of *pile-up*. The expected number of events ranges up to ≈60 for each collision of two bunches (*bunch crossing*), which are observed simultaneously in the detector, imposing major challenges on triggering and reconstruction of the events. L is often also referred to as *instantaneous* luminosity to distinguish it from the *integrated* luminosity:

$$L_{\mathrm{int}} = \int L \,\mathrm{d}t \tag{4.3}$$

There are four locations at the LHC, at which the two particle beams are brought to collision. These interaction points are where the four main experiments are located: ATLAS, ALICE, CMS and LHCb. ATLAS [47] and CMS [48] are both designed as general-purpose detectors to measure final states as inclusively as possible. Their goal

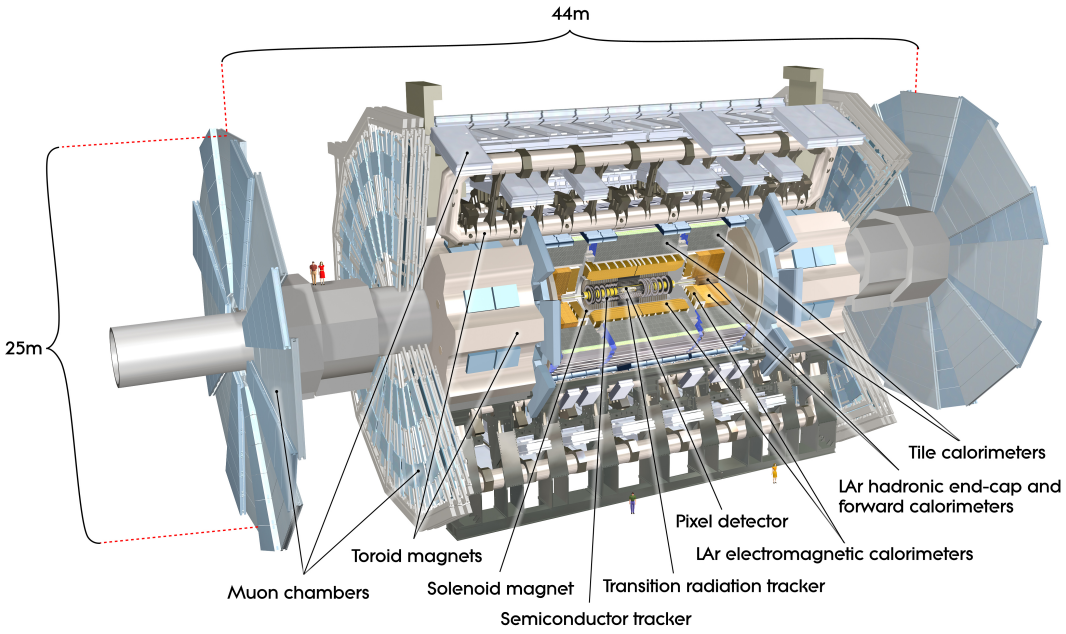

Figure 4.2: Schematic layout of the ATLAS detector. The beams enter from the left and right of the picture to be crossed at the interaction point in the center. Each of the indicated sub-systems is described in Sections 4.2.1 to 4.2.3. [47]

is to precisely test the Standard Model and search for new phenomena. ALICE [49] is specialized in studying the strong interaction in heavy ion collisions that provide especially high energy densities, in particular the deconfinement of quarks and gluons in a plasma. LHCb [50] is a forward spectrometer studying the decay of hadrons containing bottom or charm quarks to measure CP violation.

The proton-proton collisions at a center-of-mass energy of $\sqrt{s} = 13\,\text{TeV}$ analyzed in this thesis correspond to an integrated luminosity of $L_{\text{int}} = 3.2\,\text{fb}^{-1}$. They were recorded in 2015 by the ATLAS detector and on average consist of 13.7 interactions per bunch crossing.

4.2 The ATLAS Detector

The ATLAS detector is a general-purpose detector that is designed to cover as many final states as possible, especially to discover the Higgs boson with its multiple decay channels and perhaps particles beyond the Standard Model. It offers an almost complete 4π coverage of the solid angle, with the only gap being the beam pipe. It uses an onion-shell structure consisting of the inner detector, the calorimeters and the muon system, as illustrated in Figure 4.2, which are discussed in more detail in the following chapters.

The detector's description is based on a right-handed coordinate system with its origin at the interaction point. The z-axis coincides with the beam direction, the x-y-plane is defined transverse to this with the x-axis pointing towards the center of the LHC ring and the y-axis pointing upwards. Transverse quantities like the transverse momentum

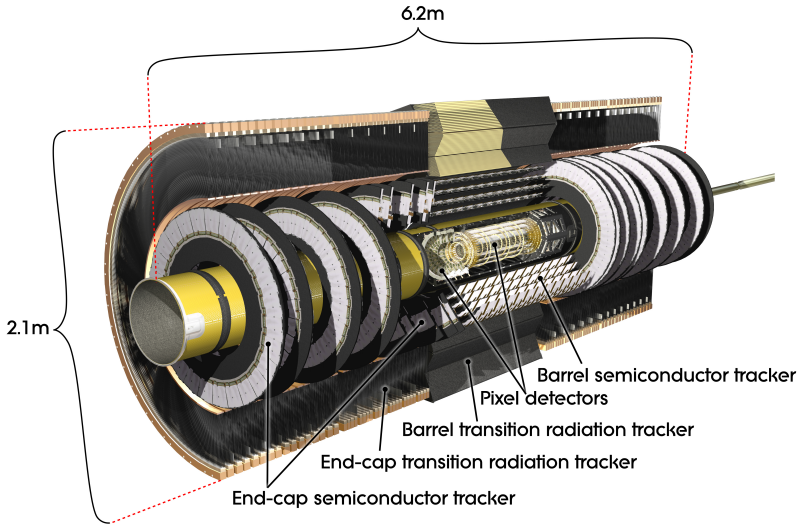

Figure 4.3: Schematic layout of the inner detector of ATLAS. The three main components Silicon Pixel Detector, Semiconductor Tracker and Transition Radiation Tracker are each composed of a central barrel and end-caps for the higher η regions. [47]

or transverse energy are defined as projections onto this plane. The azimuthal angle ϕ measures the angle in this plane towards the positive x-axis. The polar angle θ is defined as the angle towards the positive z-axis. This polar angle is often expressed in terms of the pseudorapidity $\eta = -\ln\left[\tan\left(\theta/2\right)\right]$. Distances between two objects are measured in the η-ϕ-plane as $\Delta R = \sqrt{\Delta\eta^2 + \Delta\phi^2}$. r expresses the radial distance from the z-axis, which is used in most of the technical detector descriptions.

4.2.1 Inner Detector

The inner detector precisely tracks charged particles in the central region $|\eta| < 2.5$. As it is placed in the 2 T magnetic field of a solenoid magnet (Figure 4.2), the trajectories are bent due to the Lorentz force, which allows the momentum calculation from the curvature. By the extrapolation of tracks into the beam pipe, it also enables the association of particles to primary collision vertices or secondary decay vertices of longer-lived particles, like B mesons, which traveled a certain distance. The precise track measurement is achieved by a layered design as depicted in Figure 4.3, consisting of the *Silicon Pixel Detector*, the *Silicon Microstrip Tracker* (labeled as *Semiconductor Tracker* in Figure 4.3) and the *Transition Radiation Tracker*. Each of these subsystems consists of a central barrel surrounding the beam pipe and disk-shaped end-caps placed perpendicular to the beam pipe to cover the higher $|\eta|$ regions.

The innermost Pixel Detector consisting of three identical layers offers the finest resolution with $\approx 10\,\mu\text{m}$ in r-ϕ and $\approx 150\,\mu\text{m}$ in z in the barrel, or respectively in r in the end-caps. This is achieved by semiconducting silicon pixel sensors, whose depletion zones become conductive as transitioning charged particles generate electron-hole pairs, which produces a measurable voltage signal. During the LHC's first long shutdown 2013/2014 the Pixel Detector was upgraded with the *Insertable B-Layer*, an additional

pixel layer inserted between the beam and the original Pixel Detector [51]. It compensates for inevitable radiation damage in the pixel sensors and further increases the tracking precision, which helps to reduce pile-up effects due to the increased instantaneous luminosity.

The Pixel Detector is surrounded by the Silicon Microstrip Tracker made of 4 layers, each featuring pairs of 6 cm long and 80 µm wide microstrips slanted at 40 mrad to each other in order to measure both coordinates. Their alignment parallel to the beam pipe in the barrel results in a resolution of $\approx 17\,\mu\text{m}$ in r-ϕ and $\approx 580\,\mu\text{m}$ in z. In the end-caps they are aligned radially, resulting in the same resolution but in r-ϕ and r, respectively.

The outermost instrumentation of the inner detector, the Transition Radiation Tracker, consists of straw tubes of 4 mm diameter with anode wire tensioned in their centers. A charged particle traversing the tube ionizes the xenon/carbon dioxide gas mixture in its path, resulting in an electron avalanche process due to the high voltage between the anode wire and the straw wall. Like the microstrips, the straw tubes are aligned parallel to the beam in the barrel and radially in the end-caps. The straw tubes do not allow for a measurement of the coordinate along their axis but offer a resolution of 130 µm in r-ϕ in the barrel and in ϕ-z in the end-caps. Although this resolution is worse than for the inner silicon systems, they provide around 36 additional hits per track, improving the precision of the momentum measurement.

Additionally, the Transition Radiation tracker serves the electron identification. The gaps between the straw tubes are filled with polypropylene causing *transition radiation* which occurs when charged particles transit inhomogeneous media. As the transition radiation of a particle with mass m and energy E strongly depends on its Lorentz factor $\gamma = E/m$, it allows distinguishing particles with measured energy according to their mass [52]. As these radiated low-energy photons typically provide much larger signal amplitudes in the straw tubes than traversing minimum-ionizing charged particles, the transition radiation can be filtered in the readout to be analyzed separately.

Including the Insertable B-Layer, the resolution of the vertex reconstruction by the inner detector was found to be between 160 µm and 20 µm in transversal direction and between 340 µm and 40 µm longitudinally, improving with the number of tracks [53]. A relative momentum resolution $\sigma_p/p = (4.83 \pm 0.16) \cdot 10^{-4} \cdot p_\text{T}\,[\text{GeV}]$ has been measured in the study of cosmic rays [54].

4.2.2 Calorimeter

The tracking detector and its solenoid magnet are surrounded by the ATLAS calorimetry system. It is used to stop the majority of the particles exiting the tracker (except muons and neutrinos) and to measure their deposited energy. The calorimeter also contributes to the particle identification by measuring the distinct shower shapes. It consists of two major layers: the inner *electromagnetic* (EM) layer, optimized for electrons and photons, and the outer *hadronic* (Had) layer for hadronic activity. A schematic overview of its subsystems is given in Figure 4.4.

The electromagnetic layer is separated into the EM Barrel covering $|\eta| < 1.475$ and the EM End-Caps covering $1.375 < |\eta| < 3.2$. Both rely on lead absorbers and liquid argon as active material. Lead strips (between 1.1 mm and 2.2 mm thick) are folded in an accordion pattern longitudinal to the interaction point, while the gaps are filled with liquid

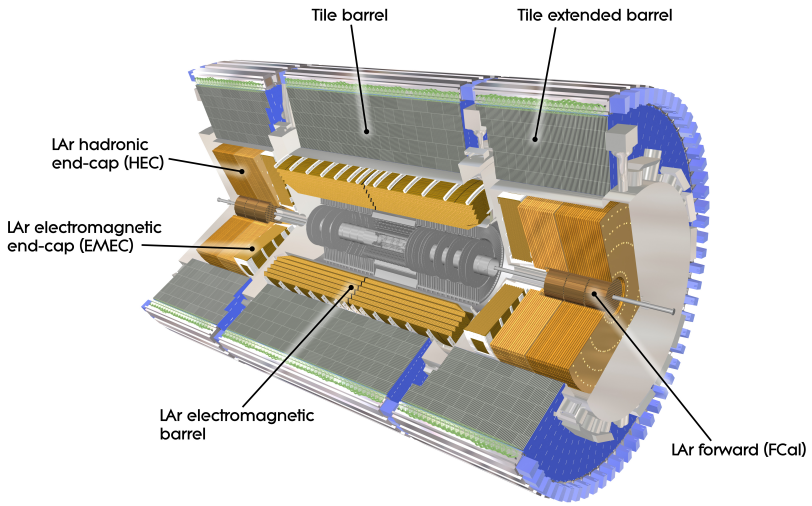

Figure 4.4: Schematic layout of the ATLAS calorimeters. They are built around the inner detector indicated in gray. They are mainly split into two layers, the inner hadronic and outer electromagnetic layer. In addition there is the Forward Calorimeter directly around the beam pipe. [47]

argon. The surfaces are covered with electrodes to apply a voltage of $\approx 2000\,\mathrm{V}$ to the argon. A particle passing through the calorimeter repeatedly transits between lead and argon. In lead, electrons above 10 MeV lose their energy dominantly via bremsstrahlung, photons above 1 MeV do so via pair production [55]. This creates a *shower* of electrons and photons which exponentially decrease in energy because with each interaction their energy is distributed to two particles. The electrons and photons of lower energy in turn strip electrons from the liquid argon, which will then drift towards the surrounding electrodes resulting in a detectable signal.

The showering process is characterized by the radiation length X_0 which is defined as the length after which an electron has been decelerated to $1/e$ of its initial energy which also corresponds to 7/9 of the mean free path of a high energy photon before pair production. In a material with proton number Z, the radiation length approximately follows [56]

$$X_0 \propto \frac{m_e^2}{Z^2}\,, \tag{4.4}$$

which is why lead, which has the highest proton number of all stable elements, was chosen as an absorber. Overall the material of the electromagnetic calorimeter adds up to $\approx 20 X_0$, depending on $|\eta|$, ensuring that most of the electromagnetic showers stay confined inside. Since the energy loss due to bremsstrahlung decreases quadratically with the particle's mass, muons lose only a small amount of their energy in this layer. The energy resolution in the electromagnetic layer was measured to be $\sigma_E/E = 10\%/\sqrt{E\,[\mathrm{GeV}]} \oplus 2\%$, where $\oplus$ indicates summing in quadrature [57].

The majority of the hadrons also leave the electromagnetic layer. Their deceleration is mainly based on inelastic nuclear scattering with an energy transfer to secondary

hadrons. These continue to scatter until they are of sufficiently low energy to be stopped via ionization energy transfer or to be absorbed by a nucleus. This hadronic showering is characterized by the nuclear absorption length λ, which is typically much larger than the radiation length and not strongly dependent on the proton number.

This gives rise to the different design of the hadronic layer of the calorimeter. It consists of several subsystems: the Tile Long Barrel covering $|\eta| < 1.0$, Tile Extended Barrels covering $0.8 < |\eta| < 1.7$, the Hadronic End-Caps covering $1.5 < |\eta| < 3.2$ and the Forward Calorimeters covering $3.1 < |\eta| < 4.9$. The End-Caps and Forward Calorimeters also use liquid argon as active material but in combination with considerably thicker copper and tungsten absorbers totaling in $\approx 10\lambda$ of material to contain highly energetic jets.

The Tile Calorimeter uses steel as absorber in combination with polystyrene scintillators equipped with wavelength-shifting fibers and photomultipliers, providing around 7.4λ of material.

The energy resolution of a hadronic calorimeter is generally far worse than its electromagnetic counterpart, as there are several ways that energy can escape "unseen" [52]. For instance, hadrons can excite nuclei which, depending on their lifetime, can keep the excitation during the readout. If the excitation is only short-lived, the nucleus can undergo fission, of which the heavy decay products usually cannot leave the absorber. In both cases, the energy is not seen by the active material. The excited nucleus can also emit (a) slow neutrons (so-called spallation), which only transfer energy to the active material if it contains nuclei of similar mass (usually in the form of hydrogen), (b) slow protons which ionize the active material much more strongly than the shower particles of higher energy or (c) photons, which create an electromagnetic shower with a possibly different response in the active material.

In addition to these processes of interaction with matter, the statistical composition of the jet can make a difference. Typically, a significant contribution to a jet's energy is carried by pions. The visible energy varies drastically depending on the ratio of π^0, which dominantly decay into two photons, and $\pi^\pm$, which dominantly decay into a muon-neutrino pair leaving the calorimeter without a large energy deposition.

These processes result in the coarser energy resolution for hadrons, which is measured to be $\sigma_E/E = 53\%/\sqrt{E\,[\mathrm{GeV}]} \oplus 6\%$ in the Tile Barrel [58], $\sigma_E/E = 71\%/\sqrt{E\,[\mathrm{GeV}]} \oplus 6\%$ in the Hadronic End-Caps [59] and $\sigma_E/E = 94\%/\sqrt{E\,[\mathrm{GeV}]} \oplus 8\%$ in the Forward Calorimeters [60].

4.2.3 Muon Spectrometer

The muon spectrometer is used to measure muon tracks bent by the large superconducting air-core barrel and end-cap toroid magnets depicted in Figure 4.2. It is designed to precisely track charged particles exiting the calorimeters in a pseudorapidity range of $|\eta| < 2.7$ and to also allow fast triggering in the range $|\eta| < 2.4$.

The muon spectrometer consists of three cylindrical layers in the barrel while the end-caps are made of four large wheels orthogonal to the beam. The precision tracking is mostly done by *Monitored Drift Tubes* filled with an argon/carbon dioxide mixture. These tubes are aligned perpendicular to the r-z-plane (also called bending plane since the bending of the muon's trajectory due to the magnetic field happens in this plane). That

way, they offer a fine resolution of 35 µm in the bending plane, but no distinction in ϕ other than the hit octant. The inner layer of the end-cap's forward region ($2.0 < |\eta| < 2.7$) is equipped with *Cathode-Strip Chambers* instead which can deal with the higher rates in this region. They are realized as multiwire proportional chambers, meaning they consist of a grid of anode wires and cathode wires orthogonal to each other in a chamber also filled with an argon/carbon dioxide mixture. This allows for a similar resolution in the bending plane of 40 µm and a coarse resolution in ϕ-direction of about 5 mm.

Resistive Plate Chambers(RPCs) were selected as detectors for triggering in the barrel region ($|\eta| < 1.05$). They consist of parallel plates at a distance of 2 mm with an applied strong electric field of 4.9 kV/mm. This does not allow for a spatial resolution finer than the plate size but assures a very fast avalanche process on the order of 5 ns which makes this detector suitable for bunch-crossing identification and triggering. In the end-caps, the same purpose is fulfilled by *Thin-Gap Chambers* (TGCs), which are multiwire-proportional chambers. Both the Resistive Plate Chambers and the Thin Gap Chambers also provide resolution in ϕ to complement the Monitored Drift Tubes' lack thereof.

4.2.4 Trigger System

With a collision frequency of 40 MHz and a raw event size in the order of 1 MB, the bandwidth of the ATLAS detector as well as the storage capacities are insufficient to readout every bunch-crossing or to store the results. Hence, the ATLAS detector is equipped with a trigger system which has the essential task to decide on the fly, which bunch-crossing contains an interesting event and is to be read out and saved for future analyses. It received major upgrades during the long shutdown 2013/2014 in order to deal with the anticipated increases in center-of-mass energy and instantaneous luminosity [61]. Since only data recorded in 2015 are studied in this thesis, this chapter describes the current Run-2 system.

The trigger system consists of two stages: the hardware-implemented *Level-1* and the *High Level Trigger* (HLT) running as software in a distributed computing grid.

The Level-1 trigger has the task to reduce the bunch-crossing rate of up to 40 MHz (corresponding to the 25 ns bunch spacing) to a rate of ≈ 100 kHz for the actual readout. This decision has to be taken in less than 2.5 µs for each bunch-crossing because the readout buffers on the detector overflow otherwise. To do so, the *Central Trigger Processor* (CPT) receives input from the two subsystems, the L1 calorimeter trigger (L1Calo) and the L1 muon trigger (L1Muon). No information from the inner detector is used in Level-1 since the reconstruction of tracks from the very fine granularity tracker exceeds the 2.5 µs time budget.

L1Calo relies on reduced-granularity input from the calorimeters. The reduction is achieved by 7168 *Trigger Towers*, which are the analog sums of calorimeter cells in a 0.1×0.1 region in $\eta \times \phi$ in the Barrel up to 0.4×0.4 in the Forward Calorimeters. The *PreProcessor* digitizes this input, calibrates to the transverse energy E_T and assigns pulses to the correct bunch-crossing based on their shape. The identified energy deposits are analyzed by the *Cluster Processor* (CP) and the *Jet/Energy-sum Processor* (JEP) in parallel. The CP searches electron/photon- and τ-lepton-candidates exceeding a programmable energy threshold and, if required, meeting given isolation criteria. JEP

identifies jets and calculates both the missing transverse energy and the global scalar sum of transverse energy. L1Calo also forwards the positions of identified objects as *Regions of Interest* to the HLT, which are then used as a seed for the reconstruction algorithms.

L1Muon searches for coinciding hits in the different layers of the muon trigger chambers (RPCs and TGCs). The deviation of these hits from a straight line is compared to thresholds defined for muon tracks of certain momenta and lead to the identification of a muon if they are not exceeded.

The multiplicity of objects exceeding given thresholds and the global missing transverse energy and its scalar sum provided by L1Calo and L1Muon is finally evaluated by the CPT. It checks whether the conditions of any trigger in the so-called L1 trigger menu is met and if so, accepts this bunch-crossing for the HLT.

The HLT then runs reconstruction algorithms with the full calorimeter granularity, the high precision muon chambers and the tracker information. Most of these algorithms only operate on the Regions of Interest identified by their corresponding L1 seed in order to save computation time. Most triggers stage their decision in a fast first-pass reconstruction which rejects the majority of the events and a slower precision reconstruction performed on the remaining ones. This way the $\approx 100\,\mathrm{kHz}$ acceptance rate of L1 is reduced to a final trigger rate of $\approx 1\,\mathrm{kHz}$ for events to be permanently stored.

5 Object Reconstruction

After an event is read out from the ATLAS detector, it needs to be reconstructed in order to be of use to a physics analysis. This means that signals from the various detector subsystems need to be translated into a set of physical objects (particles with certain momenta) responsible for the observation. This is currently done within the ATLAS software framework ATHENA [62]. Since Monte Carlo samples after the detector simulation provide the same output format as recorded data, these reconstruction algorithms can be applied to both in the same manner, ensuring the best possible consistency.

This chapter gives a brief description of the reconstruction of the physics objects used in this thesis from the ATLAS detector output.

5.1 Jets

As stated in Section 2.1.3, quarks and gluons emerging from a proton-proton collision cannot exist freely due to QCD color confinement. Instead, they form collimated *jets* of color neutral hadrons. Jets considered in this thesis are reconstructed from calorimeter energy deposits using the anti-k_{T} algorithm [63] with the radius parameter (defined in the η-ϕ-plane) set to $R = 0.4$. It sequentially clusters calorimeter cells into larger objects, starting at the highest energies, until given exit criteria based on the radius parameter are met. This is repeated until every energy deposit exceeding a given noise threshold is clustered into a jet.

The resulting jets are then calibrated as detailed in Reference [64] for EM jets. Besides the calorimeter and tracking measurements, muon spectrometer hits are considered to account for constituents of the jet that leave the calorimeter. Energy deposits in the jet area from identified pile-up events are removed [65] and a residual dependence on the number of primary vertices and the average number of interactions per bunch crossing is corrected for. Afterwards, a Monte-Carlo-based correction is applied in order to match the energy measured on detector level to the energy on particle level. The last calibration step is applied only to data such that it matches the Monte Carlo scale. It balances the transverse momentum of observed jets to other recoiling objects of known energy scales. With increasing jet energy, these recoiling partners are photons, leptonically decaying Z bosons and multiple low-energy jets.

This calibration altogether applies sizeable corrections accompanied by systematic uncertainties which are collectively called the *jet energy scale* uncertainty. It depends on p_{T} and falls from 6% at 20 GeV to $\approx 1\,\%$ above 200 GeV. At very large transverse momenta above 1.8 TeV, it rises again to $\approx 3\,\%$ because the balancing against well known objects becomes harder [66].

Although the jet energy scale can be calibrated to meet the average detector response, the coarse energy resolution of the calorimeter leads to a smeared jet energy measurement.

This *jet energy resolution* was found to be $\approx 15\,\%$ for low-energy jets of 30 GeV and to fall to $\approx 5\,\%$ at $> 300\,\text{GeV}$ [67].

In this thesis, only jets not labeled as pile-up objects by the jet vertex tagger [68] are considered. For central low-energy jets with $p_\text{T} < 50\,\text{GeV}$ and $|\eta| < 2.4$, it requires them to have a significant amount of tracks which are compatible with the primary vertex[1] (corresponding to a jet vertex fraction > 0.64).

5.2 Muons

Muon reconstruction relies primarily on tracks in the inner detector and muon spectrometer, while partially being aided by information from the calorimeters. The reconstruction of tracks in the muon spectrometer is based on the *Chain 3* algorithm from Run-1 with several improvements described in Reference [69]. It begins with a Hough transform [70] in the single layers of the precision chambers to identify hits aligned on a trajectory in the bending plane. The coordinates perpendicular to the bending plane are determined by the trigger chambers. These segments from the single layers then seed a fit to the trajectory across all layers.

If the resulting trajectory can be extrapolated to a reconstructed track in the inner detector, it is reconstructed as a *combined* muon by a global fit to both tracks. In the region $|\eta| < 0.1$, the efficiency of the combined reconstruction drops to $\approx 60\,\%$ because necessary structural material of the ATLAS detector limits the amount of muon chambers. Here, *segment-tagged* and *calorimeter-tagged* muons are reconstructed as well. Segment-tagged means that a trajectory reconstructed from the inner detector is compatible with at least one track segment in the precision chambers, calorimeter-tagged only requires it to be compatible with an energy deposit from a minimum-ionizing particle in the calorimeter. These reconstructions increase the efficiency to $\approx 96\,\%$ at the cost of an increased rate of false-positives.

Different qualities are assigned to the muons, depending on additional requirements on the significance of the charge determination, the consistency of the p_T measured by the inner detector and the muon spectrometer, and the χ^2 of the global fit. In this thesis, *loose* and *medium* muons in the central region $|\eta| < 2.5$ are used. Medium quality here only allows combined muons, whereas loose quality also includes segment-tagged and calorimeter-tagged muons at $|\eta| < 0.1$.

The momentum scale uncertainty of combined muons was measured to be $< 0.3\,\%$, depending on $|\eta|$, in J/ψ and Z decays [69]. With the same measurements, a momentum resolution of $< 3\,\%$, also depending on $|\eta|$, was determined.

5.3 Electrons

Electrons are reconstructed using tracks from the inner detector and energy deposits in the calorimeter. Tracks in the inner detector are fitted with two hypotheses modeling the energy loss by interactions with the detector material. If the default pion hypothesis fails

[1] Among all reconstructed vertices in the luminous area, the one with the highest $\sum p_\text{T}^2$ of all associated tracks with a transverse momentum exceeding 400 MeV is selected as primary vertex.

to explain the hits, a second fit under the electron hypothesis allowing for larger energy loss is performed [71]. In the calorimeter, clusters of energy deposition are identified and matched to the electron tracks to create electron candidates. If no track is associated, they are considered as unconverted photon candidates described in the following section. To eliminate jets or converted photons from these candidates, a multivariate identification analysis is performed, using criteria like the shower shape, leakage into the hadronic calorimeter, track condition or information from the transition radiation tracker.

Based on the evaluated likelihood in this identification analysis, a quality is assigned to each electron. This assignment is inclusive, meaning that e.g. all medium electrons are also loose electrons.

Similar to the calibration of jets, electrons are corrected for energy losses, calibrated towards Monte Carlo particle level and, in data, balanced to observed Z decays. In a cross-check with J/Ψ- and Z-decays a remaining scale uncertainty between 1 % and 0.03 % depending on $|\eta|$ and p_{T} was found [72]. The calibration of the mean scale of the calorimeter, however, does not change its resolution. It falls from $\approx 3\,\%$ at $p_{\mathrm{T}} = 10\,\mathrm{GeV}$ to $\approx 1\,\%$ for $p_{\mathrm{T}} > 200\,\mathrm{GeV}$

5.4 Photons

Photon reconstruction in ATLAS [73] is closely linked to the electron reconstruction, since both behave similarly in the electromagnetic calorimeter. Before reaching the calorimeter, a photon traverses the inner detector where it does not leave a track due to its lack of charge. But as the inner detector makes up between 0.4 and 2.4 radiation lengths of material, depending on $|\eta|$ [47], the photon might convert into an electron-positron pair. This creates two classes of photons – *converted* and *unconverted* – that need to be considered in the reconstruction.

As mentioned above, electromagnetic clusters without associated tracks are handled as candidates for unconverted photons. Additionally, vertices from the inner detector consistent with electron-positron pair production become candidates for converted photons after matching their tracks to electromagnetic clusters. These candidates undergo a similar multivariate analysis as the electron candidates. If the criteria are met, the quality loose or tight is assigned based on the evaluated likelihood.

After the calibration, a scale uncertainty for photons of $\approx 0.3\,\%$ remains. Their resolution is identical to that for electrons mentioned above.

5.5 Overlap Removal

With the reconstruction and identification of objects as described above, double-counting is possible. For example, an identified electron might still be counted as a jet or as a calorimeter-tagged muon. To minimize these effects, an overlap removal based on the ATLAS recommendations [74] is performed in this thesis.

Jets in the direct vicinity $\Delta R(\text{jet}, e) < 0.2$[2] of an electron are removed since it is likely that the electron was also clustered as a jet. In the case of $0.2 < \Delta R(\text{jet}, e) < 0.4$, however, the electron is removed. This was chosen, because hadrons present in the jet could decay leptonically. The resulting electron needs to be counted towards the energy of the jet and not as prompt particle from the hard interaction. The overlap removal for muons and jets is performed identically, except that a jet needs to have at least three tracks to be removed.

The last removal is applied between electrons and muons. As a muon leaves a track in the inner detector and some energy in the calorimeter, it might also be identified as an electron. Thus, electrons that share the track with an identified muon are removed.

5.6 Missing Transverse Energy Calculation

As mentioned in Section 2.3, the missing transverse energy is the negative vectorial sum of all final state particles' transverse momenta. The two components are

$$E_x^{\text{miss}} = -\sum_{\text{particles}} p_x \,, \quad E_y^{\text{miss}} = -\sum_{\text{particles}} p_y \,. \tag{5.1}$$

Since different particles receive different energy scale corrections, it is crucial to use the fully calibrated and selected objects in the sum. This is referred to as the *hard term* of $\vec{E}_{\text{T}}^{\text{miss}}$. However, not all tracks and energy deposits are associated to a specific reconstructed object. They make up the *soft term* that needs to be added without being scale corrected. The final missing transverse energy is then given by:

$$\vec{E}_{\text{T}}^{\text{miss}} = \vec{E}_{\text{T}}^{\text{miss,jets}} + \vec{E}_{\text{T}}^{\text{miss},\mu} + \vec{E}_{\text{T}}^{\text{miss},e} + \vec{E}_{\text{T}}^{\text{miss},\gamma} + \vec{E}_{\text{T}}^{\text{miss,soft}} \,. \tag{5.2}$$

The $\vec{E}_{\text{T}}^{\text{miss}}$ calculation in this thesis uses the track-based soft term [75]. Tracks with $p_{\text{T}} > 400\,\text{MeV}$, $|\eta| < 2.5$ and the usual reconstruction quality criteria [76] are selected. Tracks not originating from the primary vertex and those with a momentum uncertainty exceeding 40 % are removed. Additionally, the tracks belonging to already identified objects must be removed in order to not double count them. This is done for tracks with a distance $\Delta R < 0.05$ to any electron or photon cluster, tracks associated to a combined or segment-tagged muon, and tracks already clustered into a jet. The momenta of the remaining tracks are then summed to form $\vec{E}_{\text{T}}^{\text{miss,soft}}$.

The usage of tracks instead of calorimeter energy deposits to calculate the soft terms looses the contribution from neutral particles. But as it requires consistency with the primary vertex, it is less sensitive to pile-up.

The $\vec{E}_{\text{T}}^{\text{miss}}$ calculation is sensitive to mismeasurements of any observed physics objects. Especially highly energetic jets with their large momentum uncertainty impact the transverse momentum balance. In an event without legitimate missing transverse momentum, the underestimation of a jet's momentum results in *fake* $\vec{E}_{\text{T}}^{\text{miss}}$ pointing into the the direction of said jet. An overestimation yields fake $\vec{E}_{\text{T}}^{\text{miss}}$ anti-parallel to the jet,

[2] Following the recommendations, the *rapidity* y instead of the pseudorapidity η is used for the calculation of ΔR in this case. It is defined as $y = \frac{1}{2} \ln \frac{E+p_z}{E-p_z}$ and is identical to the pseudorapidity for massless particles.

respectively. For this reason, many analyses, including the two presented in this thesis, incorporate a minimal angular separation $\Delta\phi$ between $\vec{E}_{\mathrm{T}}^{\mathrm{miss}}$ and any jet.

6 Mono-Jet Search

This chapter describes a search for physics beyond the Standard Model in a mono-jet signature. The analysis strategy closely follows the recently published search of the ATLAS collaboration in 2015 data [34]. The chosen event selection criteria were derived in dedicated studies to achieve an adequate compromise between background reduction and signal efficiency [77].

As mentioned in Section 2.3, the goal of the mono-jet search is to analyze events with large missing transverse energy and a recoiling hard jet. This allows to study partially invisible final states. In this thesis, the results are interpreted in an axial-vector mediator model for WIMP production, the invisible decay of the Standard Model Higgs boson, and the existence of a Higgs-like ZZ resonance.

6.1 Monte Carlo Simulations

The dominant Standard Model contribution to the mono-jet signature is the production of a Z boson in association with at least one jet, where the Z boson decays to neutrinos. An exemplary Feynman diagram is provided in Figure 6.1(a). Additionally, the gluon and outgoing quark can be exchanged to yield the contribution of initial state radiation from an incoming quark. This diagram is indistinguishable from the expected signal, making $Z \to \nu\nu$ an *irreducible* background.

The next-largest background is the production of a W boson decaying into a $\tau^+\nu_\tau$ pair (or equivalently a $\tau^-\bar{\nu}_\tau$ pair) with a Feynman diagram as depicted in Figure 6.1(b). It is a *reducible* background because it can, in principle, be distinguished from the signal process. However, this is difficult as the τ lepton has a short lifetime of about 290 fs [55] and usually decays before reaching the tracker. With a branching ratio of 60% it decays dominantly into a neutrino and pions, which leave a detector signature similar to

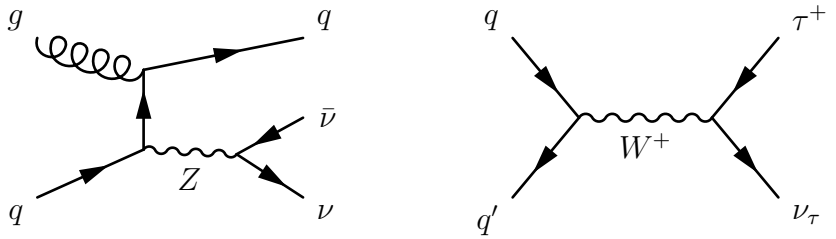

(a) $Z \to \nu\nu$ background **(b)** $W \to \tau\nu$ background

Figure 6.1: Tree-level Feynman diagrams for the dominant Standard Model backgrounds in the mono-jet topology. **(a)** $Z \to \nu\nu$ process in association with a jet. The gluon and outgoing quark can also be exchanged to form $q\bar{q}$ annihilation with initial state radiation. **(b)** $W \to \tau\nu$ process. It contributes if the τ decays hadronically.

process	generator	PDF
$Z \to \nu\nu$	SHERPA2.2.1	NNPDF3.0 NNLO
$Z \to \mu\mu$	SHERPA2.2.1	NNPDF3.0 NNLO
$W \to \ell\nu$	SHERPA2.2.1	NNPDF3.0 NNLO
diboson	SHERPA2.2.1	NNPDF3.0 NNLO
$t\bar{t}$	POWHEG + PYTHIA6 + EVTGEN	CT10
single top	POWHEG + PYTHIA6 + EVTGEN	CT10
$A \to \chi\bar{\chi}$	POWHEG + PYTHIA8 + EVTGEN	NNPDF2.3 LO
$h \to$ inv	POWHEG + PYTHIA8 + EVTGEN	NNPDF3.0 NNLO
$H \to ZZ$	POWHEG + PYTHIA8	CT10

Table 6.1: Generators and PDFs of the samples used in the mono-jet study. Descriptions of the listed generators are given in References [80–84] and of the PDFs in References [85, 86]. SHERPA includes the calculation of the hard scatter as well as a simulation of parton showers and fragmentation. POWHEG is interfaced to PYTHIA and EVTGEN to perform these tasks.

a highly energetic jet [78].

Additional considered backgrounds are $W \to e\nu$, $W \to \mu\nu$ and $Z \to \mu\mu$ in association with jets, diboson production as well as $t\bar{t}$ and single top contributions. All backgrounds in this analysis are estimated purely from Monte Carlo simulations. They are interfaced to GEANT4 [79] which simulates the complete response of the ATLAS detector to stable final state particles. This allows the identical treatment of simulated samples and recorded data in the reconstruction algorithms. A list of the generators and assumed parton distribution functions (PDFs) for all included processes is provided in Table 6.1.

The signal models are evaluated by additional Monte Carlo samples. To mimic the invisible decay of the Standard Model Higgs boson, samples of gluon-gluon and vector-boson fusion produced Higgs bosons decaying into a pair of Z bosons, which subsequently decay into neutrinos, are used. These are scaled to the full Higgs production cross section of 28.3 pb for gluon-gluon fusion and 3.74 pb for vector-boson fusion as if the Higgs boson would decay only invisible [25]. In Chapter 8, an upper limit on the invisible branching ratio is set.

For the study of Higgs-like ZZ-resonances, samples of narrow-width [87] Higgs-like scalars decaying into a pair of Z bosons are used. Gluon-gluon fusion production and vector-boson fusion production are treated separately as the coupling of this new scalar to quarks and bosons is unknown. The ZZ pair is allowed to decay into two quarks and two neutrinos producing the $E_{\mathrm{T}}^{\mathrm{miss}}$ plus hard jet signature. Additionally, both Z bosons could decay into neutrinos with initial state radiation causing a jet. As only insufficient samples for a heavy scalar decaying this way were available at the time of the study, samples with the ZZ pair decaying into two charged leptons and two neutrinos are used. Since the study is performed on particle level, the charged leptons from the Z decay can easily be identified and treated as if invisible. No correction to the sample normalization

is necessary due to approximately equal branching ratios:

$$\begin{aligned} \mathrm{BR}(ZZ \to \ell\ell\nu\nu) &= 2 \cdot \mathrm{BR}(Z \to \ell\ell) \cdot \mathrm{BR}(Z \to \nu\nu) \\ &\approx \mathrm{BR}(Z \to \nu\nu) \cdot \mathrm{BR}(Z \to \nu\nu) = \mathrm{BR}(ZZ \to \nu\nu\nu\nu)\,. \end{aligned} \tag{6.1}$$

The WIMP production via an axial-vector mediator is studied for a set of different WIMP and mediator masses m_χ and m_A, each with a separate Monte Carlo sample. The assumed couplings of the mediator to quarks (WIMPs) is $g_q = 0.25$ ($g_\chi = 1.0$). These benchmark values are recommended by the ATLAS/CMS Dark Matter Forum as benchmark for searches [88], motivated by an upper limit on g_q by di-jet searches. These couplings only affect the overall normalization of the production and do not influence the expected differential distributions. The results for different couplings can thus easily obtained by scaling the distributions obtained in this chapter according to Equation 2.18.

Pile-up effects are considered in Monte Carlo simulations by overlaying the simulated hard scatter event with other soft interactions based on an assumed profile of the instantaneous luminosity [89]. As this profile does not necessarily match the achieved luminosity in the recorded data, a reweighting is applied in this thesis [90]. Both in recorded data and simulated samples, the distribution of the number of interactions per bunch-crossing is recorded prior to any event selection criteria. This allows to apply a weight to every Monte Carlo event, such that the same distribution can be achieved while keeping the correct normalization.

In addition to the pile-up weights, each Monte Carlo event is associated with an intrinsic weight. These arise because the events are not necessarily generated following the physical kinematic distributions. Instead, they are drawn from predefined probability densities (e.g. flat in momentum) and afterwards reweighted to yield the correct distributions and phase space integral. This can serve a computationally more efficient generation as well as decreased statistical uncertainties in selected kinematic regions.

6.2 Object Selection

On top of the common reconstruction and selection criteria mentioned in Chapter 5, this mono-jet analysis introduces additional requirements for the reconstructed objects. This so-called *baseline* selection is used in the overlap removal and missing transverse energy calculation described in Sections 5.5 and 5.6.

For jets, $p_\mathrm{T} > 20\,\mathrm{GeV}$ and $|\eta| < 2.8$ are required. Muons are considered if they satisfy the loose quality criteria, $p_\mathrm{T} > 10\,\mathrm{GeV}$ and $|\eta| < 2.5$. Electrons are also selected with loose quality, and are required to have $p_\mathrm{T} > 20\,\mathrm{GeV}$ and $|\eta| < 2.47$. Photons with tight quality and $p_\mathrm{T} > 20\,\mathrm{GeV}$ are considered.

6.3 Event Selection

The events initially considered in this analysis were selected by the `HLT_xe70` trigger chain which requires $E_\mathrm{T}^\mathrm{miss}$ of at least 70 GeV in the final reconstruction of the HLT. The additional selection criteria are summarized in Table 6.2.

Events are required to have $E_{\mathrm{T}}^{\mathrm{miss}} > 250\,\mathrm{GeV}$, making sure that the trigger works fully efficient in the signal region. The jet with the highest p_{T}, called the *leading* jet, is required to have $p_{\mathrm{T}} > 250\,\mathrm{GeV}$ and $|\eta| < 2.4$. This choice reflects the anticipated symmetric behavior of the invisible final state particles and the recoiling jet. Events with more than three additional jets with $p_{\mathrm{T}} > 30\,\mathrm{GeV}$ are rejected as no large jet multiplicity is expected in the signal. The angular separation between the transverse missing energy and the transverse momenta of all selected jets must exceed $\Delta\Phi > 0.4$. This reduces the probability of fake $E_{\mathrm{T}}^{\mathrm{miss}}$ arising from the jet mismeasurements as mentioned in Section 5.6. Only the case of parallel jet and $\vec{E}_{\mathrm{T}}^{\mathrm{miss}}$ can be rejected, as the antiparallel case resembles the signal. This is however still sufficient to suppress the majority of the multi-jet background events. As no leptonic activity is expected in the signal, all events with electrons or muons satisfying the respective selection criteria are rejected. This reduces the background contribution from leptonically decaying W or Z bosons in association with jets.

Additional quality criteria on the jets are required in order to reduce background not originating from proton-proton collisions. These are beam induced background[1], muon showers from cosmic rays and noisy calorimeter cells. They typically create artificial jets in the reconstruction. The so-called *jet cleaning* suppresses these backgrounds by identifying non-collision jets based on the pulse shape in the calorimeters, the distribution of energy across the calorimeter layers and the fraction of charged particles in the jet. The event is rejected, if any of the selected baseline jets does not satisfy the loose quality requirement or if the leading jet does not satisfy the tight quality. The existence of a reconstructed primary vertex with at least three associated tracks of $p_{\mathrm{T}} > 400\,\mathrm{MeV}$ is required as well.

In addition to these physical requirements, a technical cut on Monte Carlo event weights is applied. These can, depending on the simulated process, cover a wide range of values such that a single event with a very large positive or negative weight can seriously deteriorate the statistical significance of a bin. To avoid this, the distribution of event weights in each sample was tracked and events with a weight deviating from the distribution's mean by more than 100 times the root mean square are discarded in all following evaluations. Only a negligible effect on the overall sample normalization is observed. The results of such a cut on the weights is presented in Figure A.1.

The definition of the particle level signal region closely follows that on reconstruction level described above in order to minimize the necessary extrapolation by the Monte Carlo simulation into unprobed phase space. All requirements listed in Table 6.2 are applied identically. For the object definition, the same criteria on p_{T} and η are used, but no quality requirements are necessary as these are simulated instead of reconstructed objects. The selection of jets is defined by the anti-k_{T} algorithm with radius parameter $R = 0.4$ applied to the final state particles after hadronization. Jets are removed if an electron or muon not originating from a decaying hadron exists within a $R = 0.4$ radius. The criteria suppressing the non-collision background are not applied.

[1] Protons can get lost from the beam prior to the interaction point. These cause cascades of, among others, muons which may reach the detector. These are referred to as beam induced background.

$E_{\mathrm{T}}^{\mathrm{miss}}$	$> 250\,\mathrm{GeV}$
leading jet p_{T}	$> 250\,\mathrm{GeV}$
leading jet η	< 2.4
number of jets with $p_{\mathrm{T}} > 30\,\mathrm{GeV}$	$\in \{1, 2, 3, 4\}$
$\Delta\phi\big(\vec{E}_{\mathrm{T}}^{\mathrm{miss}}, \mathrm{jets}\big)$	> 0.4
number of $e^{\pm}$ with $p_{\mathrm{T}} > 20\,\mathrm{GeV}$	$= 0$
number of $\mu^{\pm}$ with $p_{\mathrm{T}} > 10\,\mathrm{GeV}$	$= 0$

Table 6.2: Event Selection for the mono-jet signal region. The listed criteria are applied both on particle and reconstruction level, while for the latter reconstructed objects as described in Section 6.2 are used. Additional criteria to remove non-collision background are applied on reconstruction level.

6.4 Uncertainties

Both the observed and simulated distributions are subject to statistical uncertainties in each bin. In data, the observed numbers of events follow Poissonian distributions with an associated uncertainty of $\sigma \approx \sqrt{n_{\mathrm{obs}}}$. In Monte Carlo simulations, however, not all events contribute equally to the final event count due to their individual weights depending on the present momenta and the pile-up. Additionally, the resulting distributions are scaled to match the recorded luminosity $L_{\mathrm{int}} = 3.2\,\mathrm{fb}^{-1}$. This is done based on the highest order cross section calculation available for the process in a given sample. Thus, the final event count in a given bin does not necessarily follow a Poissonian anymore. In this thesis, a Gaussian shape is assumed and the width is estimated using the bootstrapping method described in Section 3.5. Typically, these statistical Monte Carlo uncertainties are small compared to those in data because more simulated events are available in the selected phase space.

6.4.1 Systematic Experimental Uncertainties

Systematic uncertainties on energy scales and resolution are applied on the Monte Carlo background estimate. They are evaluated by altering their respective values in the calibration procedure and repeating the analysis. Uncertainties on the reconstruction and identification efficiency of electrons (muons) are accounted for by increasing or decreasing the weights of events with identified electrons (muons). As all events with electrons or muons satisfying the selection criteria are rejected in this mono-jet analysis, these systematic variations have no impact.

All of these uncertainties have multiple sources which can be varied separately by a corresponding nuisance parameter. To save computational effort, the ATLAS calibration groups provide so-called reduced models where several nuisance parameters are

jet energy scale	JET_GroupedNP_1 JET_GroupedNP_2 JET_GroupedNP_3
jet energy resolution	JET_JER_SINGLE_NP
$\vec{E}_{\mathrm{T}}^{\mathrm{miss}}$ soft term scale	MET_SoftTrk_Scale
$\vec{E}_{\mathrm{T}}^{\mathrm{miss}}$ soft term resolution	MET_SoftTrk_ResoPara MET_SoftTrk_ResoPerp
electron/photon energy scale	EG_SCALE_ALL
electron/photon energy resolution	EG_RESOLUTION_ALL
electron reconstruction efficiency	EL_EFF_Reco_TOTAL
electron identification efficiency	EL_EFF_ID_TOTAL
muon energy scale	MUON_SCALE
muon energy resolution	MUON_ID MUON_MS
muon efficiency	MUON_EFF_STAT MUON_EFF_SYS MUON_EFF_STAT_LOWPT MUON_EFF_SYS_LOWPT

Table 6.3: Considered experimental systematic variations and their corresponding nuisance parameters. Most of them can be set to their nominal and $\pm 1\sigma$ values in the calibration stage. For the jet energy resolution and the two $\vec{E}_{\mathrm{T}}^{\mathrm{miss}}$ soft term resolution parameters, only nominal and $+1\sigma$ are available. The -1σ effect is approximated by the negative of the $+1\sigma$ deviation in these cases.

combined into one by quadratically summing their effect. This affects correlations of the objects, e.g. across p_{T} and η. To minimize this, a singular value decomposition of these correlation matrices is performed and only the least important parameters with the smallest eigenvalues are combined [91]. Typically, several steps of reduction with increasing information loss are provided. For e.g. the jet energy scale, the full set consists of 71 parameters, the reduced one of 18 and the minimal one of 3. As the analyses presented in this thesis serve a search instead of a precision measurement, the minimal sets are used in the following.

All considered experimental uncertainties, together with their corresponding nuisance parameters, are listed in Table 6.3. Their effect is evaluated by repeating the analysis for each of them with a value of $\pm 1\sigma$ respective to their nominal value. The result are two replicas of a given distribution on reconstruction level for each nuisance parameter such that, in combination with the nominal distribution, its influence on the event count $n_{\mathrm{mc}}(R_i)$ in a given bin R_i can be evaluated. Asymmetric results are kept at this point, but are symmetrized for the derivation of limits in Chapter 8.

process	sim. events	cross section deviation	
		$\mu_R = \frac{0.5\mu_0}{2\mu_0}$	$\mu_F = \frac{0.5\mu_0}{2\mu_0}$
$Z \to \nu\nu + \text{jet}$	1 000 000	$^{+7.7\,\%}_{-6.8\,\%}$	$^{+3.5\,\%}_{-2.4\,\%}$
$A \to \chi c\bar{h}i + \text{jet}$	200 000	$^{+4.6\,\%}_{-4.5\,\%}$	$^{+1.7\,\%}_{-1.3\,\%}$
h	4 000 000	$^{+19.8\,\%}_{-15.3\,\%}$	$^{-2.9\,\%}_{+2.3\,\%}$
$h \to ZZ \to b\bar{b}\mu\mu$	1 000 000	$^{+24.9\,\%}_{-18.2\,\%}$	$^{+5.4\,\%}_{-4.8\,\%}$

Table 6.4: Total cross section uncertainties based on QCD scale choices as evaluated by the MCFM 8.0 tool.

6.4.2 Systematic Theoretical Uncertainties

In addition to these bin-wise experimental systematic uncertainties, theoretical cross section uncertainties on the Standard Model background and signal processes are considered. They originate mainly from the choice of QCD scales – specifically, the renormalization scale μ_R defining the evaluation of α_S [92] and the factorization scale μ_F separating the hard, perturbative QCD from the soft, non-perturbative QCD [9]. In the generation of Monte Carlo samples, these scales are set to typical energies μ_0 present in the respective process. As this choice is not unique, their variations need to be evaluated. In the following, that is done with the MCFM8.0 tool which allows parton level cross section calculation for given scales [93–95]. The calculations are done at next-to-leading order with both scales at μ_0 and separately for each of them varied by a factor of 0.5 or 2. The number of simulated events per integration step is chosen sufficiently large, depending on the process, in order to reach a stable result. The results are summarized in Table 6.4. All calculations are based on the CT14 NNLO PDF [96].

The effect of the QCD scale choices on the complete Standard Model background is approximated by the effect on the dominant $Z \to \nu\nu + \text{jet}$ contribution. The uncertainty on the the production of WIMPs via an axial-vector mediator in association with a jet is evaluated at $m_A = 1\,\text{TeV}$ and $m_\chi = 100\,\text{GeV}$ and assumed for all mass points. For these two processes, also a minimal missing transverse energy of 250 GeV, as in the event selection described in Section 6.3, is required. The uncertainty on the Standard Model Higgs production via gluon-gluon fusion and vector-boson fusion are assumed for the Higgs to invisible model as no dependence on the QCD scales in the invisible final state is expected. For the uncertainty on the heavy Higgs-like ZZ-resonance, the production of a Standard Model Higgs decaying into two Z bosons, of which one decays hadronically, is evaluated. In the two latter cases, no requirement on the missing transverse energy can be placed as the simulated processes do not involve any invisible particles. The effect of the variation of the renormalization scale is found to be larger in these cases because the production of a Higgs boson via gluon-gluon fusion scales $\propto \alpha_S^2$ at lowest order and involves large corrections from higher orders [25].

Uncertainties from the PDF are neglected in this thesis.

6.5 Results on Reconstruction Level

In the data set recorded in 2015 corresponding to an integrated luminosity of $3.2\,\text{fb}^{-1}$, 20 722 events were observed, which fulfill the selection criteria described in the previous section. Their distribution in several kinematic variables in comparison to the Standard Model prediction of in total 19 642 events is presented in Figure 6.2.

In most cases, no significant difference with respect to the given uncertainties is observed. However, the distribution of the leading jet η shows, that the Monte Carlo prediction systematically underestimates events with large pseudorapidity. This mismodeling is also present in the jet-multiplicity, where the slope is underestimated by the simulation. The depicted uncertainties in this distribution are dominated by the $\approx 8\,\%$ QCD scale uncertainty that is fully correlated across bins. Consequently, the deviation in each individual bin is consistent with the uncertainty, but a tension across bins remains.

In the $E_{\text{T}}^{\text{miss}}$ distribution, which is the only one considered in the following derivation of limits, the effect is not as pronounced. The underestimation of in total 5.2 % can be mostly covered by the fully correlated systematic uncertainties since no major shape deviation is observed. As ultimately only relative differences between single and combined signatures are of interest in the scope of this thesis, any remaining mismatch is tolerable.

For the statistical analysis, the $E_{\text{T}}^{\text{miss}}$ distribution split into seven bins is used as the discriminant, following Reference [34]. Table 6.5 lists the event yield in each of these bins as well as its composition from the different Standard Model processes. The same results are also shown in Figure 6.7(a). The stated uncertainties on the prediction include the statistical and systematic component, the effect of each variation is presented in Table A.1. They are dominated by the cross section uncertainties from the renormalization scale ($\approx 7\,\%$) and factorization scale ($\approx 3\,\%$). The largest components among the experimental uncertainties are those on jet energy scale and resolution ($\leq 5\,\%$) and the $E_{\text{T}}^{\text{miss}}$ soft term ($< 1\,\%$). The statistical uncertainty ($\leq 1\,\%$) is small compared to the systematic effects.

The analysis of the results with respect to different signal models is performed on particle level after the unfolding step described in the following section.

6.6 Unfolding

The binning on reconstruction and particle level is chosen identical, such that the aforementioned seven $E_{\text{T}}^{\text{miss}}$ intervals correspond to both R_i and T_j ($i, j = 1, \ldots, 7$). With this choice of coarse binning, the migrations between bins become relatively small as the $E_{\text{T}}^{\text{miss}}$ resolution is smaller than or comparable to the bin width. This can be seen from the migration matrix A_{ij} and the folding probability P_{ij} in Figure 6.3. They are close to diagonal with migrations between adjacent bins of 7–22 % and of $< 1\,\%$ across distances of more than one bin. This means, that the unfolding procedure mainly needs to apply a bin-wise correction factor for fakes and misses and the actual deconvolution only plays a subordinate role. The difference between different unfolding methods is thus expected to be small. This is confirmed by unfolding the $E_{\text{T}}^{\text{miss}}$ distribution with the iterative Bayesian and IDS method for different numbers of iterations. Figure 6.4 shows the unfolded result of the Bayesian algorithm depending on the number of iterations. For a reasonably low number of iterations ≤ 4 no significant deviations arise from the

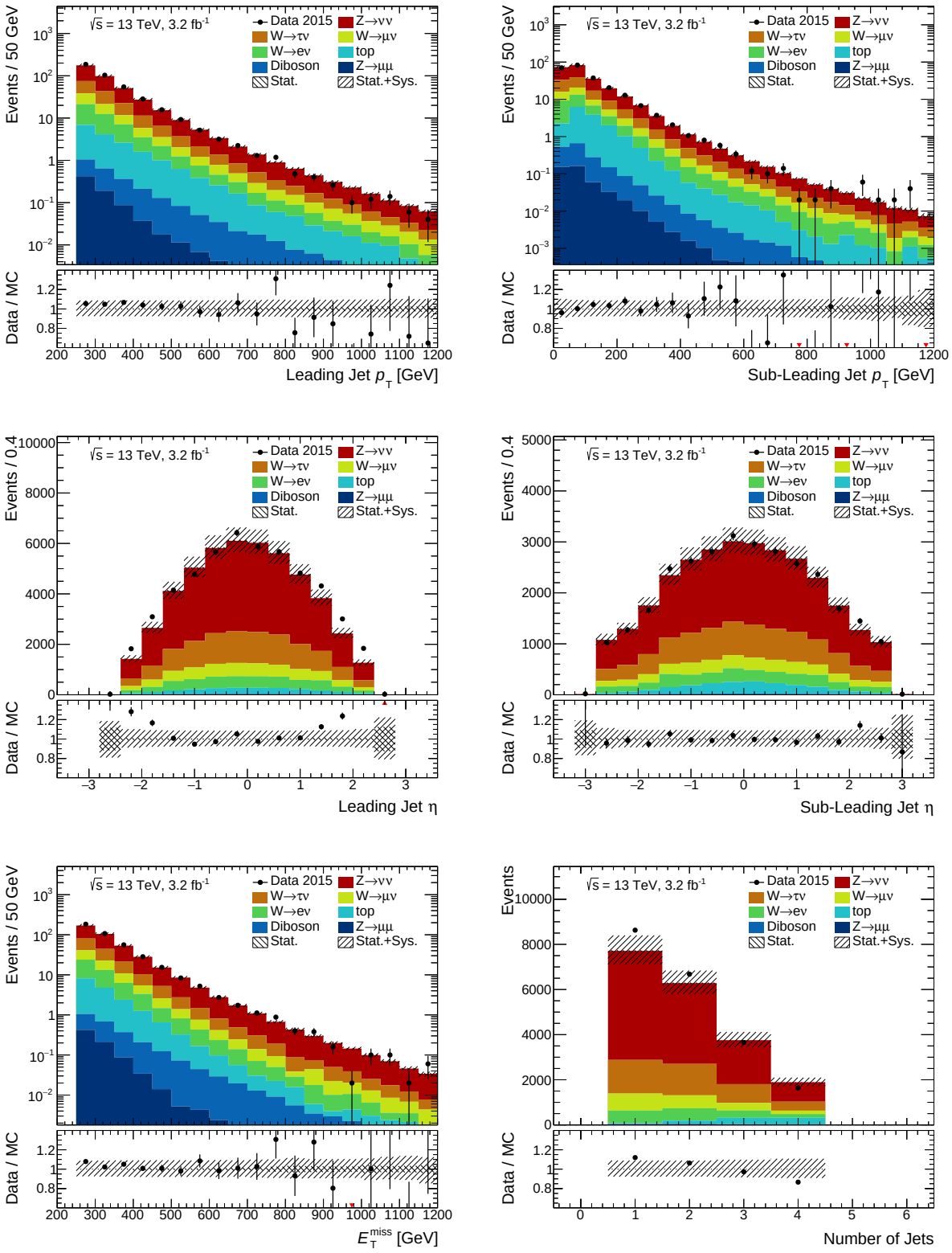

Figure 6.2: Observed distributions of the leading jet's p_{T} and η, $E_{\mathrm{T}}^{\mathrm{miss}}$ and, if it exists, the sub-leading jet's p_{T} and η in comparison to the Standard Model prediction. The jet multiplicity refers to the set of jets with $p_{\mathrm{T}} > 30\,\mathrm{GeV}$. The uncertainty on the Standard Model prediction is the quadratic sum of the statistical component, the systematic experimental variations and QCD scale uncertainties. The latter dominates the indicated systematic uncertainties.

$E_{\mathrm{T}}^{\mathrm{miss}}$ [GeV]	250–300	300–350	350–400	400–500
observed events	9184	5359	2803	2185
SM prediction	$8514\,^{+759}_{-648}$	$5241\,^{+486}_{-427}$	$2668\,^{+256}_{-217}$	$2168\,^{+204}_{-184}$
$Z \to \nu\nu$	$4478\,^{+396}_{-338}$	$3023\,^{+283}_{-250}$	$1607\,^{+158}_{-133}$	$1383\,^{+131}_{-117}$
$W \to \tau\nu$	$1987\,^{+181}_{-154}$	$1073\,^{+99}_{-86}$	$516\,^{+48}_{-42}$	$382\,^{+36}_{-32}$
$W \to \mu\nu$	$854\,^{+79}_{-68}$	$485\,^{+48}_{-44}$	$232\,^{+25}_{-21}$	$161\,^{+17}_{-16}$
$W \to e\nu$	$786\,^{+75}_{-66}$	$422\,^{+43}_{-37}$	$194\,^{+18}_{-17}$	$146\,^{+21}_{-21}$
top	$356\,^{+35}_{-32}$	$204\,^{+19}_{-17}$	$101\,^{+11}_{-\ 9}$	$79\,^{+8}_{-8}$
diboson	$32\,^{+3}_{-2}$	$24\,^{+2}_{-2}$	$14\,^{+1}_{-1}$	$14\,^{+1}_{-1}$
$Z \to \mu\mu$	$21\,^{+2}_{-2}$	$11\,^{+1}_{-1}$	$4.3\,^{+0.8}_{-0.7}$	$2.4\,^{+0.3}_{-0.4}$

$E_{\mathrm{T}}^{\mathrm{miss}}$ [GeV]	500–600	600–700	> 700
observed events	679	223	167
SM prediction	$667\,^{+64}_{-57}$	$225\,^{+22}_{-18}$	$159\,^{+16}_{-14}$
$Z \to \nu\nu$	$454\,^{+44}_{-39}$	$160\,^{+15}_{-13}$	$117\,^{+12}_{-11}$
$W \to \tau\nu$	$105\,^{+10}_{-9}$	$32\,^{+3}_{-3}$	$22\,^{+2}_{-2}$
$W \to \mu\nu$	$45\,^{+5}_{-4}$	$14\,^{+2}_{-2}$	$9.7\,^{+1.2}_{-1.0}$
$W \to e\nu$	$38\,^{+5}_{-6}$	$11\,^{+1}_{-1}$	$5.8\,^{+0.8}_{-0.7}$
top	$19\,^{+2}_{-2}$	$5.2\,^{+0.7}_{-0.7}$	$2.6\,^{+0.5}_{-0.4}$
diboson	$5.4\,^{+0.5}_{-0.4}$	$2.3\,^{+0.2}_{-0.2}$	$1.9\,^{+0.2}_{-0.2}$
$Z \to \mu\mu$	$0.5\,^{+0.1}_{-0.1}$	$0.2\,^{+0.0}_{-0.0}$	$0.1\,^{+0.0}_{-0.0}$

Table 6.5: Observed numbers of events in the seven $E_{\mathrm{T}}^{\mathrm{miss}}$ bins compared to the Standard Model prediction. The stated uncertainties per process are the quadratic sum of the statistical, systematic experimental and QCD scale uncertainties. These do not add up quadratically to the uncertainty of the total prediction because experimental and QCD scale uncertainties are correlated across processes. No uncertainty on the observed events is quoted, but they can be assumed to follow a Poissonian around the Standard Model prediction.

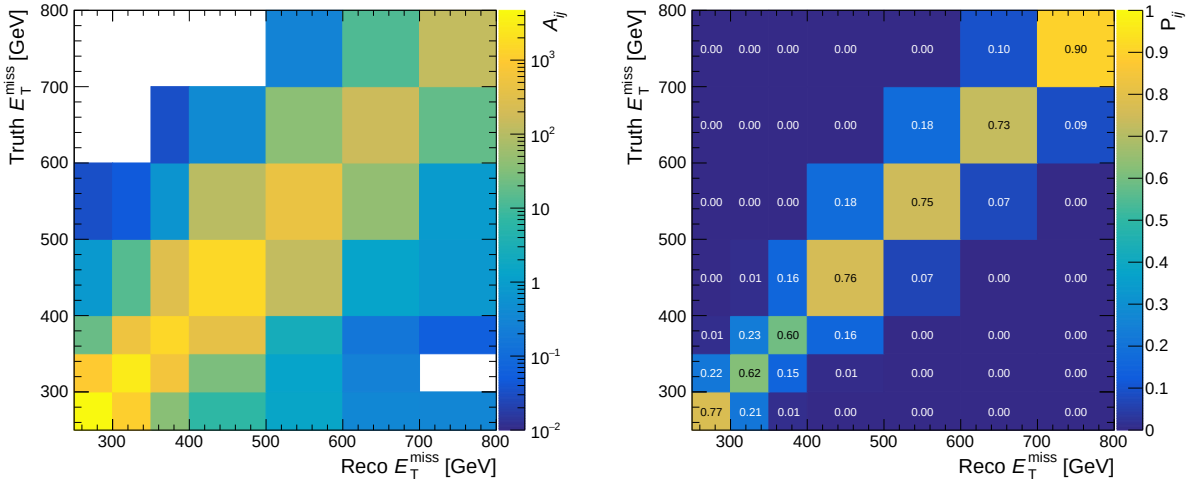

Figure 6.3: (a) Migration matrix A_{ij} of the mono-jet signal region. **(b)** A_{ij} normalized to unity along the x-axis. This corresponds to the folding probability P_{ij} from Equation 3.1 without missed events.

exact choice. But it also visualizes the problem described in Section 3.3: with increasing number of iterations fluctuations begin to grow, increasing the statistical uncertainties and introducing the need for some kind of regularization.

A comparison to the IDS unfolding method is given in Figure 6.5 which shows the χ^2_{red} between the Bayesian and IDS unfolded result obtained for given numbers of iterations. In order not to hide the growing absolute deviations by the simultaneously growing uncertainties, the quadratic difference is given in units of the statistical uncertainty of the Bayesian unfolded result in the first iteration:

$$\chi^2_{\text{red}} \equiv \frac{1}{N_T} \sum_{j}^{N_T} \frac{\left(n_{\text{unf}}^{\text{Bayes}}(T_j) - n_{\text{unf}}^{\text{IDS}}(T_j)\right)^2}{\sigma_{\text{unf}}^{\text{Bayes, 1 it}}(T_j)^2} \,. \tag{6.2}$$

Comparing the first iteration of the Bayesian and IDS unfolded results yields $\chi^2_{\text{red}} = 0$. This is due to the choice of $\lambda_U = 0$ in the first unfolding step which recovers the Bayesian algorithm. Only the refinement of this result is handled differently between the two methods. The unregularized updating of the prior in the Bayesian algorithm introduces the monotonically increasing χ^2_{red} with respect to its first iteration (very left column in the diagram). The regularized nature of IDS unfolding, on the other hand, exhibits a stable result after 4 iterations which approximately corresponds to the Bayesian result after 3 iterations.

This motivates the choice of the IDS unfolding method with 4 iterations (meaning the initial first Bayesian step plus 3 regularized updates) for all following considerations. In a real search for new physics, the exact choice of the method and regularization would require pseudo-data studies and signal injections in order to check for introduced bias and sensitivity to unknown structures. These additional steps are omitted in this thesis as ultimately only relative differences between individual signatures and the combination are studied.

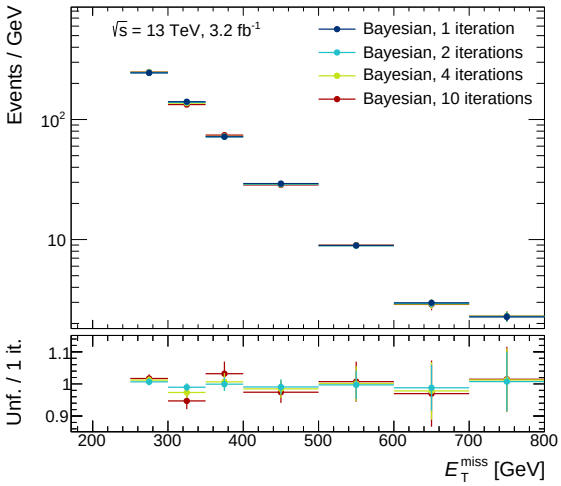

Figure 6.4: Observed $E_{\mathrm{T}}^{\mathrm{miss}}$ distribution unfolded to particle level with the Bayesian algorithm for different numbers of iterations. Indicated is only the statistical component of the uncertainty, as that is the only one approximately uncorrelated across bins. Systematic variations mostly scale the entire distribution up or down.

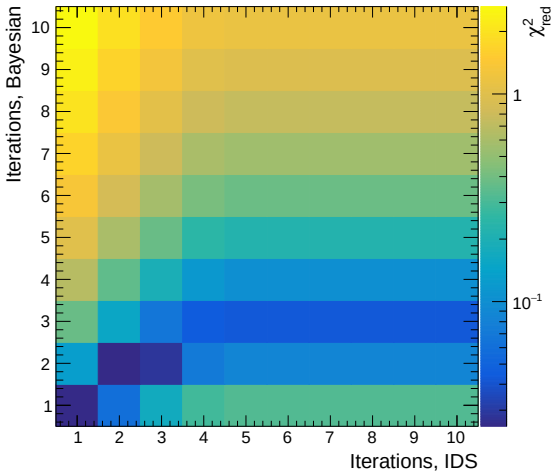

Figure 6.5: χ^2_{red} as defined in Equation 6.2 between the $E_{\mathrm{T}}^{\mathrm{miss}}$ distribution unfolded via the Bayesian and IDS algorithm for different numbers of iterations. The stabilizing nature of IDS is visible as an approximately constant result after 4–5 iterations.

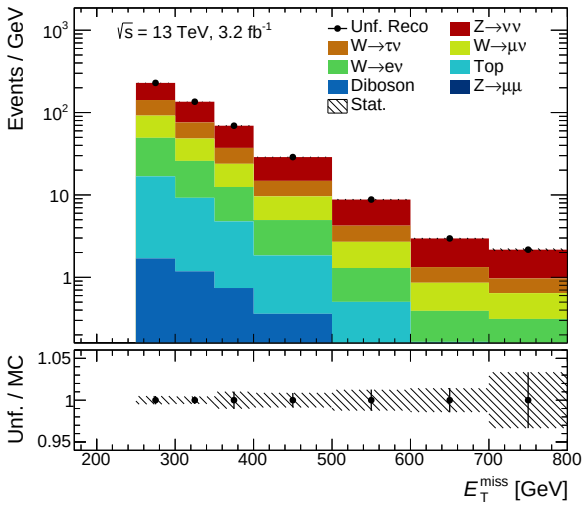

Figure 6.6: Closure test of the unfolding algorithm. Presented is the Monte Carlo particle level distribution in comparison the reconstruction level distribution unfolded with one Bayesian iteration. No deviation is observed, validating the closure of the implemented algorithm.

The overall validity of the implemented unfolding algorithm is checked with the so-called closure test. Applying a single step of Bayesian unfolding on a reconstruction-level Monte Carlo distribution is supposed to yield exactly the underlying particle-level distribution. This can be seen by inserting $n_{\mathrm{mc}}(R_i)$ instead of $n_{\mathrm{data}}(R_i)$ into Equation 3.10:

$$n_{\mathrm{unf}}\big(T_j\big) = \frac{n_{\mathrm{mc}}\big(T_j\big)}{\sum_{i=1}^{N_R} A_{ij}} \sum_{i=1}^{N_R} \left(\frac{A_{ij}}{n_{\mathrm{mc}}(R_i)}\, n_{\mathrm{mc}}(R_i) \right) = n_{\mathrm{mc}}\big(T_j\big)\,. \tag{6.3}$$

Failing to retrieve the exact particle level distribution after such an unfolding step therefore hints at a faulty implementation. The result of a closure test for the $E_{\mathrm{T}}^{\mathrm{miss}}$ distribution is presented in Figure 6.6 where no deviation is observed as expected[2].

As shown above, the first iteration of the IDS unfolding yields the same results as the first Bayesian, such that closure is also observed for the IDS method. In fact, closure is observed in both methods for any number of iterations as the prior does not need to be updated. In the Bayesian algorithm, $\mathrm{P}^{(r+1)}\big(T_j\big)$ will always be identical to $\mathrm{P}^{(r)}\big(T_j\big)$ if the unfolded result is equal to the Monte Carlo truth distribution (Equation 3.14). The IDS method also stops when $\Delta(R_i) = 0$ is reached (Equation 3.17).

This closure test also confirms the handling of the statistical uncertainties throughout the unfolding procedure via the bootstrapping method, as the initial uncertainties on the particle-level distribution are exactly recovered for the unfolded result.

So far, only the handling of the statistical uncertainties was covered, but the experimental uncertainties affecting the reconstruction-level Monte Carlo prediction need to be propagated to the unfolded result as well. For each systematic uncertainty, this is done by separately unfolding the fixed observed distribution under assumption of the varied Monte Carlo migration matrix and the varied reconstruction level distribution. The particle level distribution $n_{\mathrm{mc}}\big(T_j\big)$ is not affected by the systematic uncertainties on detector parameters.

The QCD scale choices are not added to the unfolded result in order to keep the experimental and theoretical uncertainties separated between the observations and predictions. Instead, they are applied to the particle-level Monte Carlo distributions in the comparison to the unfolded results.

With these choices, the IDS unfolded $E_{\mathrm{T}}^{\mathrm{miss}}$ distribution of the mono-jet signal region after four iterations is presented in Table 6.6 and visualized in Figure 6.7(b). The composition of the uncertainties is provided in Table A.2. To be able to use these results in a search for new physics, the correlations of the statistical uncertainties between bins introduced by the deconvolution needs to be provided as well. Due to the aforementioned approximately diagonal response, these become relatively small in this case (between $-5\,\%$ and $15\,\%$). The full correlation matrix is provided in Figure 6.8.

[2] In case of a finer binning, a minor deviation from unity in the ratio $n_{\mathrm{unf}}\big(T_j\big)/n_{\mathrm{mc}}\big(T_j\big)$ is indeed observed in the tail with lower statistics. This can be attributed to events with negative Monte Carlo weights. If such an event is filled into a rarely populated bin in the migration matrix, the final event count in this bin can become negative. The resulting unphysical negative $\mathrm{P}\big(R_i \,|\, T_j\big)$ can lead to instabilities in the unfolding procedure. Therefore, negative bins are set to zero instead. This can cause a minor non-closure for low-statistics bins.

$E_{\mathrm{T}}^{\mathrm{miss}}$ [GeV]	250–300	300–350	350–400	400–500
observed events (unfolded)	$12332\,^{+355}_{-363}$	$6928\,^{+282}_{-265}$	$3636\,^{+160}_{-177}$	$2902\,^{+152}_{-135}$
SM prediction (particle level)	$11464\,^{+976}_{-827}$	$6771\,^{+576}_{-489}$	$3462\,^{+296}_{-252}$	$2882\,^{+246}_{-209}$
$Z \to \nu\nu$	$4361\,^{+371}_{-314}$	$2974\,^{+253}_{-214}$	$1600\,^{+136}_{-115}$	$1399\,^{+119}_{-101}$
$W \to \tau\nu$	$2509\,^{+214}_{-181}$	$1376\,^{+118}_{-100}$	$668\,^{+57}_{-48}$	$521\,^{+45}_{-38}$
$W \to \mu\nu$	$2125\,^{+181}_{-154}$	$1125\,^{+96}_{-81}$	$570\,^{+49}_{-41}$	$465\,^{+40}_{-34}$
$W \to e\nu$	$1628\,^{+146}_{-126}$	$834\,^{+75}_{-65}$	$386\,^{+47}_{-44}$	$311\,^{+34}_{-31}$
top	$756\,^{+64}_{-55}$	$403\,^{+34}_{-29}$	$202\,^{+17}_{-15}$	$148\,^{+13}_{-11}$
diboson	$85\,^{+7}_{-6}$	$59\,^{+5}_{-4}$	$37\,^{+3}_{-3}$	$36\,^{+3}_{-3}$
$Z \to \mu\mu$	$0.0\,^{+0.0}_{-0.0}$	$0.0\,^{+0.0}_{-0.0}$	$0.0\,^{+0.0}_{-0.0}$	$0.0\,^{+0.0}_{-0.0}$

$E_{\mathrm{T}}^{\mathrm{miss}}$ [GeV]	500–600	600–700	> 700
observed events (unfolded)	$894\,^{+58}_{-54}$	$294\,^{+24}_{-25}$	$228\,^{+23}_{-23}$
SM prediction (particle level)	$880\,^{+76}_{-64}$	$296\,^{+26}_{-22}$	$217\,^{+20}_{-17}$
$Z \to \nu\nu$	$455\,^{+39}_{-33}$	$163\,^{+14}_{-12}$	$120\,^{+10}_{-9}$
$W \to \tau\nu$	$155\,^{+13}_{-11}$	$47\,^{+4}_{-4}$	$33\,^{+3}_{-3}$
$W \to \mu\nu$	$140\,^{+12}_{-10}$	$47\,^{+4}_{-4}$	$33\,^{+3}_{-3}$
$W \to e\nu$	$79\,^{+12}_{-12}$	$23\,^{+4}_{-4}$	$21\,^{+7}_{-7}$
top	$36\,^{+3}_{-3}$	$11\,^{+1}_{-1}$	$5.1\,^{+0.6}_{-0.5}$
diboson	$14\,^{+1}_{-1}$	$5.7\,^{+0.5}_{-0.4}$	$5.2\,^{+0.5}_{-0.4}$
$Z \to \mu\mu$	$0.0\,^{+0.0}_{-0.0}$	$0.0\,^{+0.0}_{-0.0}$	$0.0\,^{+0.0}_{-0.0}$

Table 6.6: Numbers of events in the single $E_{\mathrm{T}}^{\mathrm{miss}}$ bins, unfolded to particle level, in comparison to the Standard Model prediction. The stated uncertainties per process are the quadratic sum of the statistical and QCD scale uncertainties. Because of the assumed correlation of the QCD scale across processes, the individual uncertainties do not add up quadratically to the total one. The uncertainty on the unfolded result contains the statistical component as well as the systematic experimental uncertainties.

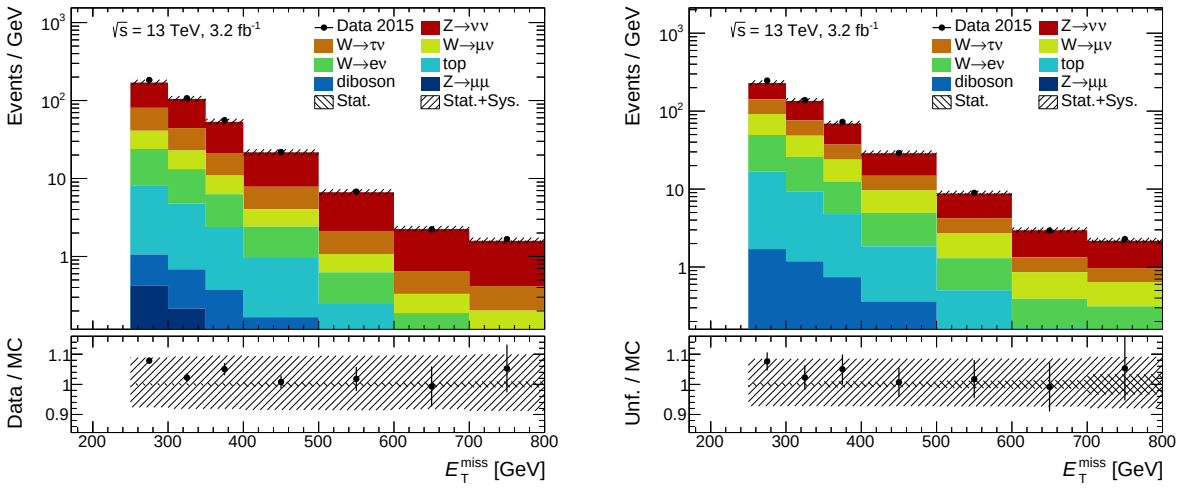

(a) Reconstruction level **(b)** Particle level

Figure 6.7: Observed $E_{\mathrm{T}}^{\mathrm{miss}}$ distribution compared to the Standard Model prediction in the mono-jet signal region **(a)** on reconstruction level and **(b)** unfolded to particle level. The systematic experimental uncertainties are shifted from the Monte Carlo prediction in **(a)** to the unfolded observation in **(b)**.

6.7 Signal Contribution

In order to constrain the selected BSM models using the observed events in the mono-jet signal region, the predicted number of events for said signal region must be known. As the observed $E_{\mathrm{T}}^{\mathrm{miss}}$ distribution was unfolded to particle level, the BSM models only need to be evaluated at particle level. This was the main motivation for unfolding in the beginning and the benefits become visible at this point as Monte Carlo samples without detector simulation can be used and an easy modification of objects in the final state is possible (e.g. declaring the decay products of a Higgs boson invisible).

The signal models are scaled to an integrated luminosity of $3.2\,\mathrm{fb}^{-1}$ and their event yield is evaluated int the seven $E_{\mathrm{T}}^{\mathrm{miss}}$ bins according to the particle-level selection criteria stated in Section 6.3. Results from the three studied signal models at selected masses are presented in Figure 6.9.

The stated event numbers of the heavy Higgs-like scalar are the sum of the $ZZ \to \nu\nu\nu\nu$ and the $ZZ \to \ell\ell\nu\nu$ processes. The latter dominates by orders of magnitudes because of the larger hadronic branching ratio of the Z boson and, more importantly, because no additional highly energetic initial state radiation is necessary. The result is an $E_{\mathrm{T}}^{\mathrm{miss}}$ spectrum rising up to a cut-off at approximately $m_H/2$ as the hadronically decaying and invisibly decaying Z bosons recoil against each other. Only minor differences between the production via gluon-gluon fusion or vector-boson fusion are visible, also indicating that the decay products of the heavy scalar are mainly responsible for the hard objects opposed to initial state radiation or the quarks that radiated the vector bosons. The peak structure results in an improved sensitivity to the heavy scalar with increasing m_H as the Standard Model background falls approximately exponentially with $E_{\mathrm{T}}^{\mathrm{miss}}$.

The invisibly decaying Standard Model Higgs boson also creates an exponentially falling $E_{\mathrm{T}}^{\mathrm{miss}}$ distribution comparable to the background processes but with a total cross

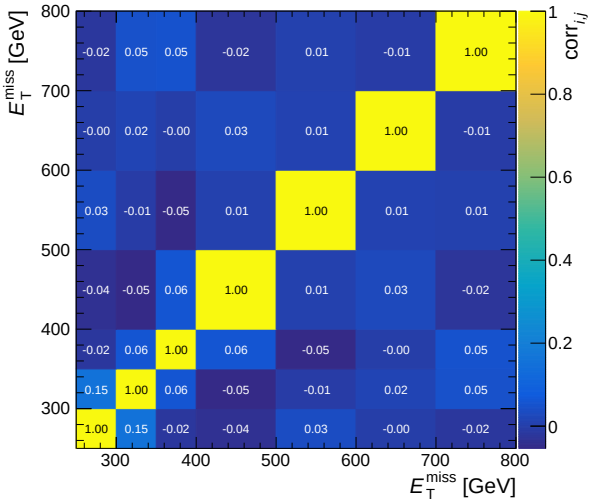

Figure 6.8: Correlation of the unfolded $E_{\mathrm{T}}^{\mathrm{miss}}$ distribution across bins, evaluated by the bootstrapping method. Because of the small amount of migrations, it is close to diagonal.

section which is approximately two orders of magnitude lower. This results in a relatively low sensitivity of the mono-jet signal region to this signal.

For the WIMP production via an axial-vector mediator, Monte Carlo samples for several mass points (m_A, m_χ) are studied. Each of these results in a separate $E_{\mathrm{T}}^{\mathrm{miss}}$ distribution. In order to combine these results with the mono-Z signal region, which provides samples at different mass points, an interpolation in the masses is performed. For each of the seven $E_{\mathrm{T}}^{\mathrm{miss}}$ bins, the available mass points with their corresponding number of events n_{mc} are arranged in the m_A-m_χ-plane and a Delaunay triangulation [97] is performed on these points. This splits the plane into a set of triangles with their vertices corresponding to known mass points. Inside these triangles, a planar interpolation between the three points is performed[3].

The result corresponds to a polygon spanned by the available $(m_A, m_\chi, n_{\mathrm{mc}})$ points per $E_{\mathrm{T}}^{\mathrm{miss}}$ bin. An example for this is provided in Figure 6.10. Notably, configurations with $m_\chi \gtrsim m_A/2$ are heavily suppressed because the mediator cannot be on-shell anymore. For $m_A < 800\,\mathrm{GeV}$, the majority of the available Monte Carlo samples are on or above that diagonal such that the interpolation in that region could deviate significantly from the true distribution. This results in a "spiky" structure of the interpolated signal dictated by the position of the Delaunay triangles. Additional Monte Carlo samples in this sensitive region would resolve this problem but their generation is accompanied with large computational effort.

In Chapter 8, these predicted distributions are used to constrain the different signal models by the observed numbers of events.

[3] As the event count can vary by orders of magnitude between points, the planar interpolation between the three vertices of a given triangle is performed with logarithmic z-axis.

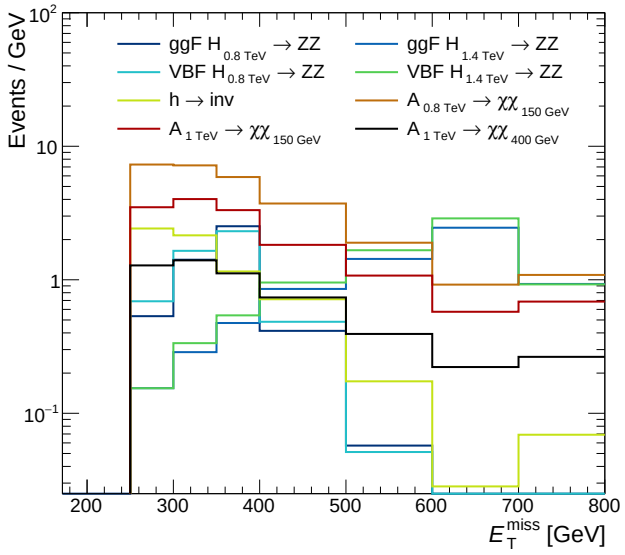

Figure 6.9: Predicted $E_{\mathrm{T}}^{\mathrm{miss}}$ distributions of selected signal samples. The depicted heavy Higgs-like scalar results correspond to a total production cross section of 1 pb. For the WIMP models, $g_q = 0.25$ and $g_\chi = 1$ were assumed.

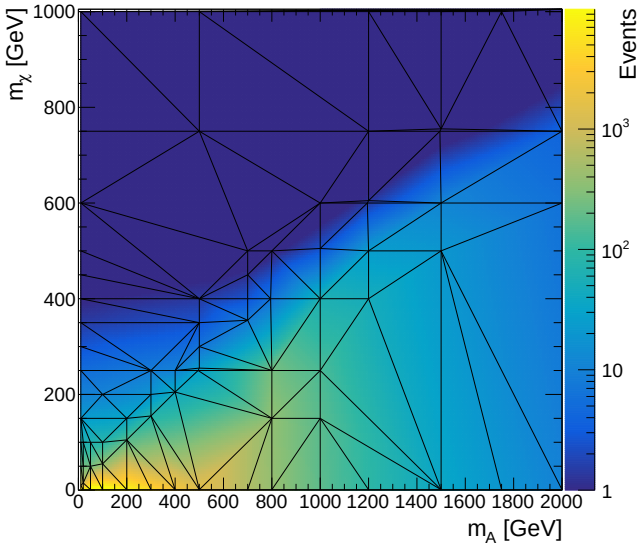

Figure 6.10: Event count of the $A \to \chi\bar{\chi}$ signal in the 250 GeV $< E_{\mathrm{T}}^{\mathrm{miss}} <$ 300 GeV bin, interpolated across the m_A-m_χ-plane. The vertices of the indicated Delaunay triangles correspond to mass points with an available Monte Carlo signal sample to evaluate the event count.

7 Mono-Z Search

Complementary to the mono-jet signature described above, this chapter presents the mono-Z signature with a Z-boson decaying into a e^+e^- or $\mu^+\mu^-$ pair instead of a jet as recoil partner for the invisible final state particles. It is less sensitive to the WIMP production via an axial-vector mediator because the necessary initial state radiation needs to be created via the weak coupling to a Z boson instead of the strong coupling to a gluon. However, it offers cleaner signatures for the invisible Higgs decay via the radiation of a Higgs boson from a Z boson and for heavy ZZ-resonances. By the requirement of a leptonic decay of the Z, the majority of the QCD backgrounds that are present in the mono-jet signature are suppressed. Additionally, the $E_{\mathrm{T}}^{\mathrm{miss}}$ is less likely to originate from a mismeasurement of a high-energy jet.

The chosen object and event selection criteria closely follow those in the ATLAS note [98] analyzing 13.3 fb^{-1} of 2015 and early 2016 data. The recently published ATLAS search [33] that includes the complete 2015 and 2016 data set, corresponding to an integrated luminosity of 36.1 fb^{-1}, uses a very similar definition of the signal region.

7.1 Monte Carlo Simulations

The dominant background process resulting in $E_{\mathrm{T}}^{\mathrm{miss}}$ and a recoiling e^+e^- or $\mu^+\mu^-$ pair is the production of two Z bosons where one decays into neutrinos and the other into said pair of charged leptons. A Feynman diagram of this is shown in Figure 7.1(a). It is an irreducible background and is estimated purely from Monte Carlo simulations.

Exchanging the Z boson decaying into neutrinos for a leptonically decaying W boson yields the sub-dominant WZ background as depicted in Figure 7.1(b). If the charged lepton from the W decay is either out of the detector's acceptance, missed, identified as jet or a hadronically decaying tau, the event can contribute to the signal region. As

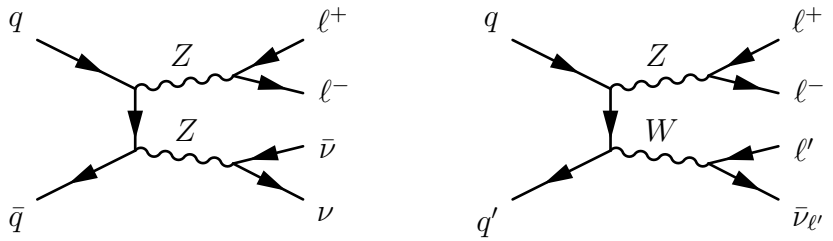

(a) ZZ background **(b)** WZ background

Figure 7.1: Tree-level Feynman diagrams for the dominant Standard Model backgrounds in the mono-Z topology. The ZZ background in **(a)** is irreducible as it creates exactly the expected signal topology. The reducible WZ background in **(b)** contributes to the signal region, if the charged lepton from the W boson is out of acceptance or not identified.

process	generator	PDF
$W \to \ell\nu$	Powheg + Pythia8 + EvtGen	CT10
$Z \to ee$	MadGraph + Pythia8 + EvtGen	NNPDF2.3 LO
$Z \to \mu\mu$	MadGraph + Pythia8 + EvtGen	NNPDF3.0 NLO
$Z \to \tau\tau$	MadGraph + Pythia8 + EvtGen	NNPDF2.3 LO
diboson	Powheg + Pythia8 + EvtGen	CT10
triboson	Sherpa2.2.1	CT10
$t\bar{t}$	Powheg + Pythia6 + EvtGen	CT10
single top	Powheg + Pythia6 + EvtGen	CT10
$A \to \chi\bar{\chi}$	MadGraph + Pythia8 + EvtGen	NNPDF3.0 NLO
$h \to$ inv	Powheg + Pythia8 + EvtGen	NNPDF3.0 NNLO
$H \to ZZ$	Powheg + Pythia8	CT10

Table 7.1: Generators and PDFs of the samples used in the mono-Z study. Descriptions of the listed generators are given in References [80–84, 99] and of the PDFs in References [85, 86].

this is partially a result of an imperfect reconstruction, WZ is a reducible background. Its shape is derived from the Monte Carlo prediction while the normalization is fixed to data by a 3-lepton control region described in Section 7.5.1.

The other backgrounds taken into account are the other decay channels of diboson production, contributions from $t\bar{t}$ or single-top events, the production of a single W or Z boson in association with jets and events containing three W or Z bosons. These are all estimated purely from the Monte Carlo prediction. Table 7.1 lists the generators and PDFs used to generate the Monte Carlo samples for each process. Like in the mono-jet analysis, they are interfaced to the Geant4 simulation of the ATLAS detector.

Additional samples are used for the evaluation of the signal models. The WIMP production via an axial-vector mediator is simulated for the same couplings $g_q = 0.25$ and $g_\chi = 1.0$ as used in the mono-jet analysis. However, the available mass points are different, which necessitates the interpolation in the mass plane as described in Section 6.7 in order to derive combined limits in Chapter 8.

The invisible Higgs decay is studied by a sample of Z boson production with subsequent radiation of a Higgs boson according to the Feynman diagram in Figure 2.4(c). As no samples with a completely invisible decay of the Higgs boson were available at the time of the study, a sample with the Higgs boson decaying into a ZZ pair is utilized where one Z boson decays into neutrinos and the other into charged leptons. The decay products of all Z bosons originating from a Higgs decay are made invisible like in the mono-jet analysis. Analogously, the sample is scaled to the total Zh production cross section of 0.88 pb [25] as if the Higgs would decay 100 % invisibly.

The study of heavy Higgs-like scalars is performed on the exact same $H \to ZZ \to \ell\ell\nu\nu$ samples as the mono-jet analysis, but without artificially making the Z decay products invisible. Gluon-gluon fusion and vector-boson fusion are also treated independently.

Pile-up effects are treated identically to the mono-jet analysis by reweighting Monte Carlo events in order to reproduce the observed distribution of the number of events per bunch-crossing.

7.2 Object Reconstruction

Additional selection criteria to those defined in Chapter 5 are required on reconstructed objects in order to be initially considered in this analysis. Electrons and muons can be assigned either baseline or signal quality. The former are used in the overlap removal and the $\vec{E}_{\mathrm{T}}^{\mathrm{miss}}$ calculation and to reject events with more than two identified charged leptons, while the latter are requirements for the selected e^+e^- or $\mu^+\mu^-$ pair.

To be considered as baseline, electrons must have $p_{\mathrm{T}} > 7\,\mathrm{GeV}$ and $|\eta| < 2.47$, and must fulfill the loose quality criteria. Those which also satisfy the medium likelihood and have impact parameters consistent with the primary vertex (d_0-significance $\left|d_0/\sigma(d_0)\right| < 5$ and $|z_0 \cdot \sin\theta| < 0.5\,\mathrm{mm}$) are considered as signal electrons.

A similar selection for muons is applied. Muons of loose quality with $p_{\mathrm{T}} > 7\,\mathrm{GeV}$ and $|\eta| < 2.5$ are defined as baseline, those with medium quality, $\left|d_0/\sigma(d_0)\right| < 3$ and $|z_0 \cdot \sin\theta| < 0.5\,\mathrm{mm}$ are defined as signal.

Jets are required to have $p_{\mathrm{T}} > 20\,\mathrm{GeV}$ and $|\eta| < 4.5$ to be considered. The MV2c10 b-tagging algorithm [100, 101] is used to identify jets potentially containing b hadrons, utilizing their relatively long lifetime ($\tau \approx 1.5\,\mathrm{ps}$, $c\tau \approx 450\,\mu\mathrm{m}$), high mass and decay multiplicities. A working point of 85 % identification efficiency of b-jets with a rejection factor of 33 for light-flavour jets is selected.

Photons with tight quality and $p_{\mathrm{T}} > 20\,\mathrm{GeV}$ are considered as calibrated objects for the $E_{\mathrm{T}}^{\mathrm{miss}}$ calculation.

7.3 Event Selection

To be considered in this analysis, events must have been selected by one of the single-muon triggers `HLT_mu20_iloose_L1MU15` or `HLT_mu50`, or by one of the single-electron triggers `HLT_e24_lhmedium_L1EM20VH`, `HLT_e60_lhmedium` or `HLT_e120_lhloose`. The requirements for each of these trigger items are listed in Table A.3. An efficiency of $\geq 98\,\%$ has been found in Reference [34] for this set of triggers with a definition of the signal region as in this study.

The cleaner final state and the usage of lepton triggers instead of the $E_{\mathrm{T}}^{\mathrm{miss}}$ trigger allows to lower the $E_{\mathrm{T}}^{\mathrm{miss}}$ threshold to 90 GeV for this analysis. At even lower $E_{\mathrm{T}}^{\mathrm{miss}}$, the signal region would be dominated by $Z \to \ell\ell$ production with fake $E_{\mathrm{T}}^{\mathrm{miss}}$ from jet mismeasurements. The complete set of criteria defining the mono-Z signal region is listed in Table 7.2.

To select events with a recoiling Z boson, exactly one e^+e^- or $\mu^+\mu^-$ pair is required. These two selected leptons must have the signal quality defined in Section 7.2 while events with additional baseline electrons and muons are rejected, reducing the WZ background. The leading lepton must exceed a transverse momentum of 30 GeV, the sub-leading must exceed 20 GeV. In order to suppress the background of non-resonant lepton production, the invariant mass $m_{\ell\ell}$ of the selected pair is required to lie within a window of $\pm 15\,\mathrm{GeV}$ around the mass of the Z boson.

Additional cuts are placed in order to specifically select events with the Z boson recoiling against the invisible final state particles. They are expected to be emitted back-to-back which is assured by requiring a minimal azimuthal angle between the $p_{\mathrm{T}}^{\ell\ell}$ of

the dilepton-system and the missing transverse energy of $\Delta\phi\big(\vec{p}_{\mathrm{T}}^{\,\ell\ell}, \vec{E}_{\mathrm{T}}^{\mathrm{miss}}\big) > 2.7$. At the same time, the two leptons are expected to exhibit some degree of collimation due to the transversal momentum of the Z boson. As its mass of $m_Z = 91\,\mathrm{GeV}$ is not small in comparison to its expected $p_{\mathrm{T}} > 90\,\mathrm{GeV}$, only a loose upper threshold on the angular separation of the two leptons of $\Delta R_{\ell\ell} < 1.8$ is chosen. This suppresses the Z+jets as well as the diboson backgrounds. A third requirement on the momentum balance is applied by the so-called fractional p_{T} difference $\left|\left|\vec{E}_{\mathrm{T}}^{\mathrm{miss}} + \sum_{\mathrm{jets}} \vec{p}_{\mathrm{T}}^{\,\mathrm{jet}}\right| - p_{\mathrm{T}}^{\ell\ell}\right| / p_{\mathrm{T}}^{\ell\ell}$. The sum of the missing transverse energy and the transverse momentum of all identified jets is required to deviate from the missing transverse energy of the dilepton system by at most 20 %. Similarly, a cut on the transverse mass m_{T} of the $\vec{E}_{\mathrm{T}}^{\mathrm{miss}}$ and the dilepton system is placed. In the approximation of massless decay products, it is given by

$$m_{\mathrm{T}} = \sqrt{2 p_{\mathrm{T}}^{\ell\ell} E_{\mathrm{T}}^{\mathrm{miss}} \Big(1 - \cos\Delta\phi\big(\vec{p}_{\mathrm{T}}^{\,\ell\ell},\, \vec{E}_{\mathrm{T}}^{\mathrm{miss}}\big)\Big)}\,. \tag{7.1}$$

In case of a perfect balance $\vec{E}_{\mathrm{T}}^{\mathrm{miss}} = -\vec{p}_{\mathrm{T}}^{\,\ell\ell}$ as expected from the signal, this equation becomes $p_{\mathrm{T}}^{\ell\ell} = m_{\mathrm{T}}/2$. A corresponding requirement of $p_{\mathrm{T}}^{\ell\ell}/m_{\mathrm{T}} < 0.9$ is applied.

In order to further reduce the contribution of mismeasured jets to the missing transverse energy, a minimal azimuthal angle to any identified jet with $p_{\mathrm{T}} > 25\,\mathrm{GeV}$ of $\Delta\phi\big(\vec{E}_{\mathrm{T}}^{\mathrm{miss}}, \mathrm{jets}\big) > 0.7$ is required. Background from $t\bar{t}$ and single-top contributions are suppressed by rejecting events containing identified b-jets.

Finally, the same rejection of non-collision background and of Monte Carlo events with weights deviating by more than 100 RMS from the mean as in the mono-jet analysis is performed.

The fiducial phase space on particle level is defined by the same selection criteria as listed in Table 7.2. They directly correspond to the criteria on reconstruction level minus the object quality requirements and the non-collision background rejection. A jet is labelled as b-jet, if a b hadron with $p_{\mathrm{T}} > 5\,\mathrm{GeV}$ exists within a radius of $\Delta R < 0.3$ around it. If several jets exist within this cone around the b-hadron, it is only associated to the closest one in ΔR space.

To fix the normalization of the WZ background, a control region enriched with this process is defined. Besides the selected e^+e^- or $\mu^+\mu^-$ pair fulfilling the Z mass window and p_{T} criteria, an additional $e^\pm$ or $\mu^\pm$ with $p_{\mathrm{T}} > 20\,\mathrm{GeV}$ and signal quality is required. Events containing a fourth lepton satisfying the baseline quality are rejected. The W candidate consisting of the third lepton and the missing transverse energy must have a transverse mass m_{T}^W of at least 60 GeV. It is defined analogously to Equation 7.1 but with the transverse momentum of the third lepton instead of the dilepton system. In the case that the third lepton is of the same flavor as the signal pair, an ambiguity in assigning them as the Z- and W-candidates exists. If that is not resolved by the requirement of the Z mass window $|m_{\ell\ell} - m_Z| < 15\,\mathrm{GeV}$, the event is accepted if any permutation fulfills the m_{T}^W criterion. To reduce background contributions from top quarks, events containing b-jets are rejected like in the signal region.

For the WZ control region, no fiducial phase space is defined because the normalization is derived on reconstruction level in the following. As it only consists of a comparison of data to the Standard Model prediction, nothing is to be gained from unfolding.

one pair of e^+e^- or $\mu^+\mu^-$, no additional $e^\pm$ or $\mu^\pm$ with $p_\mathrm{T} > 7\,\mathrm{GeV}$	
leading lepton p_T	$> 30\,\mathrm{GeV}$
sub-leading lepton p_T	$> 20\,\mathrm{GeV}$
$E_\mathrm{T}^\mathrm{miss}$	$> 90\,\mathrm{GeV}$
$\lvert m_{\ell\ell} - m_Z \rvert$	$< 15\,\mathrm{GeV}$
$\Delta R_{\ell\ell}$	< 1.8
$\Delta\phi\big(\vec{p}_\mathrm{T}^{\,\ell\ell}, \vec{E}_\mathrm{T}^\mathrm{miss}\big)$	> 2.7
$\Big\lvert \big\lvert \vec{E}_\mathrm{T}^\mathrm{miss} + \sum_\mathrm{jets} \vec{p}_\mathrm{T}^\,\mathrm{jet} \big\rvert - p_\mathrm{T}^{\ell\ell} \Big\rvert / p_\mathrm{T}^{\ell\ell}$, jets with $p_\mathrm{T} > 20\,\mathrm{GeV}$	< 0.2
$\Delta\phi\big(\vec{E}_\mathrm{T}^\mathrm{miss}, \mathrm{jets}\big)$, jets with $p_\mathrm{T} > 25\,\mathrm{GeV}$	> 0.7
$p_\mathrm{T}^{\ell\ell} / m_\mathrm{T}$	< 0.9
number of b-jets with $p_\mathrm{T} > 20\,\mathrm{GeV}, \lvert\eta\rvert < 2.5$	$= 0$

Table 7.2: Event selection criteria for the mono-Z signal region. Besides the quality requirements on reconstructed objects as defined in Section 7.2 and the cleaning from non-collision background, they are chosen identically on reconstruction and particle level.

one pair of e^+e^- or $\mu^+\mu^-$, third $e^\pm$ or $\mu^\pm$ with $p_\mathrm{T} > 20\,\mathrm{GeV}$, no fourth $e^\pm$ or $\mu^\pm$ with $p_\mathrm{T} > 7\,\mathrm{GeV}$	
leading Z lepton p_T	$> 30\,\mathrm{GeV}$
sub-leading Z lepton p_T	$> 20\,\mathrm{GeV}$
$\lvert m_{\ell\ell} - m_Z \rvert$	$< 15\,\mathrm{GeV}$
m_T^W	$> 60\,\mathrm{GeV}$
number of b-jets with $p_\mathrm{T} > 20\,\mathrm{GeV}, \lvert\eta\rvert < 2.5$	$= 0$

Table 7.3: Event selection criteria for the WZ control region. They are based on reconstructed objects fulfilling the quality requirements defined in Section 7.2. Additional cleaning from non-collision background is applied.

process	sim. events	cross section deviation	
		$\mu_R = \frac{0.5\mu_0}{2\mu_0}$	$\mu_F = \frac{0.5\mu_0}{2\mu_0}$
$ZZ \to ee\nu\nu$	1 000 000	$^{+5.8\,\%}_{-4.8\,\%}$	$^{+0.3\,\%}_{-0.5\,\%}$
$A \to \chi\bar{\chi} + \gamma$	200 000	$^{+3.2\,\%}_{-2.3\,\%}$	$^{+2.5\,\%}_{-2.0\,\%}$
Zh	10 000 000	$^{+2.2\,\%}_{-1.8\,\%}$	$^{-1.2\,\%}_{+0.9\,\%}$
$h \to ZZ \to \mu\mu\nu\nu$	1 000 000	$^{+36.8\,\%}_{-24.9\,\%}$	$^{+8.0\,\%}_{-7.2\,\%}$

Table 7.4: Total cross section uncertainties based on QCD scale choices derived by MCFM8.0.

7.4 Uncertainties

Uncertainties in this analysis are handled identically to the mono-jet analysis as described in Section 6.4. Since electrons and muons are now part of the final state, all systematic experimental uncertainties listed in Table 6.3 have an impact on the Monte Carlo prediction.

The theoretical uncertainties on the cross sections are also determined by the use of MCFM8.0 at next-to-leading order. The uncertainty on the full Standard Model prediction is approximated by its dominant contribution. For the mono-$Z(\to ee)$ decay channel, this is the $ZZ \to ee\nu\nu$ process and the for the muon decay channel $ZZ \to \mu\mu\nu\nu$ respectively. As no significant difference in the QCD scale response is expected between these two processes, $ZZ \to ee\nu\nu$ is used to approximate the uncertainty in both channels.

The uncertainty on the cross section of the WIMP production is evaluated at $m_A = 1\,\text{TeV}$ and $m_\chi = 100\,\text{GeV}$ in association with a photon from initial state radiation. As only QCD processes are affected by the scale choices, the difference to the $A \to \chi\bar{\chi} + Z$ process of interest is expected to be small.

The production of a Standard Model Higgs boson $h \to ZZ \to \mu\mu\nu\nu$ is evaluated to estimate the uncertainty on heavy Higgs-like ZZ resonances. Like in the mono-jet analysis, this process is very sensitive to the choice of the QCD scales because of large contribution from terms of high order in α_S.

Except for the Higgs radiation process that does not offer an invisible Higgs decay, a minimal missing transverse energy of 90 GeV is required in the cross section calculations. The results are presented in Table 7.4.

7.5 Results on Reconstruction Level

7.5.1 WZ Control Region

The WZ control region is evaluated first in order to fix the normalization of the WZ background in the signal region. In the analyzed 2015 data corresponding to $3.2\,\text{fb}^{-1}$, 433 events fulfilling the selection criteria have been observed. Split into the four possible decay channels $e^+e^-e^\pm$, $e^+e^-\mu^\pm$, $\mu^+\mu^-e^\pm$, $\mu^+\mu^-\mu^\pm$, their E_T^miss distributions in comparison to the Standard Model prediction are shown in Figure A.2. By design of the selection

channel		events	scale factor f^{WZ}
	observed events	118	
$e^+e^-e^\pm$	WZ prediction	$64.6 \pm 1.4\,^{+3.4}_{-4.8}$	$1.13 \pm 0.26\,^{+0.18}_{-0.16}$
	bkg prediction	$45.0 \pm 12.9\,^{+7.6}_{-7.9}$	
	observed events	80	
$e^+e^-\mu^\pm$	WZ prediction	$67.3 \pm 1.3\,^{+2.4}_{-3.3}$	$1.03 \pm 0.14\,^{+0.09}_{-0.06}$
	bkg prediction	$11.1 \pm 2.8\,^{+3.0}_{-4.2}$	
	observed events	120	
$\mu^+\mu^-e^\pm$	WZ prediction	$71.4 \pm 1.3\,^{+1.9}_{-2.5}$	$1.25 \pm 0.29\,^{+0.10}_{-0.08}$
	bkg prediction	$30.8 \pm 16.6\,^{+4.9}_{-5.8}$	
	observed events	111	
$\mu^+\mu^-\mu^\pm$	WZ prediction	$87.2 \pm 1.5\,^{+1.5}_{-2.5}$	$1.19 \pm 0.12\,^{+0.03}_{-0.02}$
	bkg prediction	$7.2 \pm 0.4\,^{+0.5}_{-0.4}$	

Table 7.5: Observed numbers of events in the WZ control region in comparison to the Standard Model prediction. The background prediction includes all considered Standard Model processes other than WZ production. The stated uncertainties are the symmetrical statistical component evaluated by bootstrapping and the quadratic sum of all experimental systematic uncertainties.

criteria, the WZ process is the dominant contribution. Depending on the decay channel, a purity between 59 % and 92 % is reached. These results are used to derive a scale factor f^{WZ} to normalize the WZ Monte Carlo prediction. It is given by the ratio of observed events and the prediction after subtraction of the other remaining Standard Model processes:

$$f^{WZ} = \frac{n_{\text{data}} - \sum_{\text{bkg}} n_{\text{mc}}^{\text{bkg}}}{n_{\text{mc}}^{WZ}} \,. \tag{7.2}$$

This ratio is calculated for all bootstrapped replicas and the root mean square of the resulting distribution is used to estimate the statistical uncertainty on f^{WZ}. Table 7.5 lists the results for each of the four decay channels. Those with an electron as third lepton still have a considerable contribution from the $Z \to \ell\ell$ background, presumably because of jets being misidentified as electrons. This misidentification is more likely to happen for the third leptons as opposed to the pair, because the latter is constrained by the Z mass window. As the corresponding Monte Carlo sample is associated with a relatively large statistical uncertainty, these two channels are not as sensitive for the determination of f^{WZ}.

The same scale factor is to be expected for all four decay channels which allows to combine the result to reduce the uncertainties. As the channels are orthogonal, their bootstrapped likelihoods $\mathcal{L}\big(f^{WZ}\big)$ are assumed to be independent for a fixed set of

systematic variations, such that they multiply to the total distribution:

$$\mathcal{L}_{\text{tot}}\left(f^{WZ}\right) \propto \mathcal{L}_{eee}\left(f^{WZ}\right) \cdot \mathcal{L}_{ee\mu}\left(f^{WZ}\right) \cdot \mathcal{L}_{\mu\mu e}\left(f^{WZ}\right) \cdot \mathcal{L}_{\mu\mu\mu}\left(f^{WZ}\right). \tag{7.3}$$

The likelihoods of the individual channels as well as the combined one are shown in Figure A.3. Using the mean[1] and root mean square of this distribution and quadratically summing the effects of systematic variations yields the final scale factor

$$f_{\text{total}} = 1.12 \pm 0.07\,^{+0.05}_{-0.04}. \tag{7.4}$$

This factor is used to scale up the predicted cross section of the WZ background, improving the agreement between data and Monte Carlo estimate. The propagation of the derived uncertainties is omitted in the following. The WZ background makes up only $\approx 25\,\%$ of the total number of events and a $7\,\%$ uncertainty on this is well below the overall statistical uncertainty of both observed data and the Monte Carlo prediction. Ultimately, the study of this control region mainly serves as validation for the used methods to properly reproduce the observation in the selected phase space.

7.5.2 Signal Region

With this fixed scaling, the signal region can be evaluated. In total, 87 events meeting the selection criteria have been observed in the analyzed 2015 data set, of which 39 occurred in the e^+e^- decay channel and 48 in the $\mu^+\mu^-$ decay channel. This exceeds the Standard Model prediction of $31.1 \pm 1.3\,^{+4.7}_{-2.9}$ and $37.3 \pm 1.3\,^{+2.7}_{-2.8}$, respectively, by $\approx 20\,\%$ in both cases. Assuming a Poissonian distribution of the observed number of events around the Monte Carlo prediction with associated uncertainty $\sigma_{\text{Poiss}} \approx \sqrt{n_{\text{mc}}}$, this corresponds to an underestimation by 1.1σ and 1.6σ, respectively, after quadratically summing all sources of uncertainty. Any potentially unconsidered systematic effect thus does not induce a significant deviation.

The kinematic distributions of the observed events in comparison to the Standard Model prediction are provided in Figures A.4 and A.5. Because of the low number of events in the signal region, they are associated with relatively large uncertainties on both the observation and prediction. With respect to these, no significant deviation is observed.

Like for the mono-jet signature, the $E_{\text{T}}^{\text{miss}}$ distribution is used as discriminant for the following statistical analysis in Chapter 8. Because of the overall low number of events, a coarse binning into the three $E_{\text{T}}^{\text{miss}}$ [GeV] regions 90–120, 120–180 and > 180 is applied. This allows for a certain degree of distinction between the Standard Model background and the signal models favoring larger $E_{\text{T}}^{\text{miss}}$ (Figure 7.7.) without degrading the available statistics per bin too far.

The resulting binned results in comparison to the Standard Model prediction are presented in Table 7.6, the composition of the stated uncertainties is listed in Table A.4. The uncertainty in the e^+e^- channel strongly depends on the $E_{\text{T}}^{\text{miss}}$ region, mainly because of the $Z \to \ell\ell$ process. At the nominal value of the experimental nuisance

[1] As the profiled likelihoods are approximately symmetrical, this is close to selecting the maximum likelihood. The latter would require some kind of interpolation as the distribution obtained by 1000 replicas is not sufficiently smooth.

$E_{\mathrm{T}}^{\mathrm{miss}}$ [GeV]	90–120	120–180	> 180
e^+e^- channel			
observed events	15	20	4
SM prediction	$13.0\,^{+4.3}_{-2.4}$	$11.9\,^{+1.4}_{-1.3}$	$6.1\,^{+0.7}_{-0.6}$
ZZ	$6.6\,^{+0.6}_{-0.6}$	$7.7\,^{+0.8}_{-0.7}$	$5.0\,^{+0.6}_{-0.5}$
WZ	$3.5\,^{+0.6}_{-0.4}$	$3.0\,^{+0.4}_{-0.4}$	$1.1\,^{+0.2}_{-0.2}$
top	$2.0\,^{+1.5}_{-1.5}$	$0.9\,^{+0.9}_{-0.9}$	$0.0\,^{+0.0}_{-0.0}$
WW	$0.9\,^{+0.9}_{-0.9}$	$0.3\,^{+0.3}_{-0.3}$	$0.0\,^{+0.0}_{-0.0}$
$Z \to \ell\ell$	$0.0\,^{+2.6}_{-0.0}$	$0.0\,^{+0.0}_{-0.0}$	$0.0\,^{+0.0}_{-0.0}$
$\mu^+\mu^-$ channel			
observed events	25	14	9
SM prediction	$15.9\,^{+1.7}_{-2.0}$	$14.1\,^{+1.2}_{-1.1}$	$7.3\,^{+0.7}_{-0.7}$
ZZ	$8.1\,^{+0.8}_{-1.0}$	$9.5\,^{+0.8}_{-0.7}$	$5.8\,^{+0.6}_{-0.5}$
WZ	$5.0\,^{+0.6}_{-0.8}$	$4.6\,^{+0.5}_{-0.6}$	$1.4\,^{+0.3}_{-0.3}$
top	$2.0\,^{+0.9}_{-0.9}$	$0.0\,^{+0.4}_{-0.3}$	$0.0\,^{+0.0}_{-0.0}$
WW	$0.8\,^{+0.6}_{-0.6}$	$0.0\,^{+0.0}_{-0.0}$	$0.0\,^{+0.0}_{-0.0}$
$Z \to \ell\ell$	$0.0\,^{+0.1}_{-0.0}$	$0.0\,^{+0.0}_{-0.0}$	$0.0\,^{+0.0}_{-0.0}$

Table 7.6: Observed numbers of events in the three $E_{\mathrm{T}}^{\mathrm{miss}}$ bins in comparison to the Standard Model prediction. Triboson production and $W \to \ell\nu$ are omitted as they result in < 0.1 events in each bin. The stated uncertainties per process are the quadratic sum of the statistical, systematic experimental and QCD scale uncertainties. No uncertainty on the observed events is quoted, but they can be assumed to follow a Poissonian around the Standard Model prediction.

parameters, its contribution is < 0.1 events and thus negligible. But for a systematic variation of the jet energy resolution by $+1\sigma$, it induces a non-negligible background of 2.5 events (19 %) in the lowest $E_{\mathrm{T}}^{\mathrm{miss}}$ bin. Sub-dominant are the jet energy scale ($< 14\,\%$) mainly acting on the top background in the lowest bin and the statistical uncertainty ($\approx 7\,\%$) across all bins.

The uncertainty in the $\mu^+\mu^-$ channel is dominated by the statistical component (4–7 %), the uncertainty on the renormalization scale ($\approx 5\,\%$) and, in the lowest bin, the jet energy scale ($< 8\,\%$).

Overall, these effects on the Monte Carlo estimate are small in comparison to the statistical uncertainty of the observed numbers of events. This makes the mono-Z signature statistically limited, unlike the mono-jet signature which is dominated by the renormalization scale uncertainty. The latter proves beneficial in the derivation of combined limits in Chapter 8.

In order to compare these results to the signal model predictions, an unfolding procedure analogous to the mono-jet analysis is performed in the following section.

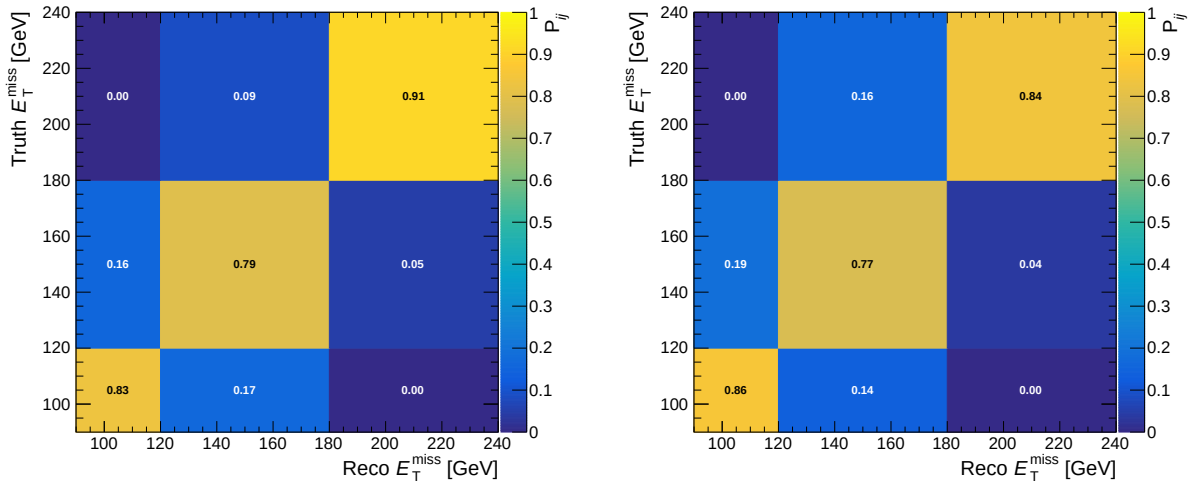

(a) e^+e^- channel **(b)** $\mu^+\mu^-$ channel

Figure 7.2: Migration matrix A_{ij} of the mono-Z signal region, normalized to unity across the x-axis, for the two considered decay channels. This corresponds to the folding probability P_{ij} from Equation 3.1 without missed events.

7.6 Unfolding

Like in the mono-jet analysis, the binning on reconstruction level is also adopted on particle level. Because of the large bin widths, migrations become relatively small in both channels, with less than 20 % between neighboring bins and less than 1 % between the outer bins (Figure 7.2). The unfolding of this topology is thus comparably robust towards the choice of the employed method as can be seen in Figure 7.3 showing the difference between the Bayesian results after different numbers of iterations in the e^+e^- channel. The observed variations are of the order of the statistical uncertainty, the deviation between one and ten iterations corresponds to $\chi^2_{\text{red}} < 1$, for example. A comparison to the IDS method is given in Figure 7.4. It yields a stable result after 3 iterations while the Bayesian method produces deviations monotonically increasing with the number of iterations. This confirms the self-stabilizing nature observed in the mono-jet unfolding and motivates the choice of the IDS method in the following. The corresponding results for the $\mu^+\mu^-$ channel, as presented in Figures A.7 and A.8, are comparable.

The implementation of both methods is verified in a closure check identical to the one described in Section 6.6. No deviations from perfect closure are observed and the statistical uncertainties assigned to the unfolded result via the bootstrapping method correctly reproduce the statistical uncertainty of the Monte Carlo particle level distribution (Figure A.6).

Systematic uncertainties are handled analogously to the mono-jet analysis by unfolding the observed distribution under the assumption of the several varied Monte Carlo reconstruction level distributions and migration matrices. QCD scale uncertainties are not propagated to the unfolded result as they are applied to the particle level Monte Carlo predictions for the derivation of limits in Chapter 8.

The resulting $E_{\text{T}}^{\text{miss}}$ distributions in both channels, unfolded with the IDS method and three iterations, are presented in Table 7.7 and Figure 7.5. The composition of

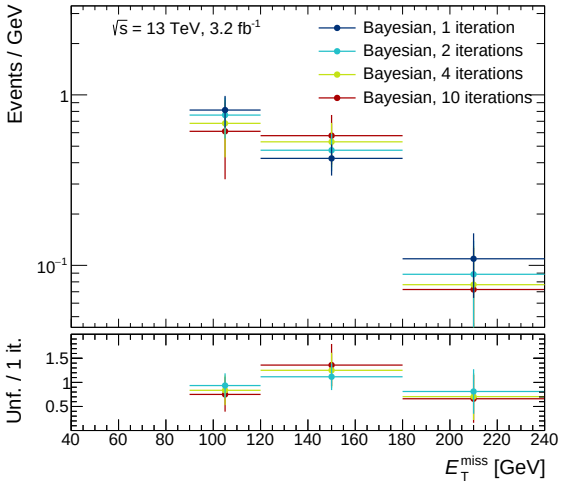

Figure 7.3: Observed $E_{\mathrm{T}}^{\mathrm{miss}}$ distribution in the e^+e^- channel unfolded to particle level with the Bayesian algorithm for different numbers of iterations. Indicated is only the statistical uncertainty.

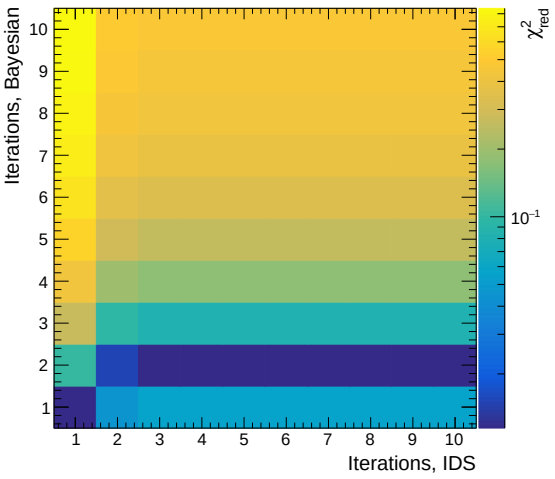

Figure 7.4: χ^2_{red} as defined in Equation 6.2 between the $E_{\mathrm{T}}^{\mathrm{miss}}$ distribution in the e^+e^- channel unfolded via the Bayesian and IDS algorithm for different numbers of iterations.

the stated uncertainties is detailed in Table A.5. The statistical uncertainty from the observed number of events (22–50 %) dominates in both channels for all bins. The only non-negligible systematic contributions originate from the jet energy scale and resolution corresponding to up to 23 % in the lowest $E_{\mathrm{T}}^{\mathrm{miss}}$ bin. The overfluctuations in the observed number of events in the lowest (second) $E_{\mathrm{T}}^{\mathrm{miss}}$ bin in the $\mu^+\mu^-$ (e^+e^-) channel are preserved.

The Standard Model prediction on particle level is consistent between the two channels within 2σ of the statistical uncertainties. As no processes with asymmetric behavior between electrons and muons are included, this meets the expectation.

As in the mono-jet analysis, the unfolded results need to be paired with the correlations of the statistical uncertainties which are created by migrating events between bins. Because of the large bin widths, these are relatively small ($\leq 5\,\%$). The full correlation matrices for both channels are given in Figure 7.6.

7.7 Signal Contribution

The contribution of the considered signal models to the mono-Z signature is evaluated on particle level such that they can be constrained by the observed $E_{\mathrm{T}}^{\mathrm{miss}}$ distribution unfolded to particle level. The available Monte Carlo samples are scaled to the recorded integrated luminosity of $3.2\,\mathrm{fb}^{-1}$ and events fulfilling the particle level criteria mentioned in Section 7.3 are selected. The results for all three signal models with selected mass parameters in the e^+e^- channel, separated into the three $E_{\mathrm{T}}^{\mathrm{miss}}$ bins, are presented in Figure 7.7. In the $\mu^+\mu^-$ channel, these distributions behave very similarly with deviations

$E_{\mathrm{T}}^{\mathrm{miss}}$ [GeV]	90–120	120–180	> 180
e^+e^- channel			
observed events (unfolded)	$22.6\,^{+8.3}_{-7.5}$	$27.2\,^{+6.6}_{-6.6}$	$5.8\,^{+2.9}_{-2.9}$
SM prediction (particle level)	$19.7\,^{+1.6}_{-1.5}$	$16.4\,^{+1.3}_{-1.2}$	$8.8\,^{+0.8}_{-0.7}$
ZZ	$10.4\,^{+0.8}_{-0.7}$	$10.7\,^{+0.8}_{-0.7}$	$7.1\,^{+0.6}_{-0.6}$
WZ	$4.7\,^{+0.5}_{-0.4}$	$3.0\,^{+0.3}_{-0.3}$	$1.4\,^{+0.2}_{-0.2}$
top	$3.4\,^{+0.9}_{-0.9}$	$2.0\,^{+0.7}_{-0.7}$	$0.3\,^{+0.3}_{-0.3}$
WW	$0.8\,^{+0.5}_{-0.5}$	$0.6\,^{+0.4}_{-0.4}$	$0.0\,^{+0.0}_{-0.0}$
$Z \to \ell\ell$	$0.4\,^{+0.4}_{-0.4}$	$0.0\,^{+0.0}_{-0.0}$	$0.0\,^{+0.0}_{-0.0}$
$\mu^+\mu^-$ channel			
observed events (unfolded)	$33.3\,^{+8.4}_{-7.8}$	$18.7\,^{+4.9}_{-4.9}$	$11.5\,^{+3.8}_{-3.8}$
SM prediction (particle level)	$20.4\,^{+1.7}_{-1.6}$	$18.6\,^{+1.4}_{-1.3}$	$9.3\,^{+0.8}_{-0.7}$
ZZ	$10.4\,^{+0.8}_{-0.7}$	$12.5\,^{+0.9}_{-0.8}$	$7.2\,^{+0.6}_{-0.6}$
WZ	$4.4\,^{+0.4}_{-0.4}$	$4.2\,^{+0.4}_{-0.4}$	$1.7\,^{+0.2}_{-0.2}$
top	$5.2\,^{+1.1}_{-1.1}$	$1.8\,^{+0.7}_{-0.7}$	$0.3\,^{+0.3}_{-0.3}$
WW	$0.4\,^{+0.3}_{-0.3}$	$0.0\,^{+0.0}_{-0.0}$	$0.0\,^{+0.0}_{-0.0}$
$Z \to \ell\ell$	$0.0\,^{+0.0}_{-0.0}$	$0.0\,^{+0.0}_{-0.0}$	$0.0\,^{+0.0}_{-0.0}$

Table 7.7: Numbers of events in the three $E_{\mathrm{T}}^{\mathrm{miss}}$ bins for both decay channels, unfolded to particle level, in comparison to the Standard Model prediction. The stated uncertainties per process are the quadratic sum of the statistical and QCD scale uncertainties. The uncertainty on the unfolded result contains the statistical component as well as the systematic experimental uncertainties.

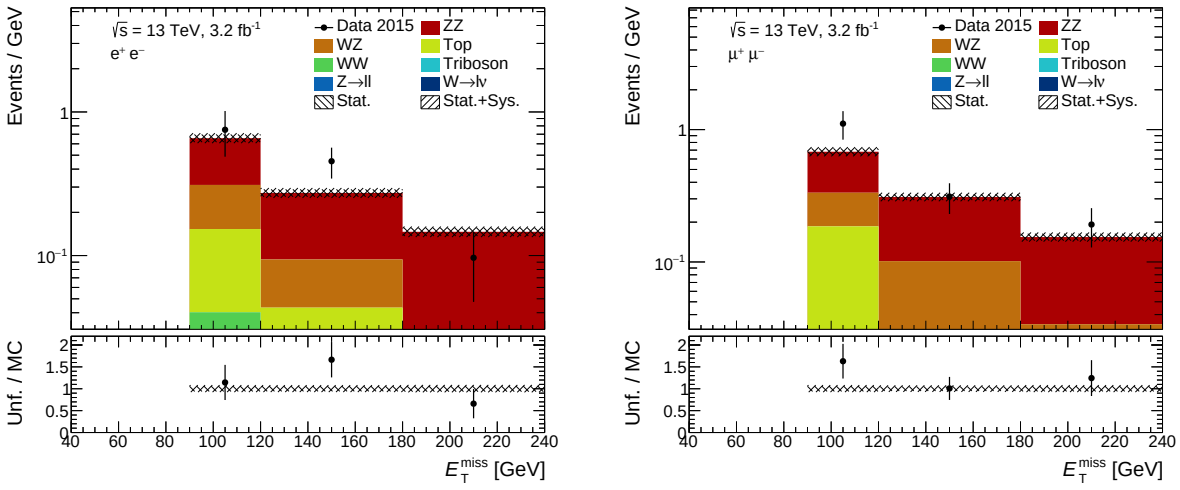

(a) e^+e^- channel **(b)** $\mu^+\mu^-$ channel

Figure 7.5: Observed $E_{\mathrm{T}}^{\mathrm{miss}}$ distributions unfolded to particle level compared to the Standard Model prediction in the two decay channels of the mono-Z signal region. The uncertainties indicated for the unfolded result contain both the statistical component and the systematic experimental variations, among which the former dominates. Both the statistical and the QCD scale uncertainties present in the Monte Carlo prediction are small in comparison.

being of the order of the statistical uncertainties[2] (Figure A.9).

As observed in the mono-jet analysis, the heavy Higgs-like scalar decaying into a pair of Z bosons favors $E_{\mathrm{T}}^{\mathrm{miss}}$ in the order of $m_H/2$. For the studied masses of $m_H \geq 400\,\mathrm{GeV}$, this mostly results in a large deposition in the highest $E_{\mathrm{T}}^{\mathrm{miss}}$ bin ($> 180\,\mathrm{GeV}$) which offers a good distinction from the Standard Model backgrounds. Only at $m_H = 400\,\mathrm{GeV}$, the majority of the events populate the $120\,\mathrm{GeV} < E_{\mathrm{T}}^{\mathrm{miss}} < 180\,\mathrm{GeV}$ bin, reducing the sensitivity to a heavy scalar of this mass as a larger background is present. The production of the scalar via gluon-gluon fusion versus vector-boson fusion does not create significant shape differences, only a minor overall scaling. As additional jets associated with the vector-boson fusion only enter the selection criteria via $\Delta\phi\big(\vec{E}_{\mathrm{T}}^{\mathrm{miss}}, \mathrm{jets}\big)$ and the required balance of the dilepton system against the missing transverse energy and jets, this is to be expected.

The invisible Higgs decay produces an approximately exponentially falling $E_{\mathrm{T}}^{\mathrm{miss}}$ distribution like in the mono-jet signature. The production via Higgs radiation from a Z boson, however, results in ≈ 10 times less events than via gluon-gluon fusion with an associated jet or vector-boson fusion. But since the Standard Model background is simultaneously suppressed by a factor of ≈ 200, the mono-Z topology is ultimately more sensitive to the invisible Higgs decay. This is confirmed by the limits derived in Chapter 8.

The production of WIMPs via an axial-vector mediator creates a similarly falling $E_{\mathrm{T}}^{\mathrm{miss}}$ spectrum. In comparison to the mono-jet selection, the mono-Z selection is suppressed by a factor of $\mathcal{O}(10^3)$ because the initial state radiation of a jet via the strong coupling

[2] Minor differences could arise due to the different handling of particle level electrons and muons overlapping with jets.

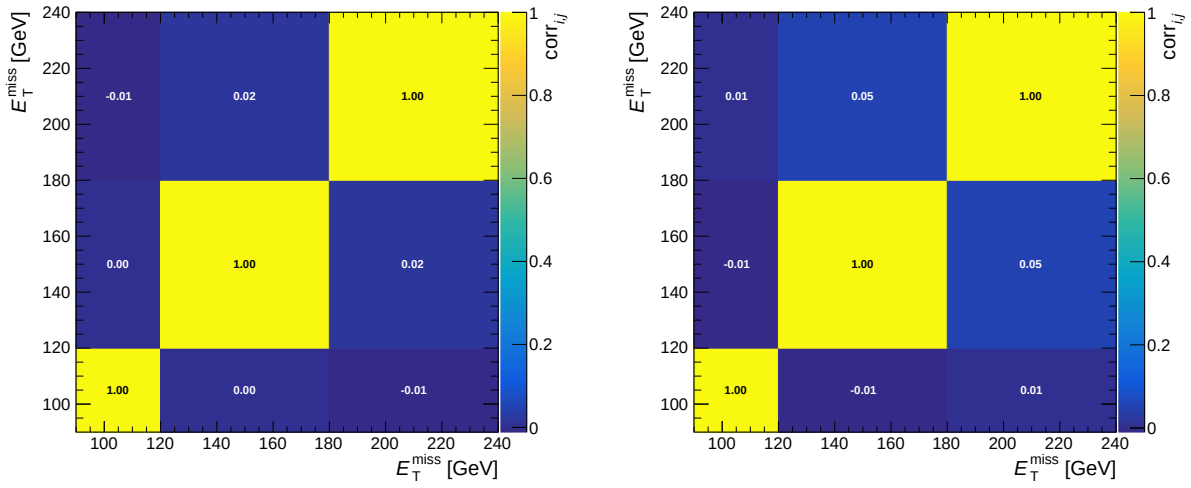

(a) e^+e^- channel **(b)** $\mu^+\mu^-$ channel

Figure 7.6: Correlation of the unfolded $E_{\mathrm{T}}^{\mathrm{miss}}$ distributions in both decay channels across bins as determined by the bootstrapping method. Because of the small amount of migrations, they are close to diagonal.

needs to be replaced by the radiation of a Z boson via the weak coupling. This results in the lowered sensitivity of the mono-Z signature to this signal model as determined in Chapter 8.

In order to combine the results with the mono-jet signature, the m_A-m_χ-plane per $E_{\mathrm{T}}^{\mathrm{miss}}$ bin is interpolated with a Delaunay triangulation identical to the description in Section 6.7. An example for the interpolated plane is provided in Figure 7.8. A structure similar to the results in the mono-jet analysis is observed with a weak dependence on m_χ up to the steep edge at $m_\chi = m_A/2$. As more samples are available in the sensitive region $m_\chi < m_A/2$, the interpolation is smoother than it is the case for the mono-jet analysis. In the white regions, no samples are available to base the interpolation on. As these are also the regions of almost vanishing sensitivity, zero is assumed for the number of signal events in these areas.

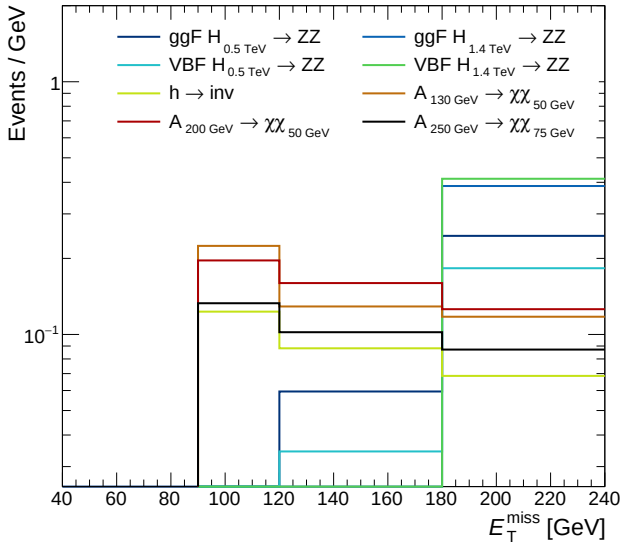

Figure 7.7: Predicted $E_{\mathrm{T}}^{\mathrm{miss}}$ distributions in the e^+e^- channel of selected signal samples. The depicted heavy Higgs-like scalar results correspond to a total production cross section of 1 pb. For the WIMP models, $g_q = 0.25$ and $g_\chi = 1$ were assumed.

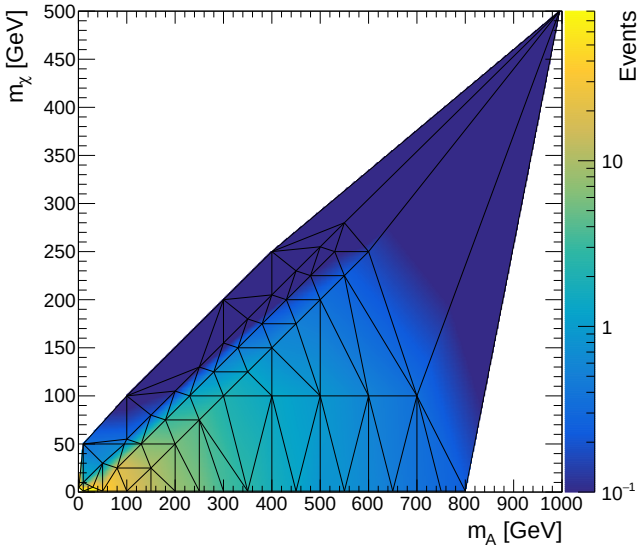

Figure 7.8: Event count of the $A \to \chi\bar{\chi}$ signal in the $90\,\mathrm{GeV} < E_{\mathrm{T}}^{\mathrm{miss}} < 120\,\mathrm{GeV}$ bin of the e^+e^- decay channel, interpolated across the m_A-m_χ-plane. The vertices of the indicated Delaunay triangles correspond to mass points with an available Monte Carlo signal sample to evaluate the event count. The white regions are set to zero due to a lack of information.

8 Derivation of Limits

Since no significant deviation between the Standard Model prediction and the recorded data has been observed, the results can be used to constrain the parameters of given new physics models. With the measured distributions unfolded to particle level, this procedure can be easily performed for any current or future models with generated Monte Carlo events on particle level. This chapter presents the derivation of limits on the three considered models of WIMP production via an axial-vector mediator, an invisible Higgs decay and a heavy Higgs-like ZZ resonance.

To demonstrate the potential benefit of combining different unfolded signatures, limits are derived from the mono-jet and the mono-Z results separately as well as in a combined analysis.

8.1 CL_s Limits

This section introduces the CL_s method widespread in high-energy physics for deriving frequentist motivated exclusion limits on parameters of a given signal model [102]. It provides a modified confidence level (CL) that considers both CL_{s+b} under the signal-plus-background hypothesis and CL_b under the background-only hypothesis. Unlike CL_{s+b}, CL_s is not prone to excluding signals to which the search is not sensitive. The following description is based on the usual procedure of deriving limits in ATLAS [103].

To derive any confidence level, the likelihood of the model parameters given the unfolded observation in the N_T particle level $E_{\mathrm{T}}^{\mathrm{miss}}$ bins must be evaluated. As no more quantities at reconstruction level are necessary, the notation is shortened in the following:

$$u_j \equiv n_{\mathrm{unf}}\big(T_j\big)\,, \tag{8.1}$$

$$b_j \equiv n_{\mathrm{mc}}^{\mathrm{SM}}\big(T_j\big)\,, \tag{8.2}$$

$$s_j \equiv n_{\mathrm{mc}}^{\mathrm{signal}}\big(T_j\big)\,. \tag{8.3}$$

These quantities are accompanied by their corresponding statistical uncertainties σ_{stat} obtained by the bootstrapping method. They also depend on a set of nuisance parameters $\boldsymbol{\theta} = \{\theta_k\}$ parametrizing the considered systematic variations, split into the 18 experimental ones $\boldsymbol{\theta^{\mathrm{ex}}} = \{\theta_k^{\mathrm{ex}}\}$ acting on the unfolded result and the 2 theoretical QCD scale uncertainties $\boldsymbol{\theta^{\mathrm{th}}} = \{\theta_k^{\mathrm{th}}\}$ acting on the prediction. Each nuisance parameter must be constrained by a probability density function $h_k\big(\theta_k \,|\, \tilde{\theta}_k\big)$ expressing the prior knowledge from other experiments or theoretical considerations with a nominal value of $\tilde{\theta}_k$.

The parameter of interest for a given signal model in this thesis is the *signal strength* μ. It scales the cross section of the signal added on top of the Standard Model background such that the prediction in a certain bin becomes $b_j + \mu \cdot s_j$. The likelihood of observing a set of statistically *independent* quantities $\boldsymbol{u} = \{u_j\}$ under the assumption of a certain value of μ and a set of nuisance parameters $\boldsymbol{\theta}$, is the product of the probability densities

g of the observations in each bin given the model prediction and the prior probability densities of each nuisance parameter:

$$\mathcal{L}_{\text{indep}}\big(\boldsymbol{u} \,|\, \mu, \boldsymbol{\theta}\big) \propto \prod_j g\big(u_j|\mu, \boldsymbol{\theta}\big) \prod_k h_k\big(\theta_k \,|\, \tilde{\theta}_k\big)\,. \tag{8.4}$$

This expression demonstrates the influence of the nuisance parameters on the likelihood. Varying one of the parameters may improve the agreement between observation and prediction and thus increase the first term. But this comes with a penalty for deviating the parameter from its nominal value by $h_k\big(\theta_k \,|\, \tilde{\theta}_k\big)$. A scan in the space of the 20 considered nuisance parameters is thus necessary in order to find the maximum likelihood for a value of μ given the set of observations.

In a common search on reconstruction level, g would be modeled by a Poissonian distribution around the expectation as it corresponds to a counting experiment in the selected bin. The statistical uncertainties on the background and signal prediction would then be handled by additional nuisance parameters if they are not negligible. The unfolding procedure, however, does not retain the Poissonian behavior because of the efficiency corrections and migrations. The bootstrapping approach allows to reconstruct the actual distribution and, with a sufficient number of replicas, the resulting histogram can directly be used as the probability density function. In order to reduce the computational effort, the distributions of u_j, b_j and s_j are approximated as Gaussians in the following with the standard deviations determined by the bootstrapping method. With that choice, the probability density of observing an unfolded result u_j given the background and signal expectation becomes

$$g\big(u_j \,|\, \mu, \boldsymbol{\theta}\big) = \frac{1}{\sqrt{2\pi\sigma^2_{\text{tot},j}}} \exp\left(-\frac{\Delta^2_j(\mu, \boldsymbol{\theta})}{2\sigma^2_{\text{tot},j}}\right) \tag{8.5}$$

$$\Delta_j(\mu, \boldsymbol{\theta}) = u_j\big(\boldsymbol{\theta}^{\mathbf{ex}}\big) - \Big(b_j\big(\boldsymbol{\theta}^{\mathbf{th}}\big) + \mu \cdot s_j\big(\boldsymbol{\theta}^{\mathbf{th}}\big)\Big) \tag{8.6}$$

$$\sigma^2_{\text{tot},j} = \sigma^2_{\text{stat}}\big(u_j\big) + \sigma^2_{\text{stat}}\big(b_j\big) + \mu^2\sigma^2_{\text{stat}}\big(s_j\big)\,. \tag{8.7}$$

These equations express that the difference $\Delta_j(\mu, \boldsymbol{\theta})$ between the observation and expectation must behave Gaussian as well with a mean of 0 and a standard deviation of $\sigma^2_{\text{tot},j}$. The dependence of u_j on the experimental variations is evaluated by varying the underlying quantity by $\pm 1\sigma$ to determine the influence on the event count as listed in Tables A.1 and A.4. The resulting up and down variations are symmetrized by taking the mean to arrive at the uncertainty $\sigma_k\big(u_j\big)$ induced by a nuisance parameter θ_k which is varied by one standard deviation. If the nuisance parameters are expressed in units of their standard deviations and centered at a nominal value of $\tilde{\theta}_k = 0$, the varied unfolded result in a bin is given by

$$u_j\big(\boldsymbol{\theta}^{\mathbf{ex}}\big) = u_j\big(\tilde{\boldsymbol{\theta}}^{\mathbf{ex}}\big) + \sum_k \Big(\theta_k \cdot \sigma_k\big(u_j\big)\Big)\,, \tag{8.8}$$

where $u_j\big(\tilde{\boldsymbol{\theta}}^{\mathbf{ex}}\big)$ is the unfolded result obtained with all nuisance parameters set to their nominal value. In this choice of variables, the constraints p_k for the experimental nuisance

parameters become standard normal distributions with a mean of 0 and standard deviation of 1:

$$p_k\left(\theta_k^{\mathrm{ex}}\right) = \frac{1}{\sqrt{2\pi}} \exp\left(-\frac{1}{2}\left(\theta_k^{\mathrm{ex}}\right)^2\right). \tag{8.9}$$

The theoretical systematic variations acting on the background and signal predictions are handled analogously to Equation (8.8). The calculated QCD scale uncertainties listed in Tables 6.4 and 7.4 are symmetrized by averaging the up- and down-variation. The results are $\sigma_k\left(b_j\right)$ approximated by the respective dominant background contribution in both signatures and $\sigma_k\left(s_j\right)$ of the tested signal process. Unlike the experimental uncertainties, however, the constraints of the theoretical uncertainties are not assumed to be Gaussian. Instead, a flat probability density between -1 and 1 and 0 outside of this interval is assigned:

$$p_k\left(\theta_k^{\mathrm{th}}\right) = \begin{cases} 1/2\,, & \text{if } -1 \leq \theta_k^{\mathrm{th}} \leq 1 \\ 0\,, & \text{otherwise} \end{cases}. \tag{8.10}$$

This reflects that no preferred choice of the renormalization and factorization scale exists besides that it should be of the order of the typical energy in the involved process.

With these choices, the likelihood $\mathcal{L}_{\mathrm{indep}}$ from Equation 8.4 is fully defined. It contains the product of N_T Gaussians for each particle level bin and a Gaussian or flat probability density function as constraint for the nuisance parameters. However, a statistically independent set of measurements $\boldsymbol{u}$ was assumed for Equation 8.4 which does not necessarily hold for unfolded distributions because of the introduced correlations between bins. The independent Gaussians thus need to be replaced by an N_T-dimensional multivariate Gaussian in order to account for correlations:

$$\mathcal{L}\left(\boldsymbol{u} \,|\, \mu, \boldsymbol{\theta}\right) \propto \exp\left(-\frac{1}{2}\boldsymbol{\Delta}^T(\mu, \boldsymbol{\theta}) \cdot \boldsymbol{V}^{-1} \cdot \boldsymbol{\Delta}(\mu, \boldsymbol{\theta})\right) \prod_k h_k\left(\theta_k \,|\, \tilde{\theta}_k\right), \tag{8.11}$$

where $\boldsymbol{\Delta}(\mu, \boldsymbol{\theta})$ is the vector of the differences between observation and expectation as defined in Equation 8.6 over all N_T truth bins. The covariance matrix $\boldsymbol{V}$ needs to account for the statistical uncertainties of the observed distribution, Standard Model prediction and signal prediction, analogous to Equation 8.7:

$$V_{ij} = \mathrm{cov}_{ij}^{\mathrm{unf}} + \delta_{ij}\left(\sigma_{\mathrm{stat}}^2\left(b_j\right) + \mu^2 \sigma_{\mathrm{stat}}^2\left(s_j\right)\right), \tag{8.12}$$

where $\mathrm{cov}_{ij}^{\mathrm{unf}}$ is the covariance of the unfolded result as obtained by the bootstrapping method via Equation 3.28. The statistical uncertainties of the background and signal prediction only enter on the diagonal as they are truly independent across bins. In the case of a diagonal $\mathrm{cov}^{\mathrm{unf}}$, the independent Gaussians from Equation 8.4 are restored. In the following, the contribution of $\sigma_{\mathrm{stat}}^2\left(s_j\right)$ is omitted because a covariance independent of the parameter of interest μ can be evaluated more efficiently in the RooStats framework which is used for the derivation of limits in this thesis. It is negligible in comparison to the uncertainty of the unfolded distribution and the Standard Model background.

The likelihood $\mathcal{L}(\boldsymbol{u} \,|\, \mu, \boldsymbol{\theta})$ can now be used to construct the test statistic q_μ for the following hypothesis tests based on the profile likelihood ratio λ_μ:

$$q_\mu = \begin{cases} -2 \ln \lambda_\mu \,, & \text{if } \mu \geq \hat{\mu} \geq 0 \\ 0 \,, & \text{otherwise} \end{cases} \tag{8.13}$$

$$\lambda_\mu = \frac{\mathcal{L}(\boldsymbol{u} \,|\, \mu, \hat{\boldsymbol{\theta}}_\mu)}{\mathcal{L}(\boldsymbol{u} \,|\, \hat{\mu}, \hat{\boldsymbol{\theta}}_{\hat{\mu}})} \,, \tag{8.14}$$

where $\hat{\boldsymbol{\theta}}_\mu$ is the set of nuisance parameters that maximizes $\mathcal{L}(\boldsymbol{u} \,|\, \mu, \boldsymbol{\theta})$ for a given μ, and $\hat{\mu}$ the parameter of interest corresponding to the global maximum of $\mathcal{L}(\boldsymbol{u} \,|\, \hat{\mu}, \hat{\boldsymbol{\theta}}_{\hat{\mu}})$. q_μ is thus always positive. Demanding $\hat{\mu} \geq 0$ reflects the requirement for a positive signal cross section. $\mu \geq \hat{\mu}$ ensures that a one-sided confidence interval is derived. Physically, this corresponds to not excluding signal processes in the presence of upwards fluctuations of the data such that the most likely $\hat{\mu}$ exceeds the tested μ.

For a certain value of μ under test, a measurement as presented in this thesis corresponds to a single observed value q_μ^{obs} of the test statistic. In order to derive confidence levels from this measurement, the probability density $f(q_\mu|\mu)$ of the test statistic under the signal-plus-background hypothesis and $f(q_\mu|0)$ under the background-only hypothesis must be known.

They are typically constructed by generating a large number of pseudo-data sets under both hypotheses and evaluating q_μ for each of these pseudo-experiments. Depending on the complexity of $\mathcal{L}$, especially the number of nuisance parameters to profile over, this approach can be computationally very demanding in order to arrive at an accurate representation of f.

An alternative to this is given by the analytic *asymptotic approximation* based on a theorem by A. Wald [104] that for large numbers of events the profile likelihood ratio behaves approximately as

$$-2 \ln \lambda_\mu \approx \frac{(\mu - \hat{\mu})^2}{\sigma^2} \,, \tag{8.15}$$

where the maximum-likelihood estimate $\hat{\mu}$ is Gaussian distributed around the true value μ' with a yet to be determined variance σ^2. As a generalization of Wilks' theorem [105], Reference [106] shows that this results in the following probability density function for q_μ:

$$f(q_\mu \,|\, \mu') = \Phi\left(\frac{\mu - \mu'}{\sigma}\right)\delta(q_\mu) + \frac{1}{\sqrt{8\pi q_\mu}} \exp\left[-\frac{1}{2}\left(\sqrt{q_\mu} - \frac{\mu - \mu'}{\sigma}\right)^2\right] , \tag{8.16}$$

where Φ is the cumulative distribution function of the standard normal distribution and δ the Dirac delta function. This expression can be used to evaluate the background-only hypothesis with $\mu' = 0$ and the signal-plus-background hypothesis with $\mu' = \mu$.

To evaluate the variance σ^2 of the signal strength μ around its maximum-likelihood value $\hat{\mu}$, one often utilizes the so-called "Asimov data set". It is assumed to provide maximum-likelihood estimates $\hat{\mu}$ and $\hat{\boldsymbol{\theta}}_{\hat{\mu}}$ identical to the true values μ' and $\boldsymbol{\theta}'$. For such

a data set, Equation 8.15 becomes

$$q_\mu^A \approx \frac{(\mu - \mu')^2}{\sigma^2}\,, \qquad \text{for } \mu \geq \mu' \geq 0\,. \tag{8.17}$$

The standard deviation σ, which characterizes the probability density in Equation 8.16, can thus be derived from the test statistic q_μ^A observed in the Asimov data set. In a real world application, however, no exact equivalent of the Asimov data set exists unless the background prediction and nuisance parameters are known exactly. Instead, it is usually approximated by the already available background-only Monte Carlo prediction with nuisance parameters at their nominal values.

With the probability density of the test statistic according to Equation 8.16, the p-value of the signal-plus-background hypothesis for a certain signal strength μ is given by

$$\mathrm{CL_{s+b}}(\mu) = \mathrm{P}\Big(q_\mu \geq q_\mu^{\mathrm{obs}} \,|\, \mathrm{s{+}b}\Big) = \int_{q_\mu^{\mathrm{obs}}}^{\infty} f\big(q_\mu \,|\, \mu\big)\,\mathrm{d}q_\mu\,. \tag{8.18}$$

It is the probability of an experiment to yield a test statistic q_μ equal to or less likely than the observed one, if the signal-plus-background hypothesis were true. This can be translated into a confidence interval by defining a threshold α, conventionally 0.05, and rejecting the signal-plus-background hypothesis for values of μ where $\mathrm{CL_{s+b}}(\mu) < \alpha$. In the considered case of an observation consistent with the background prediction, this confidence interval turns into an upper limit on μ. One then speaks of an exclusion of signal strengths above this limit at a $1 - \alpha = 95\,\%$ confidence level.

The $\mathrm{CL_{s+b}}$ method has the unphysical drawback that it can potentially exclude signals it is not sensitive to. If in Equation 8.15 the variance σ^2 becomes large due to a low sensitivity of the experiment to the signal strength, the expected probability densities $f\big(q_\mu \,|\, \mu\big)$ and $f\big(q_\mu \,|\, 0\big)$ become more alike as the difference between μ and 0 becomes small in terms of σ. Intuitively, no rejection of the signal-plus-background hypothesis should be possible in this case because both hypotheses explain an observation equally well (or badly). The $\mathrm{CL_{s+b}}$ method, however, does not consider $f\big(q_\mu \,|\, 0\big)$ and would thus exclude a signal in case of a downward fluctuation of the data that causes an unexpectedly large q_μ^{obs}.

To overcome this issue, the p-value of the background-only hypothesis needs to be considered as well:

$$1 - \mathrm{CL_b}(\mu) = \mathrm{P}\Big(q_\mu \geq q_\mu^{\mathrm{obs}} \,|\, \mathrm{b}\Big) = \int_{q_\mu^{\mathrm{obs}}}^{\infty} f\big(q_\mu \,|\, 0\big)\,\mathrm{d}q_\mu\,, \tag{8.19}$$

The $\mathrm{CL_s}$ method uses this second p-value to penalize cases where the data is similarly unlikely under the background-only hypothesis:

$$\mathrm{CL_s}(\mu) = \frac{\mathrm{CL_{s+b}}(\mu)}{1 - \mathrm{CL_b}(\mu)}\,. \tag{8.20}$$

Although $\mathrm{CL_s}(\mu)$ is no longer strictly a p-value, the translation to confidence intervals is performed analogously by rejecting regions of $\mathrm{CL_s}(\mu) < \alpha$. In the expected case of an

observation consistent with the background-only hypothesis, the result is similar to the $\mathrm{CL_{s+b}}$ method because $1 - \mathrm{CL_b}(\mu)$ is of order 1. At the same time, the false rejection of signal in an insensitive experiment is suppressed as $\mathrm{CL_{s+b}}(\mu)$ and $1 - \mathrm{CL_b}(\mu)$ assume similar values. Note, that the rejection of signal according to the $\mathrm{CL_s}$ method is always more conservative than the $\mathrm{CL_{s+b}}$ method because $0 \leq \mathrm{CL_b}(\mu) < 1$ and consequently $\mathrm{CL_s}(\mu) > \mathrm{CL_{s+b}}(\mu)$.

In addition to the *observed limit* on μ as derived by the procedure described above, an *expected limit* is typically published in comparison. The latter describes the limit that is predicted for the experiment under the assumption that no signal is present. It is obtained by replacing the observed q_μ^{obs} by the q_μ corresponding to the median of $f\big(q_\mu \,|\, 0\big)$, which is exactly q_μ^A of the background-only Asimov data set. Uncertainty bands on the expectation can be derived by repeating this with quantiles corresponding to $\pm 1\sigma$ and $\pm 2\sigma$ around the median.

8.2 Combination of Signatures

One of the main aspects of this thesis is to derive limits under simultaneous consideration of multiple signatures. In the notation as introduced above, this step becomes straightforward. Equation 8.11 provides the definition of the likelihood, given observations and predictions in N_T particle level bins with potential statistical correlations between them. These do not need to originate from the same measurement, but can include any bins from multiple signatures.

For the two searches presented in this thesis, this means that limits can be derived by considering only the seven $E_{\mathrm{T}}^{\mathrm{miss}}$ bins of the mono-jet signature, only the six bins of the mono-Z signature (three $E_{\mathrm{T}}^{\mathrm{miss}}$ bins per decay channel) as well as all thirteen at the same time. Input for the likelihood are the unfolded results and particle level Standard Model predictions as listed in Tables 6.6 and 7.7 with their dependence on the experimental nuisance parameters as given in Tables A.2 and A.5 and the QCD scales in Tables 6.4 and 7.4. For the signal predictions of the three considered models, the results from Sections 6.7 and 7.7 together with the respective QCD scale uncertainties of the process are used.

The covariance $\mathrm{cov}_{ij}^{\mathrm{unf}}$ between unfolded bins of the same distribution is calculated using the bootstrapping method as previously discussed. The covariance between bins of different signatures vanishes if the considered signatures are orthogonal, meaning no event can appear in several distributions. This is (approximately) the case for the searches presented in this thesis, as the mono-jet selection rejects events with any identified leptons, the mono-$Z(\to ee)$ requires electrons and rejects events with muons, and the mono-$Z(\to \mu\mu)$ selection requires this conversely[1]. Otherwise, the covariance can be evaluated completely analogously by the bootstrapping method, due to the event-specific seed for the random number generation.

The prior $\prod_k h_k\big(\theta_k \,|\, \tilde{\theta}_k\big)$ of the nuisance parameters remains unchanged since the same systematic uncertainties are assumed to act on both signatures fully correlated. If, for

[1] Approximately, because the definition of electrons and muons in the mono-jet and the mono-Z analysis are not identical. Nonetheless, no event has been observed that meets the selection criteria of both signatures.

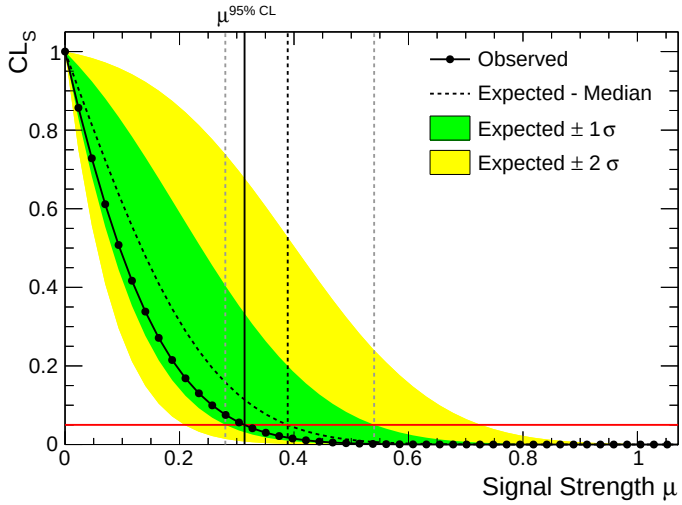

Figure 8.1: Scan in the signal strength μ to find the upper limit $\mu^{95\%\,\mathrm{CL}}$ corresponding to $\mathrm{CL_s}\left(\mu^{95\%\,\mathrm{CL}}\right) = 0.05$. The vertical solid line indicates the observed limit and the dashed lines the expected limit with $\pm 1\sigma$ uncertainties. Shown is the evaluation of the mono-jet only analysis for $m_A = 800\,\mathrm{GeV}$ and $m_\chi = 250\,\mathrm{GeV}$.

example, results from different experiments were to be combined, their uncertainties would need to be described by different nuisance parameters which act on the corresponding distributions only.

With this procedure, $\mathrm{CL_s}$ limits on the three considered signal models are derived in the following sections.

8.2.1 Axial-Vector WIMP Production

Since the predicted number of events in the case of WIMP production via an axial-vector mediator depends on the masses m_A and m_χ and the couplings g_q and g_χ, limits need to be derived in dependence of these parameters as well. The two couplings, however, only correspond to a different normalization of the predicted distributions, which allows identifying them with the signal strength in the following. At a fixed mass point, an upper limit on the signal strength μ at a 95 % confidence level is derived by finding the value of μ corresponding to $\mathrm{CL_s}\left(\mu\right) = 0.05$. This value is denoted as $\mu^{95\%\,\mathrm{CL}}$. The determination is illustrated in Figure 8.1 where the red line corresponds to the threshold $\alpha = 0.05$. It shows the observed and expected $\mathrm{CL_s}$ as a function of the signal strength μ with the uncertainty bands on the latter. Since μ scales the signal cross section, the signal-plus-background hypothesis is better distinguishable from the background-only hypothesis with increasing μ. This results in the monotonically falling $\mathrm{CL_s}(\mu)$. $\mu^{95\%\,\mathrm{CL}}$ is then identified as the point of intersection with the threshold. This way, the observed and expected limit with its uncertainties can be derived at any arbitrary point in the m_A-m_χ-plane with the interpolated signal predictions from Sections 6.7 and 7.7.

As signal predictions under the nominal assumption of $g_q = 0.25$ and $g_\chi = 1.0$ are used, $\mu = 1$ corresponds to a signal production of WIMPs with these couplings. The total cross section of the process scales quadratically with the couplings (Equation 2.18) and since the signal strength μ is used to scale the cross section of a signal model, it can

be interpreted as

$$\mu = \left(\frac{g_q}{0.25}\right)^2 \cdot \left(\frac{g_\chi}{1.0}\right)^2 = 16\, g_q^2 g_\chi^2 \,. \tag{8.21}$$

The upper limit $\mu^{95\%\,\mathrm{CL}}$ can thus directly be translated into an upper limit on $g_q^2 g_\chi^2$. If, for example, $\mu^{95\%\,\mathrm{CL}} = 0.5$ is observed at a certain mass point, all mediators with $g_q^2 g_\chi^2 > 1/32$ are excluded at a 95 % confidence level at this mass.

The derivation of $\mu^{95\%\,\mathrm{CL}}$ across the m_A-m_χ-plane is performed three times: only considering the seven bins of the mono-jet analysis, only considering the six bins of the mono-Z analysis and in a combined analysis considering all thirteen bins. The observed values are presented in the left column of Figure 8.2. The solid black line corresponds to the observed contour of $\mu^{95\%\,\mathrm{CL}} = 1$ and the dashed lines indicate the expected contour with its $\pm 1\sigma$ uncertainty band. These contours are the edge of the excluded mass region of WIMP production via an axial-vector mediator for models with $g_q^2 g_\chi^2 > 1/16$ as shown in the right column of Figure 8.2. Exclusion regions for any value of the couplings can be constructed by the corresponding contour of $\mu^{95\%\,\mathrm{CL}} = 16\, g_q^2 g_\chi^2$.

In all three diagrams, the typical triangular shape is visible since configurations with an off-shell mediator with $m_A < 2m_\chi$ are strongly suppressed. The mono-jet analysis allows to exclude mediator masses m_A of up to 1.2–1.4 TeV, depending on the WIMP mass m_χ. The mono-Z analysis is significantly less sensitive to this signal process and only allows to exclude m_A up to 270–360 GeV. This reduced sensitivity is to be expected due to the necessary initial state radiation of a Z boson via the weak interaction as opposed to a jet via the strong interaction. In both cases, the observed limit lies within the 1σ-band of the expected limit which confirms that the data does not significantly deviate from the background-only prediction.

The low sensitivity of the mono-Z topology to the signal process leads to exclusion limits of the combined analysis that are very similar to the mono-jet only analysis. The expected limit for $m_A < 400$ GeV is improved slightly by the combination as this is the region in which the mono-Z analysis offers sensitivity. For larger mediator masses, the expected combined limit is close to identical to the expected limit of the mono-jet analysis alone. The observed limit of the combined analysis is still mostly within the $\pm 1\sigma$ band but is shifted by approximately 0.2σ with respect to the observed limit of the mono-jet analysis alone, even for large m_A. Since the expected limit did not change in this region, this is no sign of an increased sensitivity of the combined analysis. Instead, the additional considered bins lead to different maximum-likelihood estimates of the systematic uncertainties, which are in turn favorable for stronger limits in the mono-jet analysis.

Ultimately, the combined analysis of both signatures only yields a minor improvement of the sensitivity to WIMP production via an axial vector mediator in comparison to the mono-jet analysis alone because the mono-Z signature lacks sensitivity to this signal model. But as no further effort is associated with considering multiple signatures for which unfolded results are available, there is no compelling reason not to include these additional bins. The potential benefit, on the other hand, is shown in the following sections for the other signal models.

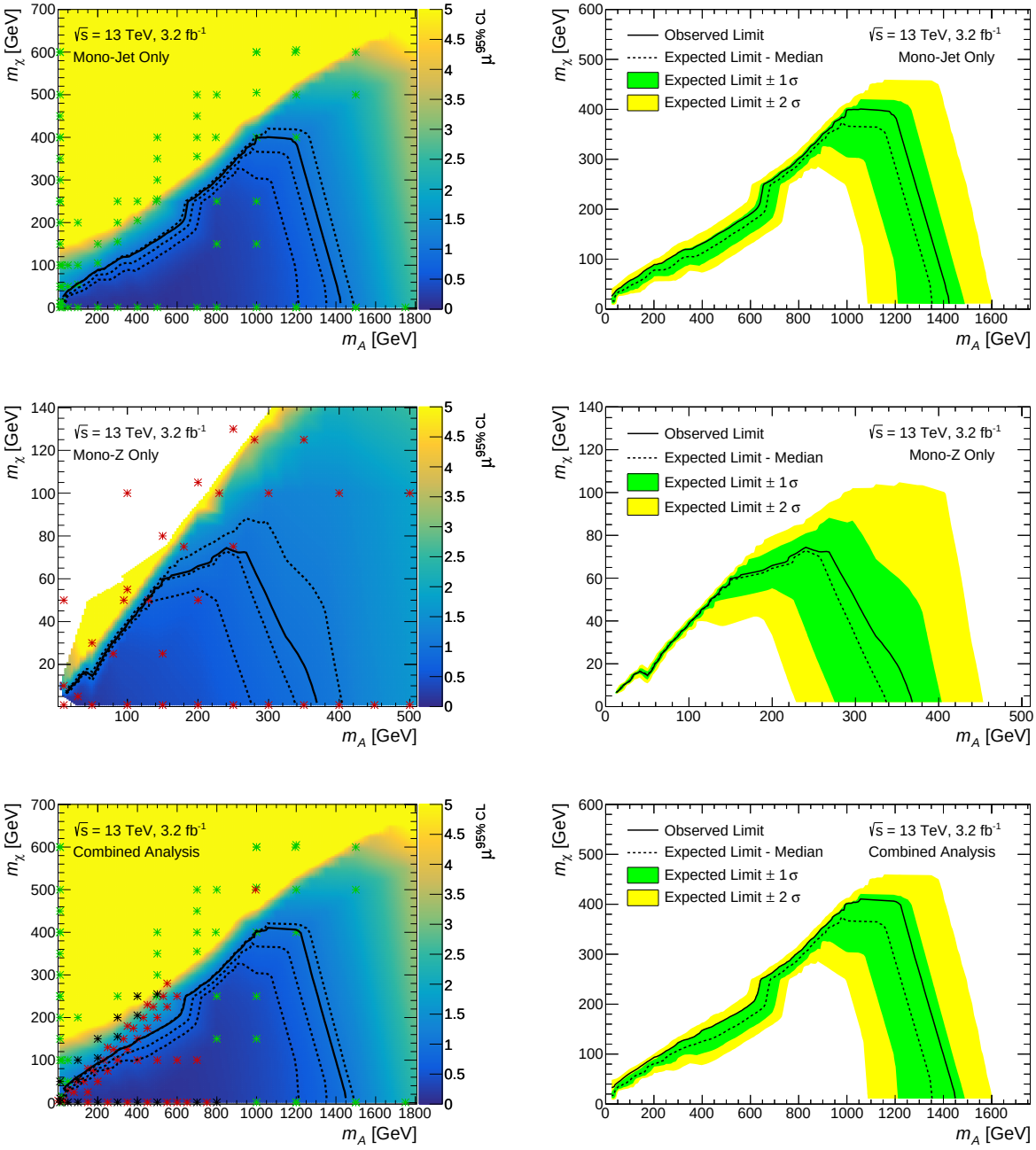

Figure 8.2: Left column: Observed $\mu^{95\%\,\mathrm{CL}}$ as a function of m_A and m_χ from the mono-jet analysis alone, the mono-Z analysis alone, and in a combined analysis. Note the different axis range in the mono-Z analysis. Indicated with green markers are the mass points at which Monte Carlo samples for the mono-jet analysis were available and between which the signal prediction was interpolated. The red markers indicate the corresponding samples used in the mono-Z analysis. Black markers indicate mass points, were samples for both signal regions were available. The white region in the mono-Z diagram corresponds to points where the signal prediction was too low to find $\mu^{95\%\,\mathrm{CL}}$ in the scan. A solid black line indicates the contour of the observed $\mu^{95\%\,\mathrm{CL}} = 1$. The dashed lines are the corresponding contours for the expected limit and the $\pm 1\sigma$ uncertainty on it.
Right column: The contours from the left column as 95 % exclusion limits on the masses of the WIMP and the axial-vector mediator for $g_q = 0.25$ and $g_\chi = 1.0$.

	upper limit on BR($h \to$ inv) [%]			
	expected	$(-1\sigma, +1\sigma)$	$(-2\sigma, +2\sigma)$	observed
mono-jet only	500	$(350, 730)$	$(250, 1060)$	310
mono-Z only	117	$(92, 153)$	$(76, 196)$	115
combined analysis	93	$(69, 128)$	$(53, 170)$	98

Table 8.1: Expected and observed upper limits on the invisible Higgs branching ratio at 95 % confidence level according to the CL_s method. Shown are the results under consideration of the mono-jet analysis alone, the mono-Z analysis alone, and all results simultaneously.

8.2.2 Invisible Higgs Decay

The procedure to derive upper limits on the branching ratio of an invisible Higgs decay is analogous to the case of the axial-vector WIMP production described in the previous section. Since the signal does not depend on any additional parameters, this evaluation does not need to be performed on a grid in a parameter space but only once.

The Monte Carlo samples used to derive the signal predictions are normalized to the Standard Model cross sections for the respective process of gluon-gluon fusion, vector-boson fusion or Higgs radiation. The produced Higgs bosons are then forced to decay invisibly, corresponding to an assumed branching ratio of BR($h \to$ inv) = 100 %. This implies that the signal strength μ can be identified as the branching ratio BR($h \to$ inv) as a value of $\mu = 1$ corresponds to the nominal prediction.

A scan of $CL_s(\mu)$ as illustrated in Figure 8.1 is performed for both analyses separately and in a combined analysis. The resulting upper limits at a 95 % confidence level are presented in Table 8.1. Although upper limits > 100 % provide no gain of physical information, they are stated to demonstrate the sensitivity of the respective analysis.

Considering only the mono-jet analysis yields the relatively weak expected limit of 500 %. The observed limit of 310 % is consistent with the expectation within 2 standard deviations. The low sensitivity is due to the low signal over background ratio in the order of 10^{-2} in this signature in combination with a $E_{\mathrm{T}}^{\mathrm{miss}}$ spectrum very similar to the background.

In the mono-Z analysis, the $E_{\mathrm{T}}^{\mathrm{miss}}$ spectrum of the signal is also similar to that of the background. But with a signal to background ratio of ≈ 0.3, it is significantly more sensitive despite the larger statistical uncertainties. This results in the stronger upper limit on the invisible branching ratio of 117 % expected and 115 % observed.

Combining both analyses provides a considerable improvement of the expected limit by ≈ 20 % in comparison to the mono-Z only result, corresponding to approximately 1 standard deviation of the expectation. This implies that the sensitivity improves by including the mono-jet results – although the latter on their own are less sensitive by a factor of ≈ 5. The effect can be understood by considering the systematic uncertainties. In the mono-Z analysis, they are only weakly constrained because of the large statistical uncertainties of the observations, such that the corresponding nuisance parameters can float around their nominal values only bound by the prior knowledge $h_k\big(\theta_k \,|\, \tilde{\theta}_k\big)$. This means that a larger set of possible observations can be brought to consistency with the prediction. The mono-jet analysis, on the other hand, offers significantly more events

in the selection, such that the statistical uncertainties become small in comparison to the systematic ones. A nuisance parameter floating within its prior probability can thus induce significant deviations between the observation and prediction, resulting in a reduced likelihood $\mathcal{L}$. This penalizes values of nuisance parameters deviating strongly from the value that creates the best agreement between the observation and prediction.

By considering the mono-jet bins in addition to the mono-Z results and correlating the nuisance parameters, the likely range of nuisance parameters is reduced in comparison to the mono-Z results alone, which improves the sensitivity. Essentially, the mono-jet signature acts as control region to fix the systematic uncertainties for the mono-Z signal region in this case. Dedicated searches for new physics on reconstruction level typically include carefully designed control regions for exactly this purpose. The potential gain in sensitivity by combining different signatures would thus decrease in such a scenario. If, however, unfolded results with detailed information on the effect of each systematic uncertainty (as in Table A.2) were published for multiple signatures, the necessity of such control regions per analysis could be reduced without a loss in sensitivity. This application relies on a correct handling of correlations of the systematic uncertainties across channels and thus favors a set of nuisance parameters as complete as possible. The minimal sets employed in this thesis and many current ATLAS searches [33, 34] entail the risk of correlating uncertainties too strongly. As several causes of an uncertainty are combined into a composite nuisance parameter, the information that different channels might be affected by different causes is lost. Instead, the composite nuisance parameter is fully correlated across them. For the presented mono-jet and mono-Z analyses, this effect is expected to be small as the considered reconstructed physics objects in both signatures are expected to be affected similarly by detector effects. However, the potential overestimation of correlations motivates additional studies on the impact of reduced sets of nuisance parameters on the combination of signatures. Ultimately, a recommended level of detail to achieve a precision suitable for a search for new physics needs to be found.

8.2.3 Heavy Higgs-Like Scalar

The last signal model under test is that of an additional heavy Higgs-like scalar H. Since the cross section ratio of the two expected production channels gluon-gluon fusion and vector-boson fusion is not fixed for H, these two processes are treated independently. The resulting limits are conservative in the sense that they apply for a scalar with gluon-gluon (or vector-boson) fusion as its only production mode and a model allowing for both would correspond to a larger signal.

Monte Carlo signal samples for masses m_H between 400 GeV and 1.4 TeV are studied such that limits can be placed in this mass range. These samples are normalized to a total H production cross section of 1 pb and let H only decay into a pair of Z bosons. An upper limit $\mu^{95\%\,\mathrm{CL}}$ on the signal strength thus corresponds to an upper limit on $\sigma(\text{ggF-}H) \times \mathrm{BR}(H \to ZZ)[\text{pb}]$, where $\sigma(\text{ggF-}H)$ denotes the total production cross section of the new scalar via gluon-gluon fusion. For the vector-boson fusion signal, this holds respectively.

Analogously to the previous sections, limits are derived under consideration of the two topologies separately and in a combined analysis. The results in dependence of the heavy

scalar's mass m_H are shown in Figure 8.3 for scalars produced via gluon-gluon fusion and in Figure A.11 for scalars produced via vector-boson fusion. As seen in Sections 6.7 and 7.7, the production mode does not have a large influence on the predicted $E_{\mathrm{T}}^{\mathrm{miss}}$ spectrum in both signatures, besides an overall scaling. This necessarily results in the exclusion limits behaving very similarly as observed such that the following statements on the ggF signal hold for the VBF signal analogously.

Considering only the mono-jet analysis, results in a limit on $\sigma(\text{ggF-}H) \times \mathrm{BR}(H \to ZZ)$ which falls with m_H. This is due to the $E_{\mathrm{T}}^{\mathrm{miss}}$ spectrum of the signal peaking at around $m_H/2$ (Figure 6.9) while the background falls exponentially with $E_{\mathrm{T}}^{\mathrm{miss}}$. Large masses thus offer an improved signal to background ratio and correspondingly an improved sensitivity. The observed limit is consistent with the expectation with respect to its uncertainty bands for all tested masses.

The mono-Z analysis yields limits with a comparably weak dependence on m_H for values $m_H \gtrsim 600\,\mathrm{GeV}$. This is caused by the different $E_{\mathrm{T}}^{\mathrm{miss}}$ binning in the mono-Z analysis where all events with $E_{\mathrm{T}}^{\mathrm{miss}} > 180\,\mathrm{GeV}$ populate the same bin. Signal models with sufficiently large m_H thus dominantly predict a contribution in this bin regardless of the exact value of m_H. Only for lower masses, a non-negligible contribution in the lower $E_{\mathrm{T}}^{\mathrm{miss}}$ bins is predicted. As these correspond to a larger Standard Model background, the sensitivity is reduced for low m_H. This dominant sensitivity by a single $E_{\mathrm{T}}^{\mathrm{miss}}$ bin is also responsible for the observed limit showing less fluctuations around the expectations than in the mono-jet analysis but instead an approximately constant offset for large m_H.

The different m_H-dependence of the limits in both analyses makes their combination especially interesting. The results are shown in Figure 8.3(c) and A.11(c), where the dashed blue and red lines indicate the expected limits of the mono-jet and mono-Z analyses alone.

For masses m_H up to 1.1 TeV, the mono-Z analysis offers the better sensitivity. Consequently, the shape of the limit as function of m_H in the combined analysis follows closely. It is, however, stronger by a factor of ≈ 2 in this region – even at the lowest tested m_H where the limit of the mono-jet analysis is weaker by two orders of magnitude. This behavior is similar to the improved sensitivity observed for the invisible Higgs decay in the previous section. Despite its low sensitivity by itself, the mono-jet signature acts as control region to fix the systematic uncertainties, resulting in an improved sensitivity of the mono-Z signature. In this case, however, the gain of the combination is much more pronounced as the limits improve by a factor of ≈ 2, which corresponds to a difference of more than 2σ of the expectation. The considerably stronger improvement than for the invisible Higgs decay can, at least partially, be attributed to the different QCD scale uncertainties on the signal predictions. These are $\approx 30\,\%$ for the $H \to ZZ$ signal as opposed to $\approx 2\,\%$ for the $Zh(\to \mathrm{inv})$ signal. The corresponding nuisance parameters, which are correlated across all background and signal processes, are strongly constrained by including the mono-jet bins. Therefore, the $H \to ZZ$ receives a stronger improvement than the $Zh(\to \mathrm{inv})$ where the QCD uncertainty is already small.

For large values of $m_H > 1.1\,\mathrm{TeV}$, the sensitivity of the mono-jet analysis surpasses that of the mono-Z analysis due to the reduced background in the higher $E_{\mathrm{T}}^{\mathrm{miss}}$ bins. Around the point of equal sensitivity of the two signatures, the improvement by the combined analysis reaches its maximum with a factor of 2.4. This corresponds to a larger statistical sample in the analysis, as more bins with sensitivity to the signal are

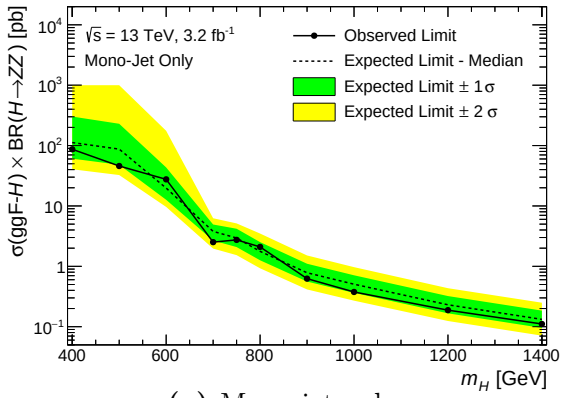

(a) Mono-jet only

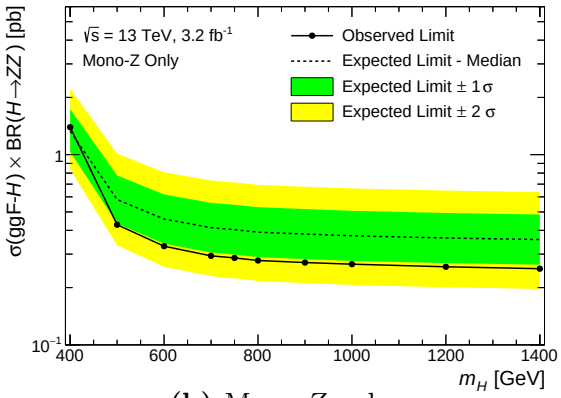

(b) Mono-Z only

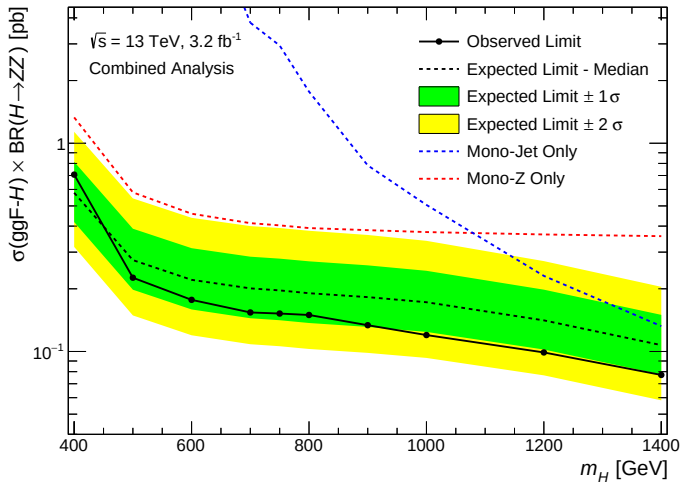

(c) Combined analysis

Figure 8.3: Expected and observed 95 % CL limits on the gluon-gluon fusion production cross section of a heavy Higgs-like scalar in dependence of its mass m_H. Shown are the results under consideration of **(a)** the mono-jet analysis alone, **(b)** the mono-Z analysis alone, and **(c)** all results simultaneously. The dashes blue and red line correspond to the expected limits from Figures **(a)** and **(b)**.

considered. Beyond this point, the shape of the combined limits starts to follow that of the mono-jet only analysis and decreases with m_H. It preserves an improved sensitivity over the mono-jet only analysis for all tested masses, but the amount of improvement decreases with m_H. This shows that the mono-Z signature does not act as control region but primarily contributes in the combination by its own sensitivity.

The observed behavior suggests that, for a specific new physics model under test, combining several signatures of comparable sensitivity can potentially provide a considerably improved sensitivity in comparison to their individual evaluation. Besides this effect, the inclusion of an insensitive signature can also be beneficial if it offers large statistics in order to constrain systematic uncertainties. As long as these are correctly correlated across signatures, no disadvantage of combining signatures arises. Instead, a potentially improved sensitivity is available with negligible additional effort.

Researchers are thus encouraged to publish results unfolded to particle level with a

full disclosure of statistical correlations and the effects of nuisance parameters. This would allow tests of any new physics models and the possibility to consider multiple, potentially sensitive signatures for these arises for free.

A similar proposition holds for results from different experiments. Although most of the experimental systematic uncertainties are independent between them, the luminosity uncertainty or theoretical cross section uncertainties can still be correlated. This reduces the possible applications as control regions, but the statistical sample size of searches can be increased in any case. If, for example, a mono-Z analysis by ATLAS and one by CMS were combined, the statistics would essentially be doubled.

Such combinations of ATLAS and CMS results are already performed, e.g. for measurements of Higgs couplings, although these are done on reconstruction level [107]. This approach is limited to signal models which are uniformly tested in both experiments. Adding the additional step of unfolding the observed distribution would provide the opportunity to repeat this for other signal models. Especially for searches where the additional small unfolding uncertainties are tolerable, as opposed to precision measurements, this approach seems promising.

9 Conclusion

A combined analysis of unfolded observations in a mono-jet and a mono-Z signature was performed to constrain models of physics beyond the Standard Model. This resulted in upper cross section limits improved by a factor of up to 2.4 as compared to the individual analysis for each signature. The strongest improvement by the combination was observed for models where the considered signatures offer similar individual sensitivity. Nonetheless, an improvement by a factor of 2 could also be gained by combining a sensitive signature with large statistical uncertainties and a signature with low or vanishing sensitivity but small statistical uncertainties as the latter helps to control systematic effects.

A combined analysis of multiple signatures relies on the correct correlation of systematic uncertainties across them. In this thesis, they were treated individually by a few nuisance parameters for the energy scale, resolution and reconstruction efficiency for each physics object and two parameters for the QCD renormalization and factorization scale. A more differentiated treatment of the individual sources of each of these uncertainties is possible, which motivates additional studies to determine the recommended level of detail.

Previous studies [41] show that cross section limits derived from unfolded distributions are consistent with those derived via the presently prevalent method including detector effects. Unfolded distributions, however, allow to reinterprete observations in terms of different models later on and to easily combine results from multiple signatures or experiments. If future searches were published with unfolded results, their correlation matrices and a detailed description of the impact of each systematic uncertainty, a significantly improved sensitivity could be reached by a combined analysis as shown in this thesis.

The presented study corresponds to the minimal use case of considering only two signatures. If more unfolded signatures become available in future publications, the potential of a combined analysis is expected to grow even further.

A Auxiliary Material

A.1 Auxiliary Figures

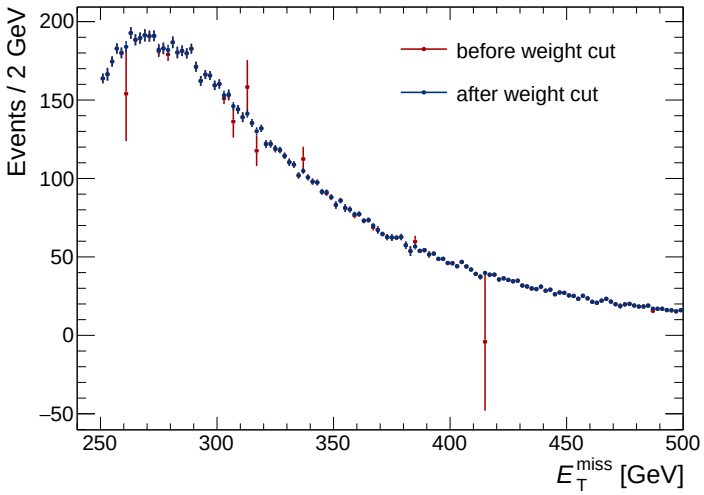

Figure A.1: Effect of the requirement that Monte Carlo event weights must not deviate by more than 100 RMS from the mean weight. Shown is the $E_{\mathrm{T}}^{\mathrm{miss}}$ distribution of the $Z \to \nu\nu$ sample in the mono-jet signal region before and after the cut is applied.

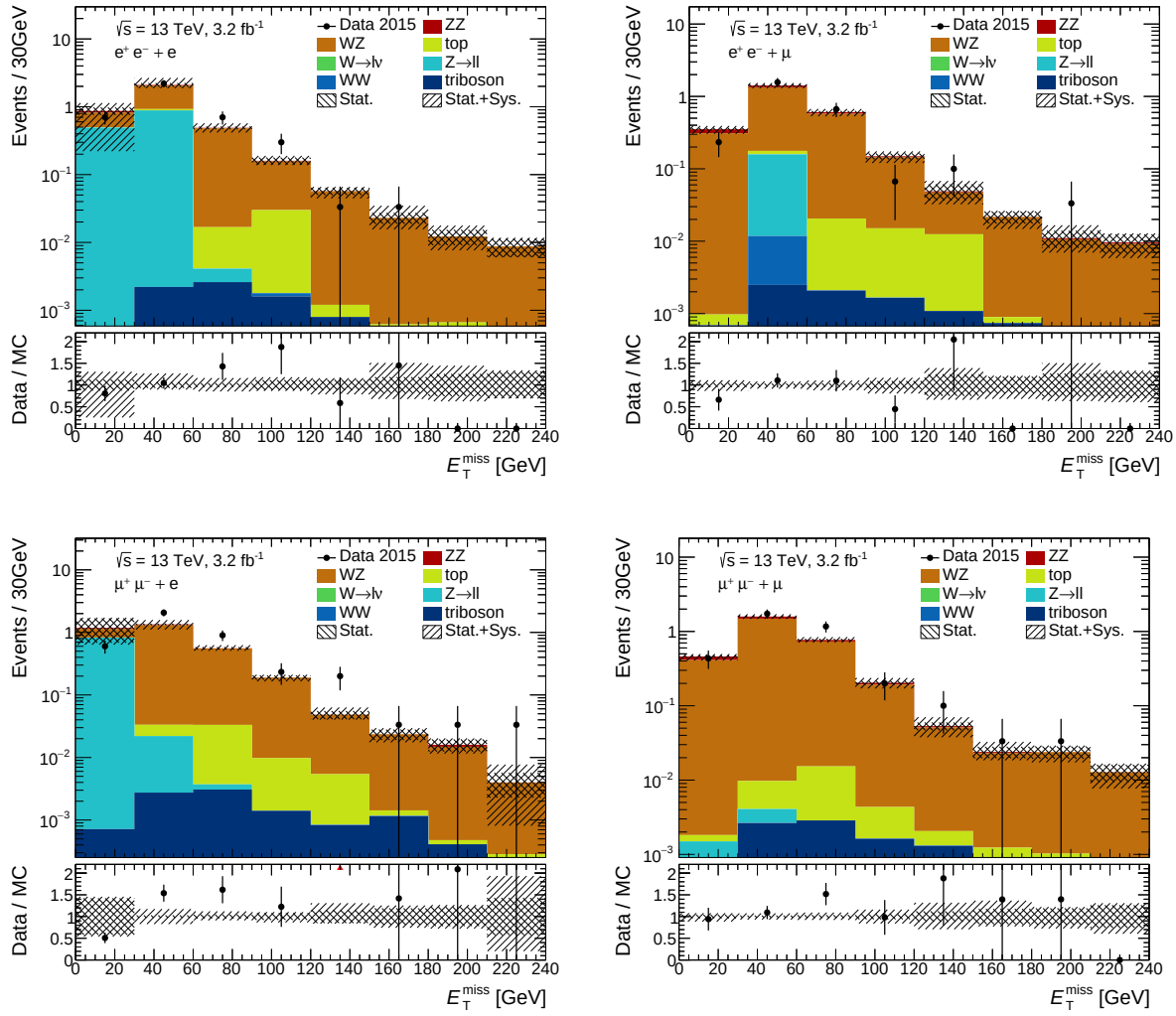

Figure A.2: Observed $E_{\mathrm{T}}^{\mathrm{miss}}$ distribution in the WZ control region compared to the Standard Model prediction, split into the four possible decay channels.

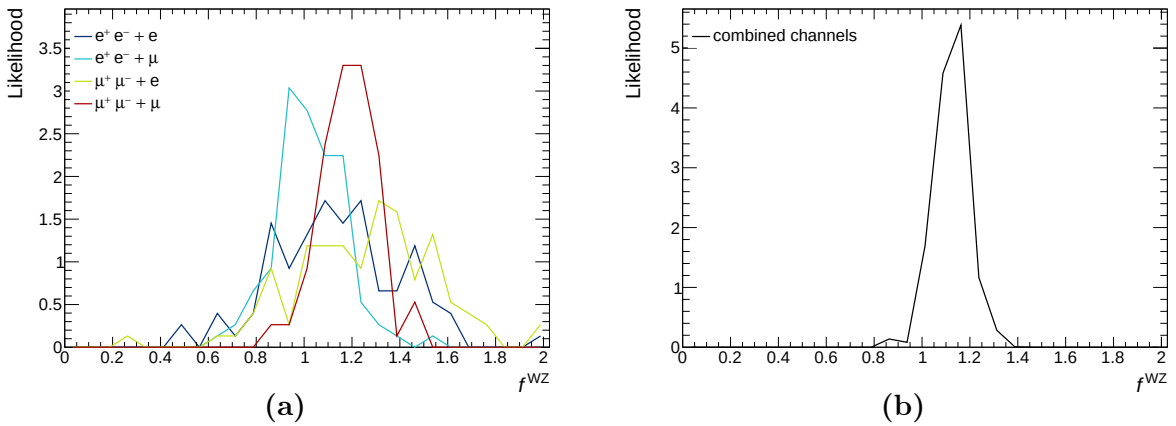

Figure A.3: Determination of the scale factor f^{WZ}. **(a)** Bootstrapped likelihood of f^{WZ} for each decay channel. **(b)** Combined likelihood from all four channels according to Equation 7.3.

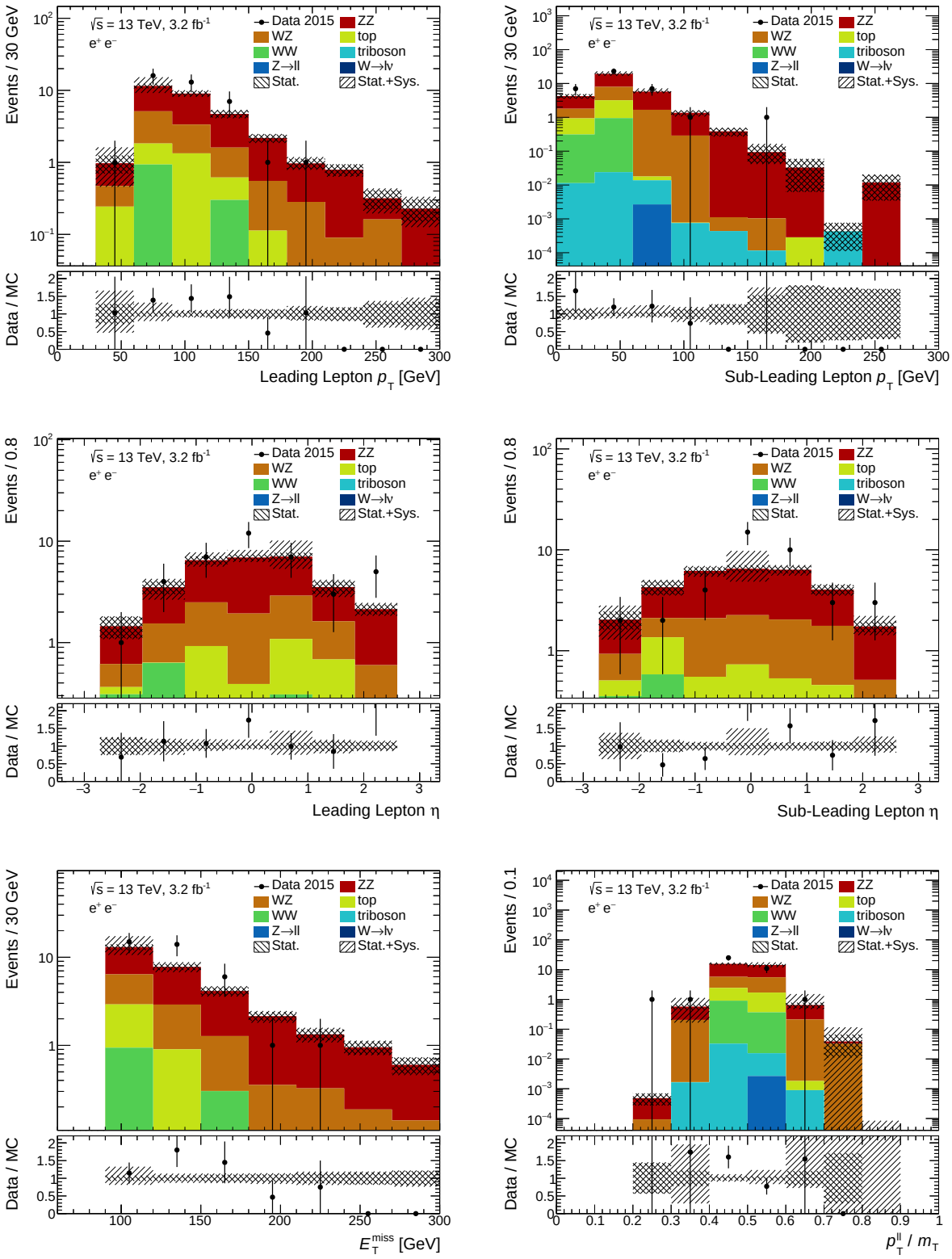

Figure A.4: Observed distributions of the leading jet's p_T and η, E_T^{miss} and, if it exists, the sub-leading jet's p_T and η in the mono-$Z(\rightarrow e^+e^-)$ signal region compared to the Standard Model prediction. The jet multiplicity refers to the set of jets with $p_T > 30\,\text{GeV}$. The uncertainty on the Standard Model prediction is the quadratic sum of the statistical component, the systematic experimental variations and QCD scale uncertainties.

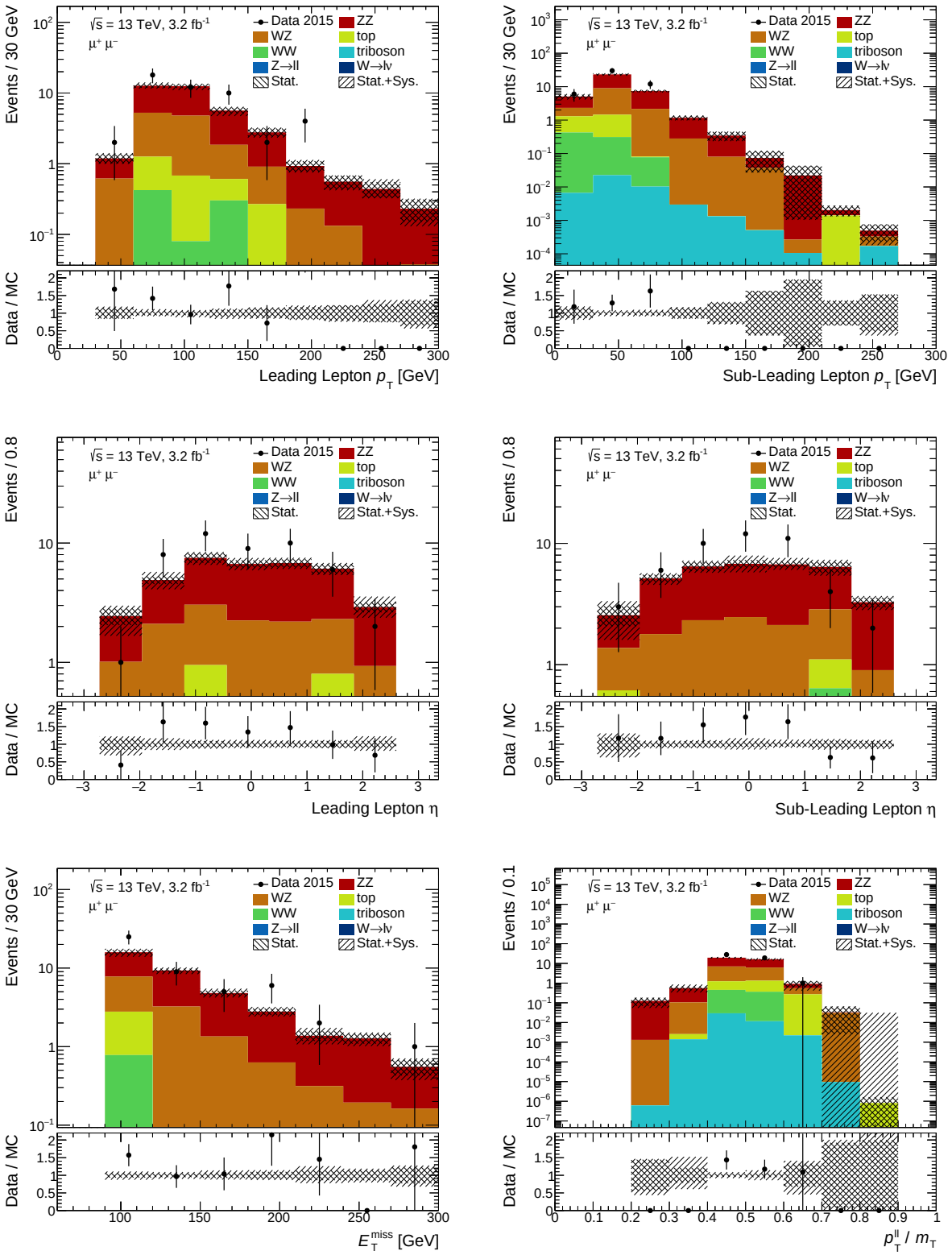

Figure A.5: Observed distributions of the leading jet's p_{T} and η, $E_{\mathrm{T}}^{\mathrm{miss}}$ and, if it exists, the sub-leading jet's p_{T} and η in the mono-$Z(\rightarrow \mu^+\mu^-)$ signal region compared to the Standard Model prediction. The jet multiplicity refers to the set of jets with $p_{\mathrm{T}} > 30\,\mathrm{GeV}$. The uncertainty on the Standard Model prediction is the quadratic sum of the statistical component, the systematic experimental variations and QCD scale uncertainties.

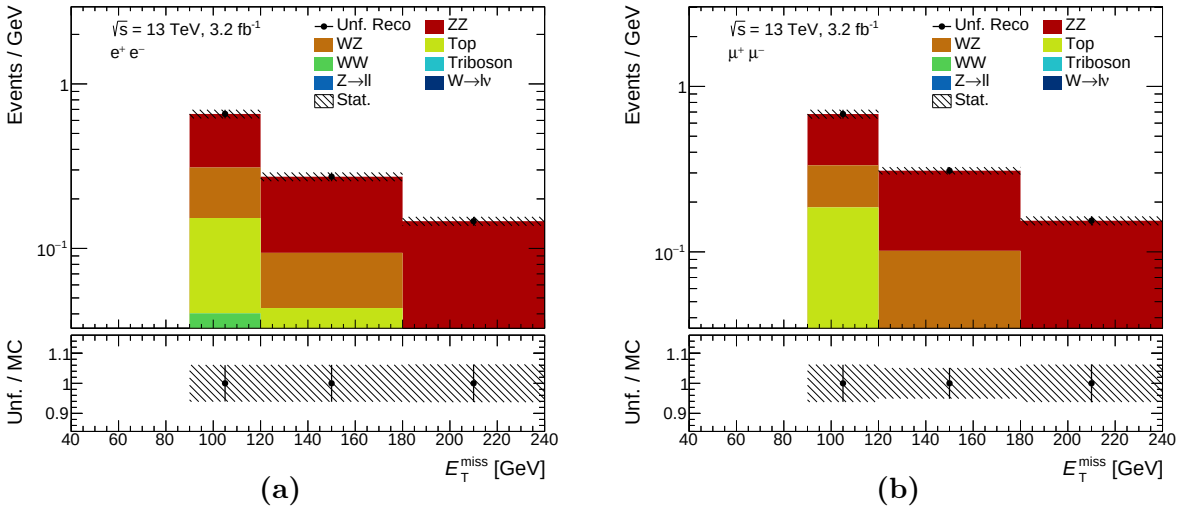

Figure A.6: Results of the closure test in the mono-Z analysis in the **(a)** e^+e^- decay channel and the **(b)** $\mu^+\mu^-$ decay channel. Shown are the Monte Carlo particle level distributions in comparison to the reconstruction level distribution unfolded with one Bayesian iteration. The error bars correspond to the statistical uncertainties only.

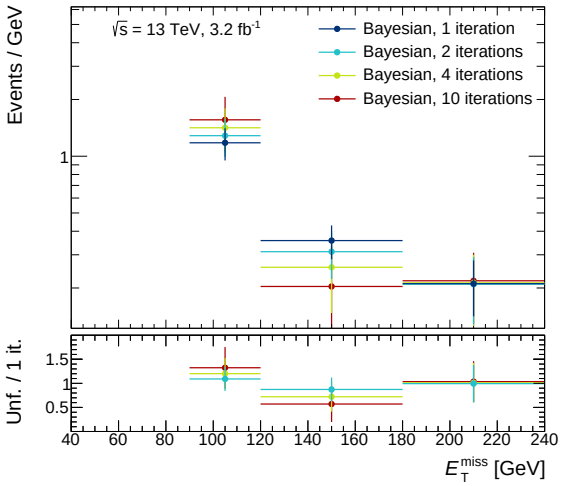

Figure A.7: Observed $E_{\mathrm{T}}^{\mathrm{miss}}$ distribution in the $\mu^+\mu^-$ channel unfolded to particle level with the Bayesian algorithm for different numbers of iterations. Indicated is only the statistical uncertainty.

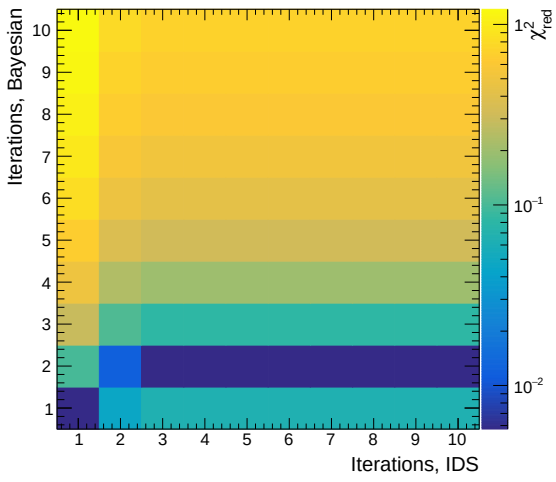

Figure A.8: χ^2_{red} as defined in Equation 6.2 between the $E_{\mathrm{T}}^{\mathrm{miss}}$ distribution in the $\mu^+\mu^-$ channel unfolded via the Bayesian and IDS algorithm for different numbers of iterations.

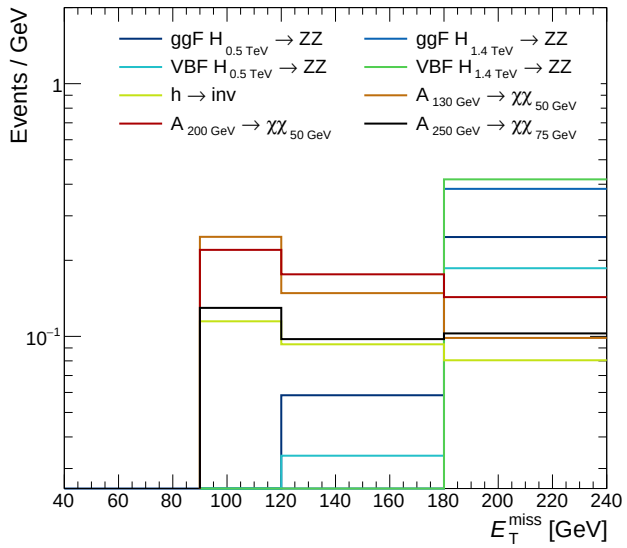

Figure A.9: Predicted $E_{\mathrm{T}}^{\mathrm{miss}}$ distributions of selected signal samples in the mono-$Z \to (\mu^+\mu^-)$ signal region. The depicted heavy Higgs-like scalar results correspond to a total production cross section of 1 pb. For the WIMP models, $g_q = 0.25$ and $g_\chi = 1$ were assumed.

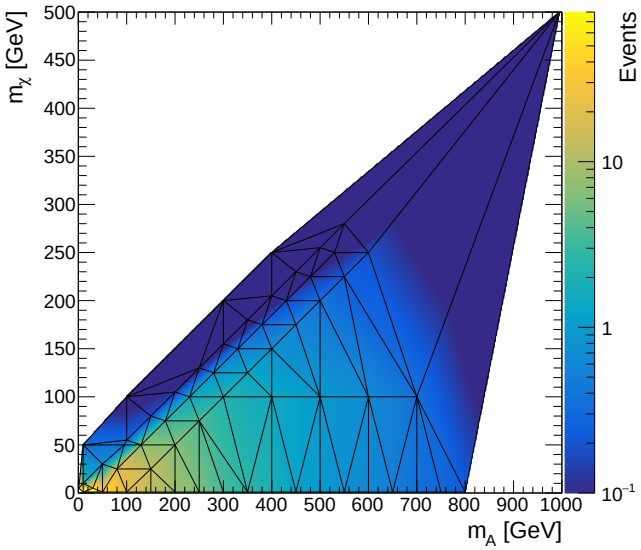

Figure A.10: Event count of the $A \to \chi\bar{\chi}$ signal in the $90\,\mathrm{GeV} < E_{\mathrm{T}}^{\mathrm{miss}} < 120\,\mathrm{GeV}$ bin of the mono-$Z \to (\mu^+\mu^-)$ signal region, interpolated across the m_A-m_χ-plane. The vertices of the indicated Delaunay triangles correspond to mass points with an available Monte Carlo signal sample to evaluate the event count. The white regions are set to zero due to a lack of information.

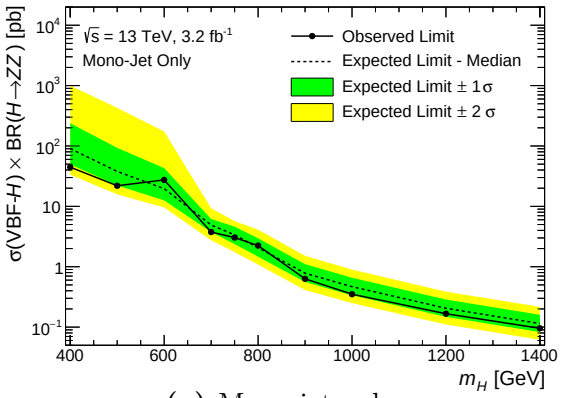

(a) Mono-jet only

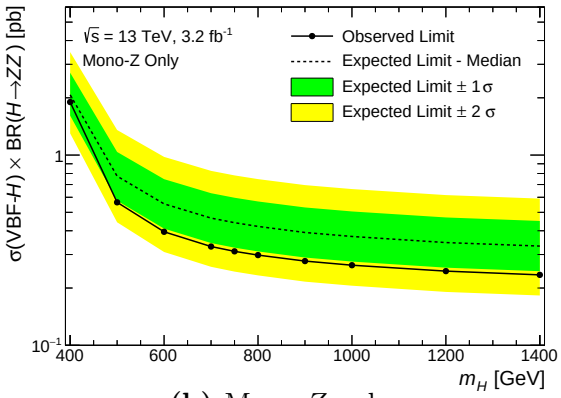

(b) Mono-Z only

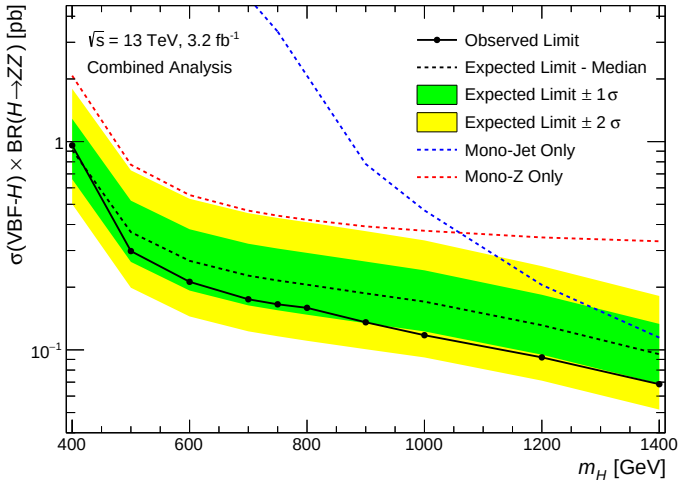

(c) Combined analysis

Figure A.11: Expected and observed 95 % CL limits on the vector-boson fusion production cross section of a heavy Higgs-like scalar in dependence of its mass m_H. Shown are the results under consideration of **(a)** the mono-jet analysis alone, **(b)** the mono-Z analysis alone, and **(c)** all results simultaneously. The dashes blue and red line correspond to the expected limits from Figures **(a)** and **(b)**.

A.2 Auxiliary Tables

$E_{\mathrm{T}}^{\mathrm{miss}}$ [GeV]	250–300	300–350	350–400	400–500
SM prediction	$8514\,^{+759}_{-648}$	$5241\,^{+486}_{-427}$	$2668\,^{+256}_{-217}$	$2168\,^{+204}_{-184}$
statistical	±0.3 %	±0.4 %	±0.4 %	±0.8 %
renormalization scale	+7.7 % −6.8 %	+7.7 % −6.8 %	+7.7 % −6.8 %	+7.7 % −6.8 %
factorization scale	+3.5 % −2.4 %	+3.5 % −2.4 %	+3.5 % −2.4 %	+3.5 % −2.4 %
JET_GroupedNP_1	+0.1 % −0.5 %	+2.6 % −2.6 %	+3.5 % −2.8 %	+3.0 % −3.6 %
JET_GroupedNP_2	+2.6 % −2.4 %	+2.4 % −2.5 %	+2.4 % −2.2 %	+2.4 % −2.4 %
JET_GroupedNP_3	+0.6 % −0.5 %	+0.5 % −0.6 %	+0.6 % −0.5 %	+0.6 % −0.7 %
JET_JER_SINGLE_NP	+0.1 % −0.1 %	+0.6 % −0.6 %	+1.0 % −1.0 %	+0.3 % −0.3 %
MET_SoftTrk_ResoPara	+0.0 % −0.0 %	+0.4 % −0.4 %	+0.4 % −0.4 %	+0.3 % −0.3 %
MET_SoftTrk_ResoPerp	+0.1 % −0.1 %	+0.3 % −0.3 %	+0.2 % −0.2 %	+0.3 % −0.3 %
MET_SoftTrk_Scale	+0.0 % −0.0 %	+0.3 % −0.4 %	+0.6 % −0.3 %	+0.3 % −0.3 %

$E_{\mathrm{T}}^{\mathrm{miss}}$ [GeV]	500–600	600–700	> 700
SM prediction	$667\,^{+64}_{-57}$	$225\,^{+22}_{-18}$	$159\,^{+16}_{-14}$
statistical	±0.6 %	±0.9 %	±1.0 %
renormalization scale	+7.7 % −6.8 %	+7.7 % −6.8 %	+7.7 % −6.8 %
factorization scale	+3.5 % −2.4 %	+3.5 % −2.4 %	+3.5 % −2.4 %
JET_GroupedNP_1	+2.9 % −3.2 %	+3.0 % −2.5 %	+3.1 % −3.1 %
JET_GroupedNP_2	+3.0 % −3.1 %	+3.2 % −2.8 %	+4.0 % −3.9 %
JET_GroupedNP_3	+0.7 % −0.7 %	+0.6 % −0.6 %	+0.5 % −0.5 %
JET_JER_SINGLE_NP	+0.1 % −0.1 %	+0.4 % −0.4 %	+0.3 % −0.3 %
MET_SoftTrk_ResoPara	+0.4 % −0.4 %	+0.2 % −0.2 %	+0.1 % −0.1 %
MET_SoftTrk_ResoPerp	+0.4 % −0.4 %	+0.2 % −0.2 %	+0.1 % −0.1 %
MET_SoftTrk_Scale	+0.2 % −0.5 %	+0.4 % −0.2 %	+0.1 % −0.2 %

Table A.1: Composition of the uncertainty on the Standard Model prediction on reconstruction level in the seven $E_{\mathrm{T}}^{\mathrm{miss}}$ bins of the mono-jet signal region. Components with an effect of $< 0.1\,\%$ are omitted. The total stated uncertainty in each bin is the quadratic sum of all components.

$E_{\mathrm{T}}^{\mathrm{miss}}$ [GeV]	250–300	300–350	350–400	400–500
observed events (unfolded)	$12332\,^{+355}_{-363}$	$6928\,^{+282}_{-265}$	$3636\,^{+160}_{-177}$	$2902\,^{+152}_{-135}$
statistical	±1.1 %	±1.4 %	±2.1 %	±2.3 %
`JET_GroupedNP_1`	$^{+0.7\,\%}_{-0.6\,\%}$	$^{+2.6\,\%}_{-2.5\,\%}$	$^{+2.9\,\%}_{-3.5\,\%}$	$^{+3.9\,\%}_{-3.1\,\%}$
`JET_GroupedNP_2`	$^{+2.5\,\%}_{-2.6\,\%}$	$^{+2.6\,\%}_{-2.4\,\%}$	$^{+2.3\,\%}_{-2.3\,\%}$	$^{+2.5\,\%}_{-2.4\,\%}$
`JET_GroupedNP_3`	$^{+0.5\,\%}_{-0.6\,\%}$	$^{+0.6\,\%}_{-0.5\,\%}$	$^{+0.5\,\%}_{-0.6\,\%}$	$^{+0.7\,\%}_{-0.6\,\%}$
`JET_JER_SINGLE_NP`	$^{+0.1\,\%}_{-0.1\,\%}$	$^{+0.5\,\%}_{-0.5\,\%}$	$^{+1.0\,\%}_{-1.0\,\%}$	$^{+0.4\,\%}_{-0.4\,\%}$
`MET_SoftTrk_ResoPara`	$^{+0.0\,\%}_{-0.0\,\%}$	$^{+0.4\,\%}_{-0.4\,\%}$	$^{+0.4\,\%}_{-0.4\,\%}$	$^{+0.3\,\%}_{-0.3\,\%}$
`MET_SoftTrk_ResoPerp`	$^{+0.1\,\%}_{-0.1\,\%}$	$^{+0.3\,\%}_{-0.3\,\%}$	$^{+0.3\,\%}_{-0.3\,\%}$	$^{+0.3\,\%}_{-0.3\,\%}$
`MET_SoftTrk_Scale`	$^{+0.0\,\%}_{-0.1\,\%}$	$^{+0.3\,\%}_{-0.3\,\%}$	$^{+0.3\,\%}_{-0.6\,\%}$	$^{+0.3\,\%}_{-0.3\,\%}$

$E_{\mathrm{T}}^{\mathrm{miss}}$ [GeV]	500–600	600–700	> 700
observed events (unfolded)	$894\,^{+58}_{-54}$	$294\,^{+24}_{-25}$	$228\,^{+23}_{-23}$
statistical	±4.3 %	±7.0 %	±8.6 %
`JET_GroupedNP_1`	$^{+3.4\,\%}_{-3.0\,\%}$	$^{+2.8\,\%}_{-3.3\,\%}$	$^{+3.1\,\%}_{-3.0\,\%}$
`JET_GroupedNP_2`	$^{+3.3\,\%}_{-3.0\,\%}$	$^{+3.1\,\%}_{-3.3\,\%}$	$^{+4.0\,\%}_{-3.9\,\%}$
`JET_GroupedNP_3`	$^{+0.7\,\%}_{-0.7\,\%}$	$^{+0.6\,\%}_{-0.6\,\%}$	$^{+0.4\,\%}_{-0.5\,\%}$
`JET_JER_SINGLE_NP`	$^{+0.1\,\%}_{-0.1\,\%}$	$^{+0.4\,\%}_{-0.4\,\%}$	$^{+0.2\,\%}_{-0.2\,\%}$
`MET_SoftTrk_ResoPara`	$^{+0.4\,\%}_{-0.4\,\%}$	$^{+0.2\,\%}_{-0.2\,\%}$	$^{+0.1\,\%}_{-0.1\,\%}$
`MET_SoftTrk_ResoPerp`	$^{+0.5\,\%}_{-0.5\,\%}$	$^{+0.3\,\%}_{-0.3\,\%}$	$^{+0.1\,\%}_{-0.1\,\%}$
`MET_SoftTrk_Scale`	$^{+0.5\,\%}_{-0.2\,\%}$	$^{+0.2\,\%}_{-0.4\,\%}$	$^{+0.2\,\%}_{-0.1\,\%}$

Table A.2: Composition of the uncertainty on the unfolded observation in the seven $E_{\mathrm{T}}^{\mathrm{miss}}$ bins of the mono-jet signal region. Components with an effect of $< 0.1\,\%$ are omitted. The QCD scale uncertainties are not propagated to the unfolded result but applied to the particle level Monte Carlo prediction instead. The total stated uncertainty in each bin is the quadratic sum of all components.

HLT trigger	HLT criteria	Level-1 seed	seed criteria
`mu20_iloose`	muon with $E_{\mathrm{T}} > 20\,\mathrm{GeV}$, loose isolation	`L1_MU15`	muon with $E_{\mathrm{T}} > 15\,\mathrm{GeV}$
`mu50`	muon with $E_{\mathrm{T}} > 50\,\mathrm{GeV}$	`L1_MU20`	muon with $E_{\mathrm{T}} > 20\,\mathrm{GeV}$
`e24_lhmedium`	electron with $E_{\mathrm{T}} > 24\,\mathrm{GeV}$, medium likelihood	`L1_EM20VH`	EM cluster with $E_{\mathrm{T}} > 20\,\mathrm{GeV}$, threshold variable along η, veto on Had layer
`e60_lhmedium`	electron with $E_{\mathrm{T}} > 60\,\mathrm{GeV}$, medium likelihood	`L1_EM22VHI`	EM cluster with $E_{\mathrm{T}} > 22\,\mathrm{GeV}$, threshold variable along η, veto on Had layer and isolation in EM layer
`e120_lhloose`	electron with $E_{\mathrm{T}} > 120\,\mathrm{GeV}$, loose likelihood	`L1_EM22VHI`	EM cluster with $E_{\mathrm{T}} > 22\,\mathrm{GeV}$, threshold variable along η, veto on Had layer and isolation in EM layer

Table A.3: List of triggers for the event selection of the mono-Z analysis. Given are the HLT trigger requirements as well as the seeding Level-1 trigger with its respective requirement.

$E_{\mathrm{T}}^{\mathrm{miss}}$ [GeV]	90–120	120–180	> 180
SM prediction, e^+e^-	$13.0\,^{+4.3}_{-2.4}$	$11.9\,^{+1.4}_{-1.3}$	$6.1\,^{+0.7}_{-0.6}$
statistical	±7.7 %	±6.3 %	±6.6 %
renormalization scale	+5.8 % −4.8 %	+5.8 % −4.8 %	+5.8 % −4.8 %
factorization scale	+0.3 % −0.5 %	+0.3 % −0.5 %	+0.3 % −0.5 %
JET_GroupedNP_1	+13.5 % − 1.4 %	+2.9 % −0.3 %	+2.4 % −1.7 %
JET_GroupedNP_2	+0.4 % −0.3 %	+0.3 % −0.0 %	+0.6 % −0.0 %
JET_GroupedNP_3	+0.4 % −0.0 %	+0.0 % −0.4 %	+0.1 % −0.0 %
JET_JER_SINGLE_NP	+27.5 % −13.7 %	+0.4 % −0.2 %	+0.7 % −0.3 %
MET_SoftTrk_ResoPara	+7.3 % −7.3 %	+3.6 % −3.6 %	+0.6 % −0.6 %
MET_SoftTrk_ResoPerp	+0.8 % −0.8 %	+2.0 % −2.0 %	+0.5 % −0.5 %
MET_SoftTrk_Scale	+0.2 % −0.3 %	+1.5 % −0.0 %	+0.5 % −1.4 %
EG_SCALE_ALL	+2.3 % −2.3 %	+3.0 % −3.0 %	+0.9 % −0.9 %
EG_RESOLUTION_ALL	+2.5 % −2.5 %	+2.0 % −2.0 %	+0.9 % −0.9 %
EL_EFF_Reco_TOTAL	+2.0 % −2.0 %	+2.6 % −2.6 %	+3.1 % −3.1 %
EL_EFF_ID_TOTAL	+2.9 % −2.9 %	+3.6 % −3.6 %	+4.5 % −4.5 %
SM prediction, $\mu^+\mu^-$	$15.9\,^{+1.7}_{-2.0}$	$14.1\,^{+1.2}_{-1.1}$	$7.3\,^{+0.7}_{-0.7}$
statistical	±6.6 %	±4.3 %	±6.3 %
renormalization scale	+5.8 % −4.8 %	+5.8 % −4.8 %	+5.8 % −4.8 %
factorization scale	+0.3 % −0.5 %	+0.3 % −0.5 %	+0.3 % −0.5 %
JET_GroupedNP_1	+4.7 % −8.2 %	+4.0 % −3.9 %	+1.1 % −2.0 %
JET_GroupedNP_2	+0.2 % −2.8 %	+0.2 % −0.3 %	+0.4 % −0.2 %
JET_GroupedNP_3	+0.0 % −0.5 %	+0.4 % −0.6 %	+0.4 % −0.0 %
JET_JER_SINGLE_NP	+2.5 % −2.5 %	+1.6 % −1.6 %	+3.8 % −3.8 %
MET_SoftTrk_ResoPara	+1.4 % −1.4 %	+1.3 % −1.3 %	+1.7 % −1.7 %
MET_SoftTrk_ResoPerp	+0.1 % −0.1 %	+1.1 % −1.1 %	+0.2 % −0.2 %
MET_SoftTrk_Scale	+0.2 % −1.5 %	+0.0 % −0.4 %	+2.1 % −0.1 %
MUON_ID	+1.7 % −0.0 %	+0.3 % −0.3 %	+1.3 % −0.6 %
MUON_MS	+0.0 % −1.2 %	+0.5 % −0.1 %	+1.2 % −0.3 %
MUON_SCALE	+0.0 % −0.3 %	+0.5 % −0.0 %	+0.1 % −0.0 %
MUON_EFF_STAT	+0.5 % −0.5 %	+0.5 % −0.5 %	+0.5 % −0.5 %
MUON_EFF_SYS	+0.9 % −0.9 %	+1.0 % −1.0 %	+1.5 % −1.5 %

Table A.4: Composition of the uncertainty on the Standard Model prediction on reconstruction level in the three $E_{\mathrm{T}}^{\mathrm{miss}}$ bins of both decay channels of the mono-Z signal region. Components with an effect of $< 0.1\,\%$ are omitted. The total stated uncertainty in each bin is the quadratic sum of all components.

$E_{\mathrm{T}}^{\mathrm{miss}}$ [GeV]	90–120	120–180	> 180
observed events (unfolded)	$22.6\,^{+8.3}_{-7.5}$	$27.2\,^{+6.6}_{-6.6}$	$5.8\,^{+2.9}_{-2.9}$
statistical	±27.3 %	±23.1 %	±50.2 %
JET_GroupedNP_1	+ 1.3 % −11.8 %	+0.4 % −2.7 %	+3.5 % −3.4 %
JET_GroupedNP_2	+0.3 % −0.4 %	+0.0 % −0.4 %	+0.0 % −0.4 %
JET_GroupedNP_3	+0.0 % −0.4 %	+0.4 % −0.1 %	+0.0 % −0.0 %
JET_JER_SINGLE_NP	+22.6 % −11.3 %	+0.6 % −0.3 %	+1.2 % −0.6 %
MET_SoftTrk_ResoPara	+8.4 % −8.4 %	+3.3 % −3.3 %	+0.8 % −0.8 %
MET_SoftTrk_ResoPerp	+0.7 % −0.7 %	+2.0 % −2.0 %	+0.3 % −0.3 %
MET_SoftTrk_Scale	+0.3 % −0.1 %	+0.0 % −1.5 %	+1.2 % −0.4 %
EG_SCALE_ALL	+2.4 % −2.4 %	+3.2 % −3.2 %	+0.1 % −0.1 %
EG_RESOLUTION_ALL	+2.6 % −2.6 %	+2.1 % −2.1 %	+0.7 % −0.7 %
EL_EFF_Reco_TOTAL_1NPCOR_PLUS_UNCOR	+2.1 % −2.1 %	+2.7 % −2.7 %	+3.2 % −3.2 %
EL_EFF_ID_TOTAL_1NPCOR_PLUS_UNCOR	+2.9 % −2.9 %	+3.8 % −3.8 %	+4.7 % −4.7 %
observed events (unfolded)	$33.3\,^{+8.4}_{-7.8}$	$18.7\,^{+4.9}_{-4.9}$	$11.5\,^{+3.8}_{-3.8}$
statistical	±22.5 %	±25.6 %	±32.6 %
JET_GroupedNP_1	+10.3 % − 5.3 %	+4.2 % −3.8 %	+2.5 % −1.6 %
JET_GroupedNP_2	+3.0 % −0.3 %	+0.3 % −0.1 %	+0.2 % −0.2 %
JET_GroupedNP_3	+0.4 % −0.0 %	+0.5 % −0.4 %	+0.0 % −0.4 %
JET_JER_SINGLE_NP	+2.8 % −2.8 %	+1.6 % −1.6 %	+3.4 % −3.4 %
MET_SoftTrk_ResoPara	+1.4 % −1.4 %	+1.4 % −1.4 %	+1.4 % −1.4 %
MET_SoftTrk_ResoPerp	+0.0 % −0.0 %	+1.2 % −1.2 %	+0.2 % −0.2 %
MET_SoftTrk_Scale	+1.9 % −0.3 %	+0.5 % −0.0 %	+0.1 % −1.9 %
MUON_ID	+0.0 % −1.8 %	+0.4 % −0.4 %	+0.5 % −1.2 %
MUON_MS	+1.5 % −0.0 %	+0.1 % −0.4 %	+0.3 % −1.0 %
MUON_SCALE	+0.5 % −0.0 %	+0.0 % −0.3 %	+0.0 % −0.1 %
MUON_EFF_STAT	+0.5 % −0.5 %	+0.5 % −0.5 %	+0.5 % −0.5 %
MUON_EFF_SYS	+0.9 % −0.9 %	+1.0 % −1.0 %	+1.5 % −1.4 %
MUON_EFF_STAT_LOWPT	+0.0 % −0.0 %	+0.0 % −0.0 %	+0.0 % −0.0 %
MUON_EFF_SYS_LOWPT	+0.0 % −0.0 %	+0.0 % −0.0 %	+0.0 % −0.0 %

Table A.5: Composition of the uncertainty on the unfolded observation in the three $E_{\mathrm{T}}^{\mathrm{miss}}$ bins of the mono-Z signal region in both decay channels. Components with an effect of $< 0.1\,\%$ are omitted. The QCD scale uncertainties are not propagated to the unfolded result but applied to the particle level Monte Carlo prediction instead. The total stated uncertainty in each bin is the quadratic sum of all components.

B Lists

B.1 List of Figures

B.2 List of Tables

C Bibliography

[1] M. Thomson. *Modern particle physics*. Cambridge University Press, New York, 2013. ISBN 9781107034266.

[2] A. Pich. The Standard model of electroweak interactions. In *The Standard model of electroweak interactions*, pages 1–49, 2008. https://inspirehep.net/record/751686.

[3] S. L. Glashow. The renormalizability of vector meson interactions. *Nucl. Phys.*, 10:107–117, 1959. doi:10.1016/0029-5582(59)90196-8.

[4] A. Salam and J. C. Ward. Weak and electromagnetic interactions. *Il Nuovo Cimento (1955-1965)*, 11(4):568–577, Feb 1959. ISSN 1827-6121. doi:10.1007/BF02726525.

[5] S. Weinberg. A Model of Leptons. *Phys. Rev. Lett.*, 19:1264–1266, 1967. doi:10.1103/PhysRevLett.19.1264.

[6] H. D. Politzer. Reliable Perturbative Results for Strong Interactions? *Phys. Rev. Lett.*, 30:1346–1349, 1973. doi:10.1103/PhysRevLett.30.1346.

[7] D. J. Gross and F. Wilczek. Ultraviolet Behavior of Nonabelian Gauge Theories. *Phys. Rev. Lett.*, 30:1343–1346, 1973. doi:10.1103/PhysRevLett.30.1343.

[8] Wikipedia. Standard model — Wikipedia, the free encyclopedia, 2004. https://commons.wikimedia.org/wiki/File:Elementary_particle_interactions_in_the_Standard_Model.png. [Accessed: 2017-11-09].

[9] J. C. Collins et al. Factorization of Hard Processes in QCD. *Adv. Ser. Direct. High Energy Phys.*, 5:1–91, 1989. doi:10.1142/9789814503266_0001.

[10] G. 't Hooft and M. J. G. Veltman. One loop divergencies in the theory of gravitation. *Ann. Inst. H. Poincare Phys. Theor.*, A20:69–94, 1974. http://www.numdam.org/item?id=AIHPA_1974__20_1_69_0.

[11] M. H. Goroff and A. Sagnotti. The ultraviolet behavior of Einstein gravity. *Nuclear Physics B*, 266(3):709 – 736, 1986. ISSN 0550-3213. doi:10.1016/0550-3213(86)90193-8.

[12] J. Polchinski. *String Theory*, volume 1 of *Cambridge Monographs on Mathematical Physics*. Cambridge University Press, 1998. doi:10.1017/CBO9780511816079.

[13] C. Rovelli. Loop Quantum Gravity. *Living Reviews in Relativity*, 1(1):1, Jan 1998. ISSN 1433-8351. doi:10.12942/lrr-1998-1.

[14] N. Arkani–Hamed et al. The hierarchy problem and new dimensions at a millimeter. *Physics Letters B*, 429(3):263 – 272, 1998. ISSN 0370-2693. doi:10.1016/S0370-2693(98)00466-3.

[15] A. D. Sakharov. Violation of CP Invariance, c Asymmetry, and Baryon Asymmetry of the Universe. *Pisma Zh. Eksp. Teor. Fiz.*, 5:32–35, 1967. doi:10.1070/PU1991v034n05ABEH002497.

[16] The Dune Collaboration. Long-Baseline Neutrino Facility (LBNF) and Deep Underground Neutrino Experiment (DUNE). 2016. https://arxiv.org/abs/1601.02984.

[17] V. C. Rubin and W. K. Ford, Jr. Rotation of the Andromeda Nebula from a Spectroscopic Survey of Emission Regions. *Astrophysical Journal*, 159:379, February 1970. doi:10.1086/150317.

[18] E. Corbelli and P. Salucci. The extended rotation curve and the dark matter halo of M33. *Monthly Notices of the Royal Astronomical Society*, 311(2):441–447, 2000. doi:10.1046/j.1365-8711.2000.03075.x.

[19] M. Bartelmann and P. Schneider. Weak gravitational lensing. *Phys. Rept.*, 340: 291–472, January 2001. doi:10.1016/S0370-1573(00)00082-X.

[20] C. Chang et al. Dark Energy Survey Year 1 Results: Curved-Sky Weak Lensing Mass Map. *ArXiv e-prints*, August 2017. https://arxiv.org/abs/1708.01535.

[21] D. Clowe et al. Weak-Lensing Mass Reconstruction of the Interacting Cluster 1E 0657–558: Direct Evidence for the Existence of Dark Matter. *The Astrophysical Journal*, 604(2):596, 2004. doi:https://arxiv.org/abs/1708.01535. http://stacks.iop.org/0004-637X/604/i=2/a=596.

[22] The Planck Collaboration. Planck 2015 results. XIII. Cosmological parameters. *Astronomy and Astrophysics*, 594:A13, September 2016. doi:10.1051/0004-6361/201525830.

[23] O. Buchmueller et al. Characterising dark matter searches at colliders and direct detection experiments: vector mediators. *Journal of High Energy Physics*, 2015(1): 37, Jan 2015. ISSN 1029-8479. doi:10.1007/JHEP01(2015)037.

[24] J. M. Cline et al. Update on scalar singlet dark matter. *Phys. Rev.*, D88:055025, 2013. doi:10.1103/PhysRevD.92.039906, 10.1103/PhysRevD.88.055025. [Erratum: Phys. Rev.D92,no.3,039906(2015)].

[25] D. de Florian et al. Handbook of LHC Higgs Cross Sections: 4. Deciphering the Nature of the Higgs Sector. 2016. doi:10.23731/CYRM-2017-002.

[26] The ATLAS Collaboration. Constraints on new phenomena via Higgs boson couplings and invisible decays with the ATLAS detector. *JHEP*, 11:206, 2015. doi:10.1007/JHEP11(2015)206.

[27] N. F. Bell et al. Self-consistent Dark Matter Simplified Models with an s-channel scalar mediator. *JCAP*, 1703(03):015, 2017. doi:10.1088/1475-7516/2017/03/015.

[28] A. Hill and J. J. van der Bij. Strongly interacting singlet-doublet Higgs model. *Phys. Rev. D*, 36:3463–3473, Dec 1987. doi:10.1103/PhysRevD.36.3463.

[29] M. Bauer et al. Simplified dark matter models with two Higgs doublets: I. Pseudoscalar mediators. *JHEP*, 05:138, 2017. doi:10.1007/JHEP05(2017)138.

[30] The ATLAS Collaboration. Search for new phenomena with photon+jet events in proton-proton collisions at $\sqrt{s} = 13$ TeV with the ATLAS detector. *JHEP*, 03:041, 2016. doi:10.1007/JHEP03(2016)041.

[31] The ATLAS Collaboration. Search for Dark Matter Produced in Association with a Higgs Boson Decaying to $b\bar{b}$ using 36 fb^{-1} of pp collisions at $\sqrt{s} = 13$ TeV with the ATLAS Detector. *Phys. Rev. Lett.*, 119(18):181804, 2017. doi:10.1103/PhysRevLett.119.181804.

[32] The ATLAS Collaboration. Search for dark matter produced in association with a hadronically decaying vector boson in pp collisions at $\sqrt{s} = 13$ TeV with the ATLAS detector. *Phys. Lett.*, B763:251–268, 2016. doi:10.1016/j.physletb.2016.10.042.

[33] The ATLAS Collaboration. Search for an invisibly decaying Higgs boson or dark matter candidates produced in association with a Z boson in pp collisions at $\sqrt{s} = 13$ TeV with the ATLAS detector. *Phys. Lett.*, B776:318–337, 2018. doi:10.1016/j.physletb.2017.11.049.

[34] The ATLAS Collaboration. Search for new phenomena in final states with an energetic jet and large missing transverse momentum in pp collisions at $\sqrt{s} = 13$ TeV using the ATLAS detector. *Phys. Rev. D*, 94:032005, Aug 2016. doi:10.1103/PhysRevD.94.032005.

[35] J. de Favereau et al. DELPHES 3: a modular framework for fast simulation of a generic collider experiment. *Journal of High Energy Physics*, 2014(2):57, Feb 2014. ISSN 1029-8479. doi:10.1007/JHEP02(2014)057.

[36] D. Alves et al. Simplified models for LHC new physics searches, journal=Journal of Physics G: Nuclear and Particle Physics. 39(10):105005, 2012. doi:10.1088/0954-3899/39/10/105005.

[37] G. D'Agostini. A Multidimensional unfolding method based on Bayes' theorem. *Nucl. Instrum. Meth.*, A362:487–498, 1995. doi:10.1016/0168-9002(95)00274-X.

[38] B. Malaescu. An Iterative, dynamically stabilized method of data unfolding. 2009. https://arxiv.org/abs/0907.3791.

[39] B. Malaescu. private communication.

[40] B. Efron. Bootstrap Methods: Another Look at the Jackknife. *Ann. Statist.*, 7(1): 1–26, 01 1979. doi:10.1214/aos/1176344552.

[41] B. Bernarding. Towards Unfolding Topologies Proof of Concept within a Monojet Analysis. Master's thesis, Ruprecht-Karls-Universität Heidelberg, 2016. https://www.kip.uni-heidelberg.de/Veroeffentlichungen/details.php?id=3475.

[42] J.-L. Caron. The LHC injection complex.. L'ensemble d'injection du LHC. AC Collection. Legacy of AC. Pictures from 1992 to 2002., May 1993. https://cds.cern.ch/record/841568.

[43] The Large Electron-Positron Collider. https://home.cern/about/accelerators/large-electron-positron-collider. Accessed: 2017-10-24.

[44] A. Hofmann. I. Synchrotron radiation from the large electron-positron storage ring LEP. *Physics Reports*, 64(5):253 – 281, 1980. ISSN 0370-1573. doi:10.1016/0370-1573(80)90135-0.

[45] L. Evans and P. Bryant. LHC Machine. *Journal of Instrumentation*, 3(08):S08001, 2008. doi:10.1088/1748-0221/3/08/S08001.

[46] ATLAS Public Luminosity Results. https://twiki.cern.ch/twiki/bin/view/AtlasPublic/LuminosityPublicResultsRun2. Accessed: 2017-10-25.

[47] The ATLAS Collaboration et al. The ATLAS Experiment at the CERN Large Hadron Collider. *Journal of Instrumentation*, 3(08):S08003, 2008. doi:10.1088/1748-0221/3/08/S08003.

[48] The CMS Collaboration et al. The CMS experiment at the CERN LHC. *Journal of Instrumentation*, 3(08):S08004, 2008. doi:10.1088/1748-0221/3/08/S08004.

[49] The ALICE Collaboration et al. The ALICE experiment at the CERN LHC. *Journal of Instrumentation*, 3(08):S08002, 2008. doi:10.1088/1748-0221/3/08/S08002.

[50] The LHCb Collaboration et al. The LHCb Detector at the LHC. *Journal of Instrumentation*, 3(08):S08005, 2008. doi:10.1088/1748-0221/3/08/S08005.

[51] The ATLAS Collaboration. ATLAS Insertable B-Layer Technical Design Report. Technical Report CERN-LHCC-2010-013. ATLAS-TDR-19, CERN, Sep 2010. http://cds.cern.ch/record/1291633.

[52] K. Kleinknecht. *Detectors for Particle Radiation*. Cambridge University Press, 1998. ISBN 9780521648547.

[53] The ATLAS Collaboration. Vertex Reconstruction Performance of the ATLAS Detector at $sqrts = 13$ TeV. Technical Report ATL-PHYS-PUB-2015-026, CERN, Geneva, Jul 2015. https://cds.cern.ch/record/2037717.

[54] The ATLAS Collaboration. The ATLAS Inner Detector commissioning and calibration. *The European Physical Journal C*, 70(3):787–821, Dec 2010. ISSN 1434-6052. doi:10.1140/epjc/s10052-010-1366-7.

[55] C. Patrignani et al. Review of Particle Physics. *Chin. Phys.*, C40(10):100001, 2016. doi:10.1088/1674-1137/40/10/100001.

[56] Y.-S. Tsai. Pair production and bremsstrahlung of charged leptons. *Rev. Mod. Phys.*, 46:815–851, Oct 1974. doi:10.1103/RevModPhys.46.815.

[57] M. Aharrouche et al. Energy linearity and resolution of the ATLAS electromagnetic barrel calorimeter in an electron test-beam. *Nuclear Instruments and Methods in Physics Research Section A: Accelerators, Spectrometers, Detectors and Associated Equipment*, 568(2):601 – 623, 2006. ISSN 0168-9002. doi:10.1016/j.nima.2006.07.053.

[58] T. Davidek and the ATLAS Tilecal system. ATLAS Tile Calorimeter performance for single particles in beam tests. *Journal of Physics: Conference Series*, 160(1): 012057, 2009. doi:10.1088/1742-6596/160/1/012057.

[59] B. Dowler et al. Performance of the ATLAS hadronic end-cap calorimeter in beam tests. *Nuclear Instruments and Methods in Physics Research Section A: Accelerators, Spectrometers, Detectors and Associated Equipment*, 482(1):94 – 124, 2002. ISSN 0168-9002. doi:10.1016/S0168-9002(01)01338-9.

[60] J. P. Archambault et al. Energy calibration of the ATLAS Liquid Argon Forward Calorimeter. *Journal of Instrumentation*, 3(02):P02002, 2008. doi:10.1088/1748-0221/3/02/P02002.

[61] The ATLAS Collaboration. Performance of the ATLAS Trigger System in 2015. *Eur. Phys. J.*, C77(5):317, 2017. doi:10.1140/epjc/s10052-017-4852-3.

[62] The ATLAS Collaboration. *ATLAS Computing: technical design report*. Technical Design Report ATLAS. CERN, Geneva, 2005. https://cds.cern.ch/record/837738.

[63] M. Cacciari et al. The anti-k_t jet clustering algorithm. *Journal of High Energy Physics*, 2008(04):063, 2008. doi:10.1088/1126-6708/2008/04/063.

[64] The ATLAS Collaboration. Monte Carlo Calibration and Combination of In-situ Measurements of Jet Energy Scale, Jet Energy Resolution and Jet Mass in ATLAS. Technical Report ATLAS-CONF-2015-037, CERN, Geneva, Aug 2015. https://cds.cern.ch/record/2044941.

[65] The ATLAS Collaboration. Jet energy measurement with the ATLAS detector in proton-proton collisions at $\sqrt{s} = 7$TeV. *The European Physical Journal C*, 73(3): 2304, Mar 2013. ISSN 1434-6052. doi:10.1140/epjc/s10052-013-2304-2.

[66] The ATLAS Collaboration. Jet Calibration and Systematic Uncertainties for Jets Reconstructed in the ATLAS Detector at $\sqrt{s} = 13$ TeV. Technical Report ATL-PHYS-PUB-2015-015, CERN, Geneva, Jul 2015. http://cds.cern.ch/record/2037613.

[67] The ATLAS Collaboration. Jet energy resolution in proton-proton collisions at $\sqrt{s} = 7$ TeV recorded in 2010 with the ATLAS detector. *Eur. Phys. J.*, C73(3): 2306, 2013. doi:10.1140/epjc/s10052-013-2306-0.

[68] The ATLAS Collaboration. Tagging and suppression of pileup jets with the ATLAS detector. Technical Report ATLAS-CONF-2014-018, CERN, Geneva, May 2014. https://cds.cern.ch/record/1700870.

[69] The ATLAS Collaboration. Muon reconstruction performance of the ATLAS detector in proton–proton collision data at $\sqrt{s}$ =13 TeV. *Eur. Phys. J.*, C76(5): 292, 2016. doi:10.1140/epjc/s10052-016-4120-y.

[70] J. Illingworth and J. Kittler. A survey of the hough transform. *Computer Vision, Graphics, and Image Processing*, 44(1):87 – 116, 1988. ISSN 0734-189X. doi:10.1016/S0734-189X(88)80033-1.

[71] The ATLAS collaboration. Electron efficiency measurements with the ATLAS detector using the 2015 LHC proton-proton collision data. 2016. https://cds.cern.ch/record/2157687.

[72] The ATLAS Collaboration. Electron and photon energy calibration with the ATLAS detector using LHC Run 1 data. *Eur. Phys. J.*, C74(10):3071, 2014. doi:10.1140/epjc/s10052-014-3071-4.

[73] The ATLAS Collaboration. Measurement of the photon identification efficiencies with the ATLAS detector using LHC Run-1 data. *Eur. Phys. J.*, C76(12):666, 2016. doi:10.1140/epjc/s10052-016-4507-9.

[74] D. Adams et al. Recommendations of the Physics Objects and Analysis Harmonisation Study Groups 2014. Technical Report ATL-PHYS-INT-2014-018, CERN, Geneva, Jul 2014. https://cds.cern.ch/record/1743654.

[75] Performance of missing transverse momentum reconstruction for the ATLAS detector in the first proton-proton collisions at at $\sqrt{s}$= 13 TeV. Technical Report ATL-PHYS-PUB-2015-027, CERN, Geneva, Jul 2015. https://cds.cern.ch/record/2037904.

[76] Data-driven determination of the energy scale and resolution of jets reconstructed in the ATLAS calorimeters using dijet and multijet events at $\sqrt{s} = 8\ TeV$. Technical Report ATLAS-CONF-2015-017, CERN, Geneva, Apr 2015. https://cds.cern.ch/record/2008678.

[77] E. L. Barberio et al. Search for new phenomena in monojet plus missing transverse momentum final states in pp collisions at $\sqrt{s} = 13$ TeV with the ATLAS detector. Technical Report ATL-COM-PHYS-2015-296, CERN, Geneva, Apr 2015. https://cds.cern.ch/record/2010840.

[78] The ATLAS Collaboration. Reconstruction, Energy Calibration, and Identification of Hadronically Decaying Tau Leptons in the ATLAS Experiment for Run-2 of

the LHC. Technical Report ATL-PHYS-PUB-2015-045, CERN, Geneva, Nov 2015. https://cds.cern.ch/record/2064383.

[79] S. Agostinelli et al. GEANT4: A Simulation toolkit. *Nucl. Instrum. Meth.*, A506: 250–303, 2003. doi:10.1016/S0168-9002(03)01368-8.

[80] P. Nason. A new method for combining NLO QCD with shower Monte Carlo algorithms. *Journal of High Energy Physics*, 2004(11):040, 2004. doi:10.1088/1126-6708/2004/11/040. http://stacks.iop.org/1126-6708/2004/i=11/a=040.

[81] T. Sjostrand et al. PYTHIA 6.4 Physics and Manual. *JHEP*, 05:026, 2006. doi:10.1088/1126-6708/2006/05/026.

[82] T. Sjostrand et al. A Brief Introduction to PYTHIA 8.1. *Comput. Phys. Commun.*, 178:852–867, 2008. doi:10.1016/j.cpc.2008.01.036.

[83] D. J. Lange. The EvtGen particle decay simulation package. *Nucl. Instrum. Meth.*, A462:152–155, 2001. doi:10.1016/S0168-9002(01)00089-4.

[84] T. Gleisberg et al. Event generation with SHERPA 1.1. *JHEP*, 02:007, 2009. doi:10.1088/1126-6708/2009/02/007.

[85] The NNPDF Collaboration. Parton distributions for the LHC Run II. *JHEP*, 04: 040, 2015. doi:10.1007/JHEP04(2015)040.

[86] H.-L. Lai et al. New parton distributions for collider physics. *Phys. Rev. D*, 82: 074024, Oct 2010. doi:10.1103/PhysRevD.82.074024.

[87] D. Berdine et al. Breakdown of the Narrow Width Approximation for New Physics. *Phys. Rev. Lett.*, 99:111601, Sep 2007. doi:10.1103/PhysRevLett.99.111601.

[88] D. Abercrombie et al. Dark Matter Benchmark Models for Early LHC Run-2 Searches: Report of the ATLAS/CMS Dark Matter Forum. 2015. https://arxiv.org/abs/1507.00966.

[89] Z. Marshall. Simulation of Pile-up in the ATLAS Experiment. *J. Phys. Conf. Ser.*, 513:022024, 2014. doi:10.1088/1742-6596/513/2/022024.

[90] W. Buttinger. Using Event Weights to account for differences in Instantaneous Luminosity and Trigger Prescale in Monte Carlo and Data. Technical Report ATL-COM-SOFT-2015-119, CERN, Geneva, May 2015. https://cds.cern.ch/record/2014726.

[91] The ATLAS Collaboration. Jet energy measurement and its systematic uncertainty in proton-proton collisions at $\sqrt{s} = 7$ TeV with the ATLAS detector. *Eur. Phys. J.*, C75:17, 2015. doi:10.1140/epjc/s10052-014-3190-y.

[92] S. J. Brodsky and L. Di Giustino. Setting the Renormalization Scale in QCD: The Principle of Maximum Conformality. *Phys. Rev.*, D86:085026, 2012. doi:10.1103/PhysRevD.86.085026.

[93] J. M. Campbell et al. A Multi-Threaded Version of MCFM. *Eur. Phys. J.*, C75 (6):246, 2015. doi:10.1140/epjc/s10052-015-3461-2.

[94] J. M. Campbell et al. Vector boson pair production at the LHC. *JHEP*, 07:018, 2011. doi:10.1007/JHEP07(2011)018.

[95] J. M. Campbell and R. K. Ellis. An Update on vector boson pair production at hadron colliders. *Phys. Rev.*, D60:113006, 1999. doi:10.1103/PhysRevD.60.113006.

[96] S. Dulat et al. New parton distribution functions from a global analysis of quantum chromodynamics. *Phys. Rev.*, D93(3):033006, 2016. doi:10.1103/PhysRevD.93.033006.

[97] B. Delaunay. Sur la sphère vide. A la mémoire de Georges Voronoï. *Bulletin de l'Académie des Sciences de l'URSS*, (6):793–800, 1934. http://www.mathnet.ru/php/archive.phtml?wshow=paper&jrnid=im&paperid=4937&option_lang=eng.

[98] The ATLAS collaboration. Search for new phenomena in the $Z(\to \ell\ell) + E_{\mathrm{T}}^{\mathrm{miss}}$ final state at $\sqrt{s} = 13$ TeV with the ATLAS detector. 2016. https://cds.cern.ch/record/2206138.

[99] J. Alwall et al. The automated computation of tree-level and next-to-leading order differential cross sections, and their matching to parton shower simulations. *JHEP*, 07:079, 2014. doi:10.1007/JHEP07(2014)079.

[100] The ATLAS Collaboration. Performance of b-Jet Identification in the ATLAS Experiment. *JINST*, 11(04):P04008, 2016. doi:10.1088/1748-0221/11/04/P04008.

[101] The ATLAS Collaboration. Optimisation of the ATLAS b-tagging performance for the 2016 LHC Run. Technical Report ATL-PHYS-PUB-2016-012, CERN, Geneva, Jun 2016. https://cds.cern.ch/record/2160731.

[102] T. Junk. Confidence level computation for combining searches with small statistics. *Nuclear Instruments and Methods in Physics Research Section A: Accelerators, Spectrometers, Detectors and Associated Equipment*, 434(2):435 – 443, 1999. ISSN 0168-9002. doi:10.1016/S0168-9002(99)00498-2.

[103] The ATLAS Collaboration, The CMS Collaboration, and The LHC Higgs Combination Group. Procedure for the LHC Higgs boson search combination in summer 2011. 2011. https://cds.cern.ch/record/1379837.

[104] A. Wald. An Extension of Wilks' Method for Setting Tolerance Limits. *Ann. Math. Statist.*, 14(1):45–55, 03 1943. doi:10.1214/aoms/1177731491.

[105] S. S. Wilks. The Large-Sample Distribution of the Likelihood Ratio for Testing Composite Hypotheses. *Ann. Math. Statist.*, 9(1):60–62, 03 1938. doi:10.1214/aoms/1177732360.

[106] G. Cowan et al. Asymptotic formulae for likelihood-based tests of new physics. *Eur. Phys. J.*, C71:1554, 2011. doi:10.1140/epjc/s10052-011-1554-0. [Erratum: Eur. Phys. J.C73,2501(2013)].

[107] The ATLAS Collaboration and The CMS Collaboration. Measurements of the Higgs boson production and decay rates and constraints on its couplings from a combined ATLAS and CMS analysis of the LHC pp collision data at $\sqrt{s} = 7$ and 8 TeV. *JHEP*, 08:045, 2016. doi:10.1007/JHEP08(2016)045.

Acknowledgements

At the very end of my thesis, I want to thank all the great people who made this thesis possible and the process of working on it so enjoyable.

First of all, many thanks to my supervisor Dr. Monica Dunford for convincing me to stay in our awesome KIP ATLAS group for my Master thesis and for supporting and advising me throughout the last year. I gladly remember both our off-topic chats and on-topic discussions and dare to say that I learned a lot about particle physics and its practical reality from you! I also want to thank Pavel for often being part of these discussions and serving with a lot of experience and, of course, humor.

Many thanks to Prof. Dr. Björn Malte Schäfer – for kindly agreeing to co-referee my thesis but also for his lecture which helped me to get a grasp of statistical methods. It was certainly helpful during the writing of this thesis.

I would also like to thank Prof. Dr. Hans-Christian Schultz-Coulon for sparking my interest of particle physics in the first place, for allowing me to write my Bachelor thesis in this group and to stay ever since, and for providing the framework of our great ATLAS group in general.

Thanks to all members of this group for making the average work day here seem less like work but rather enjoyable and special thanks to my office mates Alessandra, Manuel and Daniel. For the positive atmosphere in the office, your answers and our discussions whenever I was stuck and for helping me to endure the final stressful months of writing this thesis by showing me that you were writing just as stressfully.

Many thanks also to our farm admins Pavel, Thomas and Sebastian for constantly maintaining and improving the computing resources necessary for this thesis. Many thanks to Thomas and Sebastian in particular for enduring me steadily reporting any problems I encountered and for helping me basically instantly with all of them. I also want to thank their office mates Lars and Merve as this office was my first go-to place for any technical or physical question (and remarkably usually also my last, as I either returned with an answer or left everyone utterly confused).

Furthermore, I want to express my gratitude to Anja Butter and Anke Biekötter for showing me the theorist's point of view and for patiently setting up SFitter for my use case. I feel almost guilty for not using it after all, but understanding the underlying statistics definitely helped nonetheless.

For reading parts of this thesis and providing helpful feedback I would like to thank Jan, Thomas, Claire, Sebastian, Merve, Pavel, Daniel, Rainer, Mattis and Katja – especially considering that I asked you shortly before or even after Christmas. Special thanks to you and all my other friends in or outside of Heidelberg for helping me to bear the workload of the final months of this thesis with your uplifting mix of pity and spitefulness.

Finally, I want to thank my family for supporting me throughout the time of my studies and for tolerating my stressed mood the week between Christmas and the date of submission of this thesis.

Erklärung:

Ich versichere, dass ich diese Arbeit selbstständig verfasst habe und keine anderen als die angegebenen Quellen und Hilfsmittel benutzt habe.

Heidelberg, den 30.12.2017 .....